7-1-2016

Micro-Sandwich Test of Vapor-Deposited Hexanitroazobenzene (HNAB)

Caitlin O'Grady

Caitlin H. O'Grady

Candidate

Mechanical Engineering

Department

This thesis is approved, and it is acceptable in quality and form for publication:

Approved by the Thesis Committee:

Dr. Charles Randall Truman , Chairperson

Alexander S. Tappan

Dr. Asal Naseri Kouzehgarani

Dr. Svetlana Poroseva

Micro-Sandwich Test of Vapor-Deposited Hexanitroazobenzene (HNAB)

By

Caitlin O'Grady

B.S. Nuclear Engineering, University of New Mexico, 2013

THESIS

Submitted in Partial Fulfillment of the

Requirements for the Degree of

Master of Science

Mechanical Engineering

The University of New Mexico

Albuquerque, New Mexico

July, 2016

Acknowledgements

I would like to gratefully acknowledge:

- Alexander S. Tappan and Robert A. Knepper for assistance with this project
- Michael P. Marquez for his assistance with deposition and assembly,
- J. Patrick Ball, Thomas Conwell, and Jon Vasiliauskas for their assistance with detonation testing,
- Chuck Walker and Adrian Casias for assistance with annealing and cutting of tantalum,
- Juan Carlos Rodriguez for assistance with design and modeling,
- Ben Hanks for assistance with manufacturing, and
- Billy Cunningham and Amanda Gomez for assistance with deposition masks.

I would also like to thank my UNM advisor Dr. Truman for all of his help during this process and Dr. Asal Naseri and Dr. Svetlana Poroseva for agreeing to serve on my committee.

This project was funded by Sandia National Laboratories' Laboratory Directed Research and Development Program.

MICRO-SANDWICH TEST OF VAPOR-DEPOSITED

HEXANITROAZOBENZENE (HNAB)

By

Caitlin O'Grady

B.S. Nuclear Engineering, University of New Mexico, 2013

M.S. Mechanical Engineering, University of New Mexico, 2016

ABSTRACT

Experiments were conducted to support development of equation of state (EOS) of detonation products for the high explosive, hexanitroazobenzene (HNAB) using a scaled-down version of a sandwich test. The sandwich test is the 2-dimensional analog of the well-known 1-dimensional cylinder test. Use of the sandwich test allows experiments to be conducted on films of explosive produced by physical vapor deposition (PVD). PVD allows for close contact between the explosive and the substrate and provides repeatable geometries and microstructures. The PVD process was conducted in a custom deposition chamber at Sandia National Laboratories. HNAB was deposited by vacuum thermal evaporation onto tantalum substrates that were rotated to ensure uniform thicknesses. Amorphous HNAB films were deposited onto three different thicknesses of tantalum substrates, crystallized to HNAB-II at 35°C, then assembled into a symmetrical slab configuration by joining two identical small-scale samples to form the "micro-sandwich." The experiment successfully measured velocity of the tantalum liner during detonation. The experimental data were provided to modelers to validate EOS generated using the CTH shock-physics code.

Table of Contents

List of Figures

List of Tables

Abbreviations

CJ	Chapman-Jouguet
CTE	Coefficient of thermal expansion
EOS	Equation of State
HE	High Explosive
HNAB	Hexanitroazobenzene
JWL	Jones-Wilkins-Lee
PDV	Photonic Doppler Velocimetry
PETN	Pentaerythritol tetranitrate
PVD	Physical Vapor Deposition
TNT	Trinitrotoluene

Nomenclature

$\%TNT_{HE}$	percentage of TNT equivalence for that particular explosive
A	JWL Constant (Mbar)
B	JWL Constant (Mbar)
C	JWL Constant
f_{beat}	measured beat frequency
l	length of the liner
m_{HE}	mass of the high explosive
m_{HE}/A	mass per area of the high explosive
m_l/A	mass per area of the liner
P_s	Low Pressure term JWL
P	pressure
R_1	JWL Constant (dimensionless)
R_2	JWL Constant (dimensionless)
t	thickness of the liner
t_{HE}	thickness of the high explosive
TNT_{equiv}	TNT equivalence for the explosive
v	velocity
V	Specific Volume
w	width of the liner
λ_{laser}	wavelength of the laser used in the PDV system
ρ	density of the liner
ρ_{HE}	density of the high explosive
ω	JWL Constant (dimensionless)

1 Introduction

The computational modeling of explosives is of increasing importance as the models are useful to predict and understand explosive behavior. These models are constantly evolving as more information becomes known about various explosives. Computational codes allow for informed experiment design, as well as a greater understanding of explosives and their behavior. Additionally, modeling of explosives allows for safer handling and use of explosives. Accurate modeling of explosives depends on experimental determination of specific information unique to that individual explosive.

The standard method to obtain the reaction products equation of state (EOS) data for a high explosive (HE) is to conduct a cylinder test. A cylinder test consists of a metal tube (usually copper) confining the explosive that is detonated at one end. The detonation causes the cylinder to expand to a funnel shape. Both the radial and axial velocities are measured during the detonation with different diagnostic equipment from which the EOS is derived.

A sandwich test is the 2-dimensional adaptation of this well-known 1-dimensional cylinder test. A sandwich test uses slab geometry rather than cylindrical geometry. Both the sandwich and cylinder tests can be used to determine the EOS for a specific explosive. The goal of this project is to provide data in support of developing the products EOS of the explosive hexanitroazobenzene (HNAB). The products EOS for an explosive is specific to characteristics such as chemical makeup and density, and thus the experiment must be conducted separately for each explosive of interest. For this experiment, high-density HNAB is prepared using physical vapor deposition (PVD),

which lends itself to the slab geometry of the sandwich test. The sandwich test consists of slab geometry with a liner, generally metal, on either side of the explosive that is being tested. In essence, the explosive is the meat and the liner is the bread of the sandwich. This thesis focuses on utilizing small-scale sandwich tests, which have been named "micro-sandwich" tests.

The objectives of this thesis were to develop an experiment and acquire data that support developing the EOS for HNAB. Data that will lead to development of an EOS has been determined experimentally from a series of small-scale sandwich tests of HNAB. The sandwich test measured the velocity of the metal liner during explosive loading, which informs the explosive's EOS (Hill, 2002). The experimental data will be provided to modelers and used to develop a computational model for EOS, which will be compared to existing computational models.

1.1 Purpose and Motivation

The purpose of this project was to collect data that can lead to development of the reaction products EOS experimentally for high-density, vapor-deposited HNAB, which will be used to validate the EOS computed using thermochemical equilibrium calculations. This experiment will be computationally modeled using both thermochemical equilibrium calculations as well as shock physics codes. Shock physics codes allow for informed experiment design, as well as a greater understanding of explosives and their behavior. CTH is a numerical computational code that was developed by Sandia National Laboratories. The products EOS for HNAB will provide

more information about the explosive and will allow computations with the CTH shock physics code.

The investigation provided experimental data to support development of an explosive products EOS, such as Jones-Wilkins-Lee functions, through development of the micro-sandwich test. The motivation for this thesis comes from a need to better understand the parameters that govern the HNAB explosive, its detonation, and the products EOS. HNAB films produced by PVD are of interest as a model explosive system due to the high density, low surface roughness and unique microstructure that can be obtained from the PVD process.

1.2 History

The cylinder expansion test has been in use since the 1940's (Jones & Miller, 1948). It quickly became the experiment of choice for characterization of explosive detonation. Cylinder tests are widely used in order to inform explosive effects of detonation, and can be used to determine the products EOS data for different explosives. Cylinder tests have been described as being an "explosively-driven, outward radial expansion of a standard metal cylinder" which is observed by a streak camera and have "become one of the classic experimental tools in research concerned with detonation dynamics" (Polk, 1984).

The sandwich test has only come into use more recently for the purpose of determining the explosive products EOS. This iteration of the sandwich test was developed by Larry Hill (2002) of Los Alamos National Laboratory in the early 2000's. It is very similar to the cylinder test in that it yields much of the same information when used with relatively thin confinement. Like the cylinder test, the sandwich test is also very useful for

determining data about explosives and explosive behavior, including being used to predict explosive effects of detonation and to derive the products EOS for different explosives. Data from sandwich tests can be used to derive and better inform the computational models. For specific cases, the sandwich test has several advantages over the cylinder test, which are discussed below.

1.3 Background

The sandwich (or slab) test has been successfully used to establish the EOS from detonation. It is a similar experiment to the cylinder test, which relies on axisymmetric geometry for confinement. The sandwich test is better suited for explosives that can be deposited by PVD, whereas explosives that are manipulated in the solid or liquid form are better suited for the cylinder test. PVD refers to the process of physical vapor deposition by vacuum thermal evaporation used in this experiment to deposit HNAB onto the substrate surface.

There is a need for modeling to support design and interpretation of experiments involving high explosives (HE). Accurate data for products EOS is the basis for shock-physics codes like CTH, which are in turn used to predict explosive phenomena. CTH is used for "modelling complex multi-dimensional, multi-material problems that are characterized by large deformations and/or strong shocks" (Hertel, et al., 1992).

Modelling of high explosive behavior roughly consists of three components. First, the unreacted (inert) explosive Equation of State, which include the shock velocity – particle velocity Hugoniot ($U_s - u_p$) and the Mie-Grüneisen EOS. Second, the reactive flow model, including models such as Ignition and Growth, the Arrhenius Reactive Burn, and History-Variable Reactive Burn, which describes the chemistry during explosive

reaction. Third, explosives modeling must include an explosives products EOS using a model such as the Jones-Wilkins-Lee (JWL) functions. The data acquired during these tests will be used to calibrate a JWL EOS that was calculated from thermochemical equilibrium calculations.

1.3.1 Jones-Wilkins-Lee Functions

A Jones-Wilkins-Lee (JWL) function is used to model the pressure of expanded detonation products gases. The rate of the products gas expansion is used to develop constants for the JWL function particular to an explosive. For the cylinder test, the constants that are derived in the JWL function get fit to the cylinder test data. The JWL function provides pressure as a function of specific volume starting at the Chapman-Jouguet (CJ) state along the "expansion isentrope" as shown in Figure 1.

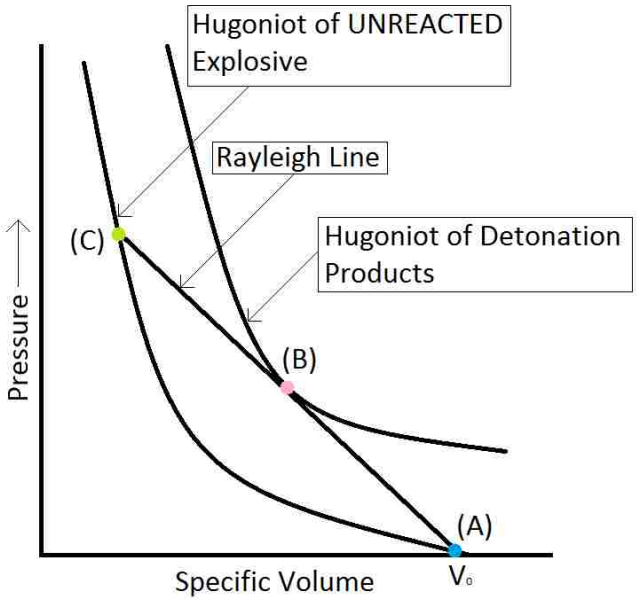

Figure 1: P-V representation of detonation with (A) as the initial state of unreacted explosive, (B) as the state of reaction products, and (C) as the jump condition to the fully shocked but unreacted explosive. Adapted from (Cooper, 1996).

The CJ point in Figure 1 is labeled as point (B). The CJ point refers to the "state of the products behind the detonation front" that was hypothesized to be the condition of steady-state detonation (Cooper, 1996). The jump point (C), also known as the von Neumann spike, refers to the condition from the unreacted explosive to the fully shocked, unreacted explosive. Finally, point (A) simply refers to the pressure-specific volume state of the unreacted explosive. These points correspond to constants in the JWL EOS empirical formula.

The JWL function is not a fundamental EOS and it yields an incomplete description of the products' states. In the case of the surface shock reflection during an explosion, the JWL function cannot provide information on the products' states. It also does not take into account after-burn effects due to hot products of detonation mixing with air. The after-burn process causes the release of "the heat of reaction via a turbulent combustion process," which, in turn, causes the temperature of the products to increase to the "adiabatic flame temperature (~3,000K)." (Kuhl, 2010). The empirical formula for the JWL EOS (Weseloh, 2014) is

$$P = Ae^{-R_1 V} + Be^{-R_2 V} + CV^{-(1+\omega)} \quad (1)$$

where A, B, C, R_1, R_2, and ω are all constants that are specific to the explosive. P refers to the pressure and V refers to the specific volume. Integrating this equation yields an equation for E, the internal energy on the isentrope of the explosive (Weseloh, 2014),

$$E = -\int P\, dV = \frac{A}{R_1} e^{-R_1 V} + \frac{B}{R_2} e^{-R_2 V} + \frac{C}{\omega} V^{-\omega} \quad (2)$$

As the products expand, the internal energy declines.

Using the Cheetah thermochemical equilibrium code (Fried, 1994), the JWL constants for HNAB-II were calculated. The resulting constants are listed in Appendix C.

The data acquired through experimentation using the micro-sandwich test in this project will be used to support development of an explosive products EOS.

1.3.2 Sandwich Test

Sandwich tests were designed by Los Alamos National Laboratory (LANL). LANL used these tests to obtain data for high explosive detonation shock dynamics models. The sandwich test was originally designed as an alternative to the much-used cylinder test.

To predict the explosive effects of a detonation, cylinder tests are widely used. Cylinder tests are commonly used to experimentally determine the products EOS data for different high explosives. Computational models have been developed from successful cylinder test experiments. For any explosive, the EOS are unique, thus the EOS for HNAB will differ from the EOS of other explosives. For specific cases, the sandwich test had several advantages over the cylinder test.

The cylindrical geometry causes the liner to stretch and thin, which can only be completed by a very ductile material that can expand adequately without tearing. Conversely, the slab geometry of a sandwich test requires only liner bending, which allows for thinner materials. Other criteria can be used for material selection in the slab/sandwich geometry. The slab geometry also has the advantage of designs that "accommodate a wide range of initial charge temperatures." The cylindrical geometry does not have the capacity for the wide range of initial temperatures due to "differential thermal expansion between HE and the liner," especially in the cold case (Hill, 2002).

There have been several instances in which the sandwich test was successfully used. Sandwich tests have been performed on PBX 9502 (plastic bonded explosive, 95% triaminotrinitrobenzene) explosive to determine detonation velocity and leading detonation shock shape (Aslam, et al., 2004). This experimental method has also been employed on ammonium nitrate and fuel oil (ANFO) and PBX 9501 (plastic bonded explosive, 95% cyclotetramethylenetetranitramine) in order to compare the geometrical effects and how they compare to the cylinder expansion tests of the same material (Jackson & Short, 2015). These experiments use a sandwich test with approximate dimensions of 12.7 mm × 152.4 mm × 152.4 mm. The experiment performed in this thesis utilizes a scaled-down version of the sandwich test, dubbed the micro-sandwich, of dimensions approximately 0.2 mm × 10 mm × 30 mm.

1.3.2.1 Micro-Sandwich

As previously noted, the micro-sandwich is a smaller version of a standard sandwich test. There are several reasons to use a micro-sandwich as opposed to a regular sandwich test or cylinder test in this case. Primarily, the vapor-deposition process for HNAB is the limiting factor. PVD does not allow for large amounts of explosive material to be deposited easily. Also, cylindrical geometry as would be needed in a cylinder test is not really conducive to the PVD process.

When dealing with explosives, it is a good practice to use the least amount of explosive material as possible. This is done for safety reasons. The micro-sandwich uses much less explosive material than does a standard sandwich test or even a cylinder expansion test.

As a general rule of thumb, when dealing with explosives it is a good practice to locate any diagnostic equipment at least 10 diameters away from the source of ignition. In the case of the micro-sandwich, the primary diagnostic is located approximately 100 thicknesses away from the source of ignition. This is another advantage of the micro-sandwich.

1.3.3 HNAB Explosive

High explosives are categorized as either primary or secondary explosives depending on the sensitivity of the explosive to ignition. Secondary explosives generally require a detonator to be initiated, whereas primary explosives can detonate when exposed to heat or shocks. Hexanitroazobenzene, referred to as HNAB, is a secondary explosive. HNAB is a thermally stable secondary explosive that has been investigated since the 1960s. It is well-suited for this experiment as it does not decompose at its melting point of 221°C and has a sufficiently high vapor pressure to evaporate from the melt (Dobratz & Crawford, 1985). These properties allow it to be vapor deposited.

HNAB has characteristics that make it well-suited for this experiment. The fact that HNAB is thermally stable above its melting temperature means that high-vapor pressures can be reached with only marginal chemical decomposition, making it well-suited for PVD. This also means that the deposition process is faster than with other explosives (Knepper, et al., 2012). The chemical structure of HNAB is shown in Figure 2.

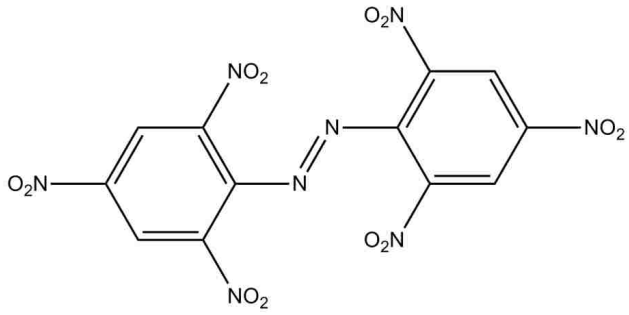

Figure 2: The chemical structure of HNAB.

HNAB films made by PVD were chosen for development of the micro-sandwich test because they have high density, low porosity, and low surface roughness with uniformity throughout the deposition thickness.

Directly after the PVD process, HNAB is in the form of an "amorphous film" that crystallizes over time. This means that the post-processing of the substrates is a critical aspect of the experiment. The conditions in which the substrates are kept affect the detonation performance of the substrate. Particularly, the temperature under which the HNAB is crystallized affects the microstructure of the HNAB, which is directly related to the properties of detonation of HNAB. "Specifically, HNAB crystallized at room temperature has uniformly distributed pores with diameters generally less than 150 nm and has a critical thickness of 63.4 ± 1.3 μm" (Tappan, et al., 2014). The critical thickness of an explosive refers to the minimum thickness of an explosive that can consistently be detonated.

Depending on crystallization temperatures and conditions, another form of HNAB can form. The desired form is called HNAB-II, whereas another undesirable form is called the unknown phase. The yet-to-be-determined unknown yellow phase does not have the same detonation properties as the HNAB-II form. The differing form of HNAB is easily

distinguished from the desired form. The desired form of HNAB, HNAB-II, is a distinct orange color whereas the other form, an as-yet-undetermined phase of HNAB, is a yellow color.

1.3.4 Physical Vapor Deposition of HNAB

The process of physical vapor deposition by vacuum thermal evaporation is used with HNAB. For this experiment the vapor deposition is conducted in a custom deposition chamber located at Sandia National Laboratories, which is shown in Figure 3. Physical vapor deposition allows for direct contact between the explosive and the substrate. PVD allows for the deposition to occur in various shapes and provides constraint over the explosive geometry and microstructure.

Figure 3: Custom deposition chamber used to deposit HNAB onto tantalum for this experiment, it is located at Sandia National Laboratories (Knepper, 2014).

The process occurs in "a custom designed high-vacuum deposition system evacuated to a base pressure in the order of 1.33×10^{4} Pa. Films were deposited at a nominal source-to-substrate distance of 10 mm from an effusion cell thermal deposition source." The deposition system is loaded with HNAB-II powder and the effusion cell is heated to "a

maximum temperature of 230°C." The HNAB powder is vaporized and condenses on the substrates. The substrates are rotated at a rate of 50 rpm, which ensures uniform thicknesses between the different substrates. As previous experiments have found, there is about ± 5% difference between the thickness of the deposited explosive as measured "with a Dektak 8 surface profiler with a 5 μm stylus" (Knepper, et al., 2012). The substrates are cooled on a copper block during the deposition in order to ensure the deposition occurs at room temperature. A basic schematic of the deposition process inside the custom chamber is shown in Figure 4.

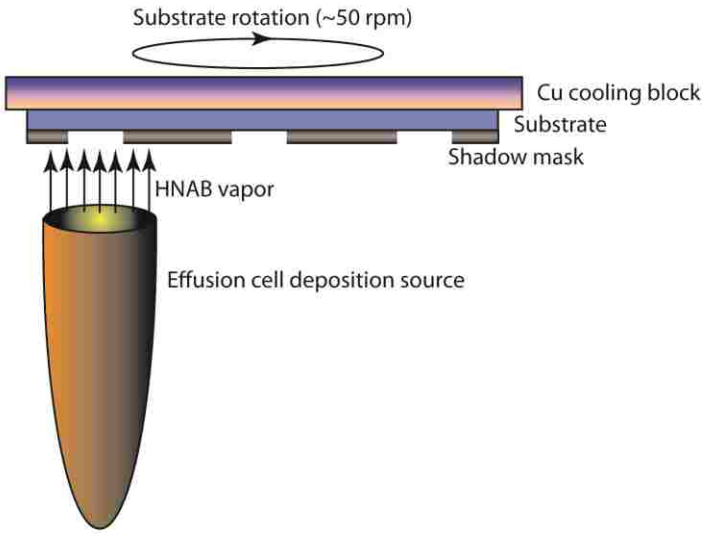

Figure 4: Schematic of the deposition system used to deposit HNAB onto substrates, from (Knepper, 2014).

The HNAB films have been found to be generally uniform across different depositions if the substrate remains adequately cool during the deposition process. This means that the HNAB substrates are somewhat unaffected by differing deposition conditions if the substrates are kept cool during the process (Knepper, et al., 2012).

The consistent deposition of the HNAB onto the substrate allows for multiple samples to be made and crystallized, each of the same thickness and conditions. This is important for this experiment, which consists of joining two identical substrates to create the "sandwich." This also allows for choosing the best substrates for the experiment and removal of the substrates that develop the unknown phase of HNAB.

The HNAB was deposited onto 10 mm × 30 mm tantalum substrates. The substrates were cut from a 5 inch by 5 inch piece of tantalum foil using a LPKF ProtoLaser U3 (355 nm) laser cutting tool shown in Figure 5.

Figure 5: LPKF ProtoLaser U3 (355 nm) System that was used to cut tantalum foil into the correctly sized substrates (LPKF:Laser&Electronics, 2016).

The laser cutting system is an ultraviolet system that has a 20 μm focused beam diameter (LPKF:Laser&Electronics, 2016). It was successfully used to cut the tantalum foil into the appropriate dimensions.

HNAB films made by PVD were initially an amorphous structure that was later crystallized at 35°C. The crystallization process varies according to substrate conditions and can take between 1 week to 1 month to fully crystallize. After crystallization, the micro-sandwich was assembled by joining two similar substrate samples into the symmetrical slab configuration.

1.3.5 TNT Equivalence

The amount of explosive energy for a specific type of explosive is often expressed in an equivalent amount of TNT (trinitrotoluene). TNT equivalence is a way to relate the potential energy output of different explosives to a known baseline, TNT output. "The strength of explosions is commonly related through the TNT equivalence concept to the effect from an equivalent mass of TNT. This provides a useful but crude means of comparing the severity of blast effects and likely damage–distance relationships from a variety of explosion sources" (Wharton, et al., 2000).

TNT equivalence relates the potential explosive output of a source in terms of an equivalent mass of TNT. "TNT-equivalence should be considered more or less a 'worst case', in which energy is released at the highest possible rate or, in any case, at a higher rate than in gas or steam vessel explosions or the like" (Held, 1983). The equivalent mass of TNT is

$$TNT_{equiv} = \sum m_{HE} \times \%TNT_{HE} \quad (3)$$

where TNT_{equiv} refers to the TNT equivalence for the explosive, m_{HE} refers to the mass of the high explosive, and $\%TNT_{HE}$ refers to the percentage of TNT equivalence for that particular explosive. For example, HNAB has a $\%TNT_{HE}$ of 112%.

The TNT equivalence is especially pertinent to this experiment as it is a potential limiting factor resulting from the explosive rating of the explosive chamber. The micro-boombox utilized in this experiment has a maximum allowable TNT equivalence of 110 mg, which limits the amount of HNAB that can be deposited on the substrate.

1.3.6 Diagnostic Equipment

Specification sheets for the diagnostic equipment is shown in Appendix B.

1.3.6.1 Surface Profiler System

The Bruker DektakXT surface profiler system is used to determine the thicknesses of deposited materials. The system is shown in Figure 6.

Figure 6: Image of the DektakXT machine used to take surface thickness measurements of the substrates for this experiment (Bruker, 2016).

The system has a very sensitive stationary stylus under which the sample is moved; stylus deflection yields the thickness of deposited material compared to the surface it is deposited on.

1.3.6.2 Streak Camera

The SC-10 streak camera from Optronis is one of the diagnostics of this experiment that can be used to determine the liner velocity. The streak camera is not the primary diagnostic tool for determining the liner velocity. It was discussed that the streak camera could serve as backup in case the main diagnostic (photonic Doppler velocimetry (PDV) probe) failed, but it was determined that the streak camera did not have adequate precision in measurements. The streak camera yields data that relates time relative to space during the experiment. The basic layout of a streak camera is shown in Figure 7.

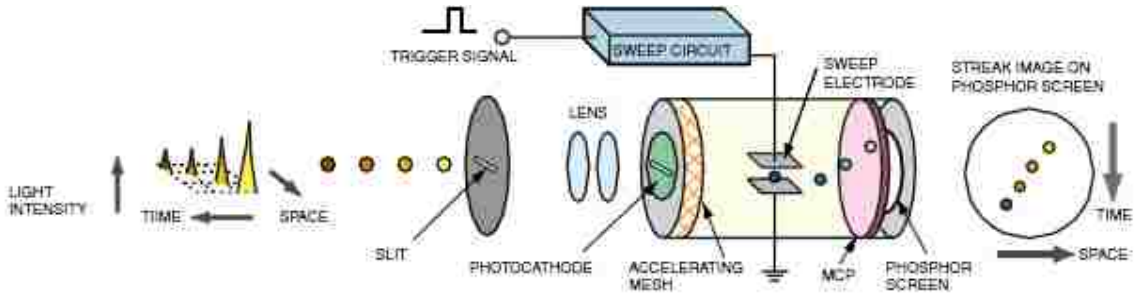

Figure 7: Basic layout of a streak camera (Hamamatsu, 2015).

Streak cameras yield information that relates both the time and spatial aspects of the experiment. Light from the experiment is imaged onto a slit and transferred to the streak tube with internal optics. A diagram of the streak tube is shown in Figure 8.

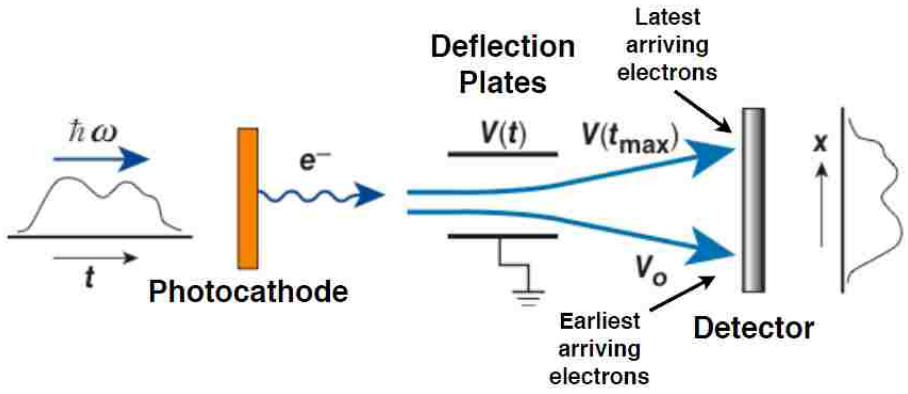

Figure 8: Streak camera streak tube layout (OMEGA-Laser-Facility).

The main unit of the streak camera consists of the streak tube with the electronics that control it and the electromechanical shutter (Hamamatsu, 2015). The streak tube has a few different parts, including the photocathode, deflection plates, and the detector. The line image is projected onto a photocathode. The photocathode converts photons into electrons proportional to the intensity of the light (Hamamatsu, 2015). Specifically, the SC-10 unit has a S25 photocathode, meaning the spectral range is between 200-950 nm (Optronis, 2010). These electrons are then accelerated by an electric field that is generated by deflector plates and are deflected. The bias (amount of voltage) on the deflection plates increases over time, meaning that early electrons are deflected less than later electrons. This "time-varying voltage" process causes electrons to be streaked across the detector that allows time data to be captured (OMEGA-Laser-Facility). The detector consists of the micro-channel plate (MCP) and the phosphor screen. The MCP multiplies the number of electrons before they impact the phosphor screen. The phosphor screen converts the electrons back into light. This light is detected as an image by an image intensifier. The image intensifier is specific to the type of camera, the SC-10 system has a "fiber optically coupled image intensifier II125 [and] is a modular part of SC-10 based systems" (Optronis, 2010). The image intensifier "provides photon counting sensitivity combined with high detection efficiency and low amplification noise" (Optronis, 2010).

1.3.6.3 Framing Camera

Capable of taking up to a billion frames per second (or 1 frame per nanosecond), the SIMX high-resolution multi-channel/multi-spectral framing camera is important for this experiment. The system is shown in Figure 9.

Figure 9: Image of the SIMX ultra-high speed framing camera (Specialised-Imaging).

The framing camera was a very important diagnostic for this experiment, as it was used to measure the liner angle during the experiment. The liner angle is used to inform data analysis correlating to other diagnostic equipment, including the angle of the liner where the Photonic Doppler Velocimetry (PDV) probe is placed. It also provides a record of what took place during the experiment in the form of timed images.

The SIMX camera is similar to digital cameras. The SIMX has 16 separate optical channels, and therefore 16 individual intensified CCD sensors. Each CCD sensor records a separate image defined by the internal timing of the framing camera.

Another advantage of the SIMX having individual intensified CCD sensors for each image is that noise that is recorded into the resulting images is reduced. This means that the experimental data is more accurate.

1.3.6.4 Illumination Source

The experiment utilized a SILUX-640 spoiled coherence laser as an illumination source that was used to backlight the experiment, providing light that was obscured from the camera due to liner motion. The laser nominally has a wavelength of 640 nm.

1.3.6.5 Photonic Doppler Velocimetry

Photonic Doppler Velocimetry, abbreviated as PDV, is a technique used to measure the velocity of an interface. The probes are used to "analyze the change in the phase of the return wave caused by the displacement…of the surface along the beam" (Briggs, et al., 2009). The tantalum surface motion was recorded using the PDV system. Figure 10 illustrates the PDV technique.

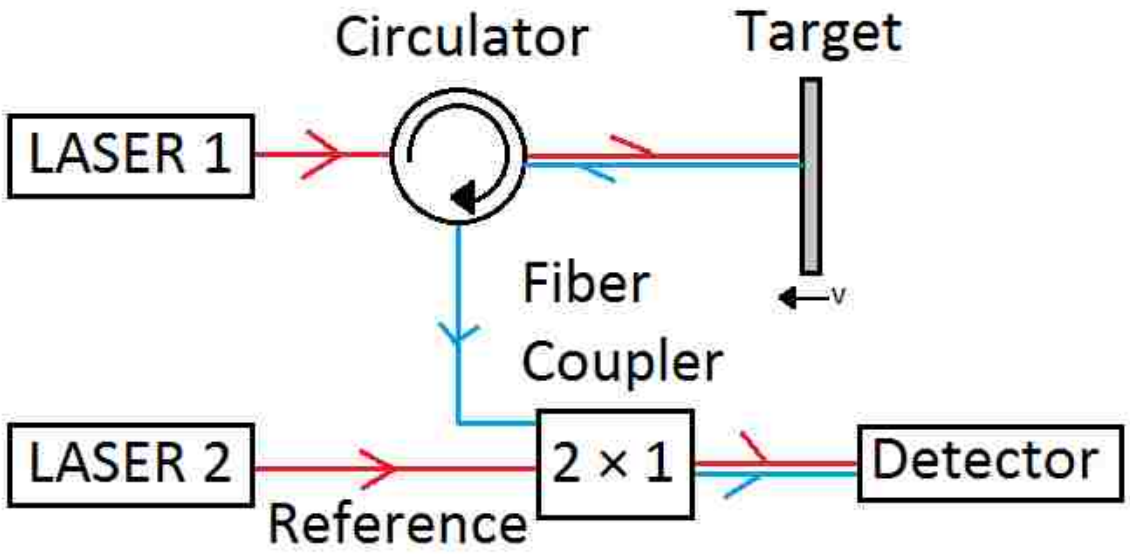

Figure 10: The basic setup of an upshifted PDV system, adapted from Ao (2010).

For this experiment, a laser generates a beam that is propagated through a single mode fiber connected to a circulator. The circulator transmits the beam to a probe lens, which focuses the beam onto the target. The light is reflected from the target back onto the probe lens. During detonation in the experiment, as the target moves the reflected light

undergoes a Doppler shift. The probe lens collects sections of the Doppler-shifted light that is propagated back through circulator to a fiber coupler. Both Doppler-shifted light and unshifted light are mixed together via a coupler which generates a beat frequency that is then sent to the optical detector. The optical detector "generates an electrical current proportional to the square of the optical fields," (Sargis, et al., 1999) which corresponds to the beat frequency of the Doppler-shifted and unshifted light. The beat frequency is proportional to the instantaneous velocity of the target (Sargis, et al., 1999). For both explosive and high velocity experiments, the beat frequency is measured and recorded "using a high-bandwidth photodiode and oscilloscope" (Maisey & Bowden, 2008).

In the case of this experiment, the PDV probes were angled to give the best return signal of the tantalum substrate. The tantalum target surface that the measurements are taken on was moving towards the PDV probe during the experiment. From previous work on cylinder expansion tests, the PDV probe angle should be fairly low, on the order of 4° to 6° (S. Pemberton, personal communication, June 8, 2016).

The PDV measurements utilize "recent advances in 1550 nm detector technology and fast digitizers to record beat frequencies in the gigahertz (GHz) range" (Jensen, et al., 2009). Among the advantages of the PDV system are its simple assembly and operation with components that are easily obtainable. Additionally, the PDV system does not have an inherent time delay and can be used with different target surface reflectivity values (Jensen, et al., 2009).

For the PDV system, the relationship between the measured beat frequency and the velocity (Maisey & Bowden, 2008) is

$$v = \left(\frac{\lambda_{laser}}{2}\right) f_{beat} \quad (4)$$

where v refers to the velocity, λ_{laser} is the wavelength of the laser used in the PDV system, and f_{beat} is the measured beat frequency.

1.3.6.6 Micro-Boombox

The micro-boombox is a chamber that is rated for small-scale explosives testing. This aluminum box is rated based on the largest amount of TNT equivalent explosive that can be safely detonated in the box. This experiment utilized a micro-boombox with a maximum allowable TNT equivalence of 110 mg. A model of a micro-boombox is shown in Figure 11.

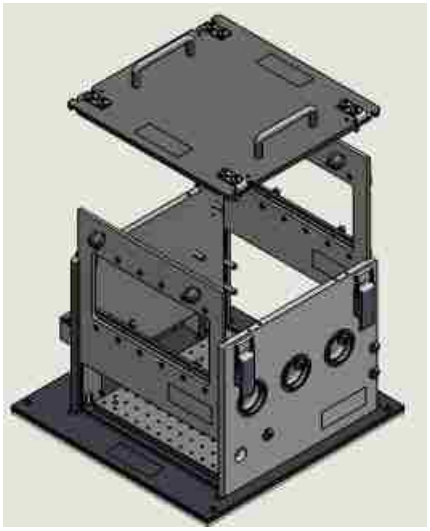

Figure 11: A SolidWorks drawing of the Micro-Boombox used in this experiment (Image Courtesy of Sandia National Laboratories).

The micro-boombox is a very important part of this experiment. It limits the amount of explosive that can be used in the micro-sandwich as well as the size of the full micro-sandwich apparatus. The internal volume of the micro-boombox is approximately 0.0283 m^3 (1 ft^3), which must contain the entire micro-sandwich system, including initiation

apparatus and the PDV probe. It must also allow clear viewing of the micro-sandwich by the framing and streak cameras.

1.3.7 Tantalum Substrate

1.3.7.1 Tantalum

It was determined that "stiff, high density metals" (Hill, 2002) are favored in sandwich tests. These materials are favored in order to satisfy the Gurney approximation (Hill, 2002), which requires that the mass per area of the liner be greater than or equal to one-third of the mass per area of the HE

$$\frac{m_l}{A} \geq \left(\frac{1}{3}\right)\left(\frac{m_{HE}}{A}\right) \qquad (5)$$

where m_l/A is the mass per area of the liner and m_{HE}/A is the mass per area of the high explosive. For this experiment, the mass per area of the high explosive is the same between the three different thicknesses of substrate. This means that the appropriate thickness for the liner in the micro-sandwich test can be found.

Additionally, higher values of acoustic impedance are desired to "provide better confinement" (Hill, 2002), as well as tough material that will resist tearing. Hill determined that there were three potential choices for liner substrate, molybdenum, tantalum, and tungsten (Hill, 2002). Tantalum is desired for several reasons, including the toughness of tantalum and the acoustic impedance that allows it to provide better confinement.

The tantalum foil (ESPI Metals, 99.98%) was purchased in 5 inch by 5 inch squares. These foils were cut using a LPKF ProtoLaser U3 (355 nm) laser cutting tool to obtain the 10 mm × 30 mm substrate upon which HANB was vapor-deposited.

1.3.7.2 Thickness

Choosing the correct thickness of liner material, tantalum, is crucial to this experiment. The liner must be thick enough so it will not break during the experiment, as well as ductile enough to deform during the experiment without creasing. Satisfying the Gurney approximation (Hill, 2002) for EOS analysis, the thickness is determined based on the material and amount of explosive that is deposited. The Gurney approximation yields an estimate of the liner mass needed to prevent the liner velocities from exceeding the Gurney characteristic velocity for the explosive (Kennedy, 2003). Gurney calculations established that the 50.8 ± 2.5 µm (2 mil) thickness of tantalum substrate would be sufficient for the 100 µm thickness of HNAB on each substrate. Performing the same calculation for a 25.4 µm (1 mil) thick sample yielded results that thickness would be insufficient. This was based on the Gurney approximation presented in Equation (5). The design of this experiment was based on the liner mass per area

$$\frac{m_l}{A} = \frac{\rho lwt}{lw} = \rho t \qquad (6)$$

where l is the length of the substrate, w is the width of the substrate, t is the thickness of the substrate, and ρ is the density of the substrate. Thus the mass per area for the liner is

$$\frac{m_l}{A} = \left(16.654\ \left[\frac{mg}{mm^3}\right]\right)(2 * 50.8\ [\mu m])\left(\frac{0.001\ [mm]}{1\ [\mu m]}\right) = 0.1692\ \left[\frac{mg}{mm^2}\right] \qquad (7)$$

Similarly the mass per area for two 100 μm layers of the HE is

$$\frac{m_{HE}}{A} = \rho_{HE} t_{HE} \quad (8)$$

$$\frac{m_{HE}}{A} = \left(1.735 \left[\frac{mg}{mm^3}\right]\right)(0.2\,[mm]) = 0.3530 \left[\frac{mg}{mm^2}\right] \quad (9)$$

where t_{HE} is the thickness of the high explosive, and ρ_{HE} is the density of the high explosive.

The Gurney approximation is satisfied because the mass per area of the liner is greater than one-third of the mass per area of the HE

$$0.169 \left[\frac{mg}{mm^2}\right] > \left(\frac{1}{3}\right)(0.353) = 0.118 \left[\frac{mg}{mm^2}\right] \quad (10)$$

Thus, using 50.8 ± 2.5 μm thick tantalum, the Gurney approximation is satisfied for the fully assembled micro-sandwich amount of HNAB, of 200 μm thickness. The experimental results tested the assumption that the 50.8 μm thickness is sufficient by testing multiple thicknesses. Three different thicknesses of tantalum were tested, 50.8 ± 2.5 μm (2 mil), 76.2 ± 5.1 μm (3 mil), and 101.6 ± 1.3 μm (4 mil). Each substrate had dimensions of 10 mm × 30 mm each with nominally 100 μm thickness of HNAB vapor deposited onto the surface.

Two different methods were employed to measure the thicknesses of the tantalum foils. The first was digital calipers to make the thickness measurement. Several different measurements were taken to confirm the entire foil had the same thickness. The measurements were taken at the edges of the substrate as well as a few in the middle of

the substrate. These results were found to be nominally what was expected, as described by the manufacturer. The error between what the manufacturer claimed and the average measured thickness ranged from 0.33% to 5%. The digital measurement made with the calipers was determined to be the preferred measurement because it had a lower total potential error. These were the values that were used in calculations. The other method measured the mass, width, and lengths of several different cut substrates and calculated the thickness using the known density of the tantalum. Because each of these measurements had an associated error, the final error was much higher, ranging between 6% and 15%.

2 Design and Experimental Setup

2.1 Apparatus

2.1.1 Sandwich Assembly

Two tantalum/hexanitroazobenzene (HNAB) substrates were joined using Sylgard ® 527 adhesive to create the "sandwich." This adhesive has a low viscosity and has been found to not react with HNAB. When the Sylgard ® 527 adhesive was acquired, a visual compatibility test was completed with HNAB. It was put directly onto a HNAB substrate and left to cure. Over time it was observed that there was no color change in the HNAB or adhesive, suggesting that the Sylgard ® 527 adhesive did not react with the explosive. Thus, it was determined that the Sylgard ® 527 adhesive would be suitable for this experiment as it could provide adhesion between substrates with only a thin layer. Additionally, the adhesive will exclude any air gaps or bubbles between the two substrates of the micro-sandwich. A cartoon cross-section is shown in Figure 12.

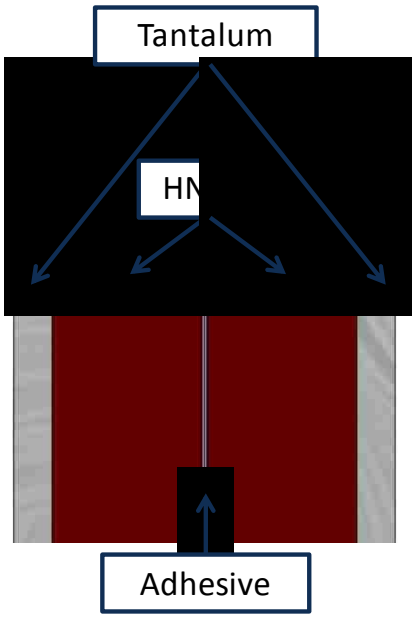

Figure 12: Cross-section of a typical sandwich test.

The sandwich was limited to 100 mg or less of TNT (trinitrotoluene) equivalence due to the explosive rating of the micro-boombox. This allows for ~100 µm thickness of HNAB on each tantalum substrate, making the sandwich itself having ~200 µm thick HNAB. The tantalum/HNAB substrates were measured using the DektakXT surface profiler system to establish the thickness of each HNAB layer. This is shown in Figure 13.

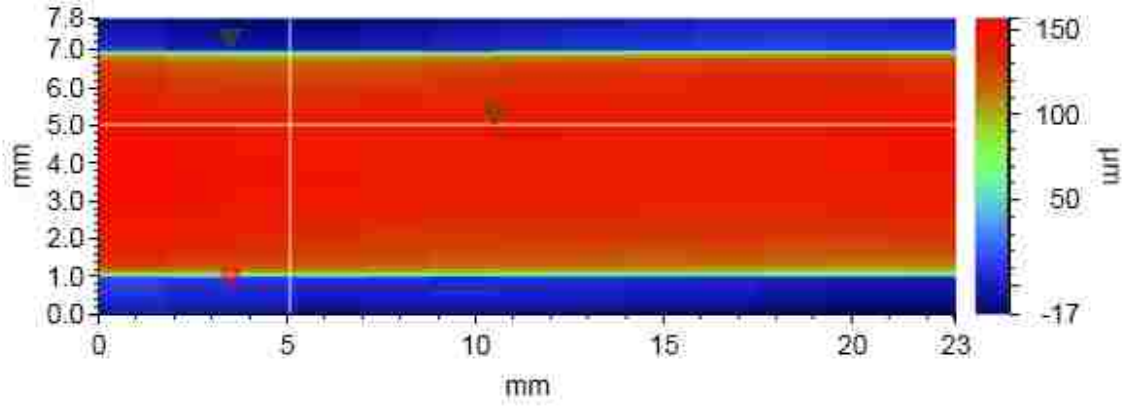

Figure 13: Plan-view map scan using Bruker DektakXT surface profiler system of 76.2 µm sample with crystallized HNAB deposited onto the surface and is capped by Parylene C.

These measurements were taken with the Bruker DektakXT surface profiler system. A "map scan" was completed with 13 separate measurements taken along the length of the substrate. As can be seen in the Figure 13, the red hue shows the thickness of HNAB compared to the blue hue of the tantalum. The map scan shows that the HNAB deposition was rather uniform along the surface. The results for each substrate can be found in Appendix F.

Another measurement with the DektakXT system graphically shows the thickness measurements from edge to edge (top to bottom in the plan-view orientation). This is shown in Figure 14.

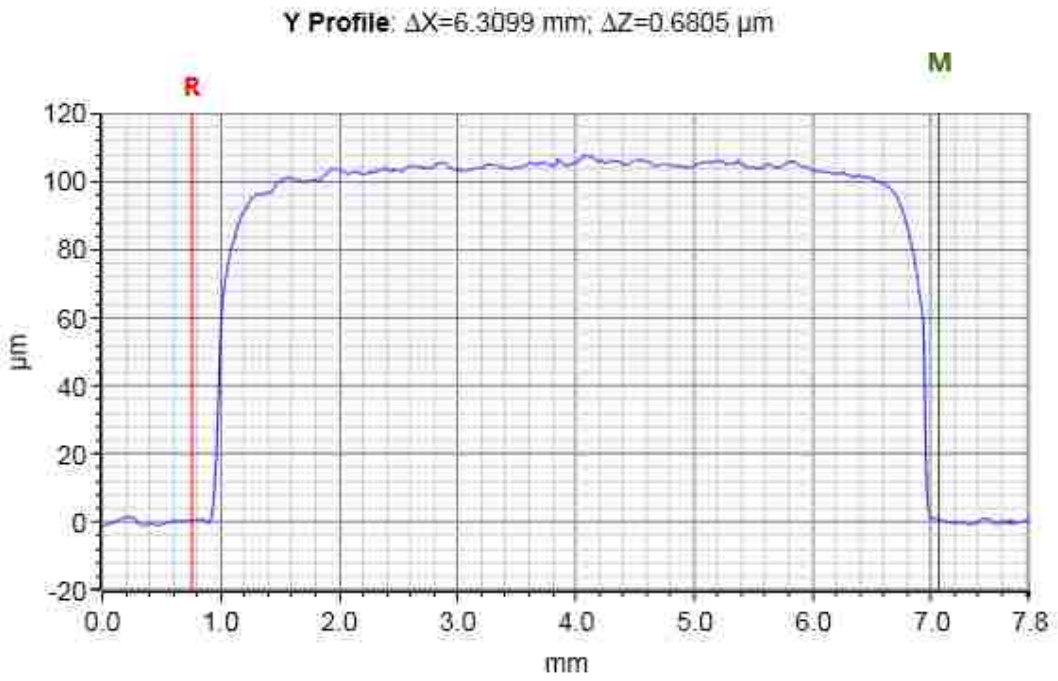

Figure 14: Graphical representation of the map scan thickness measurement on a 76.2 µm sample with crystallized HNAB that is capped by Parylene C.

The crystal density of HNAB-II is 1.744 g/cm^3 (Graeber & Morosin, 1974), but deposited and crystallized HNAB has a density of ~1.735 g/cm^3 (Knepper, et al., 2012). The deposition process is conducted under vacuum and the HNAB does not decompose at its melting point. Knowing this, and the dimensions of the deposited HNAB on each substrate (6 mm × 30 mm and 100 µm thick), the TNT equivalence of the fully assembled sandwich with approximately 200 µm thick HNAB can be calculated. The initiation apparatus is known to add ~10 mg of TNT equivalence to the fully assembled micro-sandwich system. This means that the micro-sandwich itself must be less than or equal to 100 mg of TNT equivalence. The calculation for the TNT equivalence of the substrates with the initiation apparatus is

$$TNT_{equiv_{Substrate}} = 10\ [mg] + l \times w \times t \times \rho \times 112\% \quad (11)$$

$$= 10\ [mg] + (3\ [cm])(0.6\ [cm])(0.02\ [cm])(1.765[\frac{g}{cm^3}]) \times 112\%$$

$$= 10\ [mg] + (0.0712\ [g])\left(\frac{1000\ [mg]}{1\ [g]}\right) = 81.2\ [mg]$$

where l is the length of the substrate, w is the width of the substrate, t is the explosive thickness of the fully assembled sandwich, and ρ is the density of the substrate.

Thus, the TNT equivalence for the fully assembled sandwich, consisting of two of the HNAB substrates and the initiation apparatus, is 81.2 mg which is under the mass limit of 110 mg for the micro-boombox.

2.2 Materials

2.2.1 Framing Camera

The framing camera is a SIMX High Speed Framing camera from Specialised Imaging. It is capable of taking up to a billion frames per second and was used to measure the liner angle during the experiment. It consists of 15 separate intensified CCD sensors that eliminate any lag or ghosting of the camera. A description of the framing camera was presented in the Diagnostic Equipment section of this thesis.

2.2.2 Streak Camera

The streak camera for this experiment is an SC-10 model streak camera by Optronis. It could be used as a back-up diagnostic to measure the vertical (detonation direction) component of the detonation velocity. A description of the streak camera is in the Diagnostic Equipment section of this thesis.

2.2.3 Illumination source

The illumination source for this experiment is a SILUX-640 spoiled coherence laser illumination source. This was used to backlight the experiment, providing light that was obscured from the camera due to liner motion. The laser was located outside of the micro-boombox during the experiment. The laser shined through one of the windows of the micro-boombox and was reflected off of a mirror onto the micro-sandwich setup. The reflected laser light was incident into the camera lens during the experiment.

2.2.4 Photonic Doppler Velocimetry (PDV)

The PDV system used in this experiment is a Sandia-developed custom system. It was used to measure liner velocity and "track motion in a frequency encoded temporal electro-optical signal, velocity information is preserved and allows for multiple velocity components to be recorded simultaneously" (Valenzuela, et al., 2007).

The system used a Thorlabs Single Mode GRIN Collimator probe. This is shown in Figure 15.

Figure 15: The Thorlabs PDV probe used in this experiment (Thorlabs, 2016).

The probe is designed for the 1550 nm laser that was used with it. The PDV probe was located inside the micro-boombox during the experiment.

2.2.5 Tantalum Substrate (liner)

Three different thicknesses of tantalum were tested, 50.8 µm, 76.2 µm, and 101.6 µm. Initial calculations found the 50.8 µm thickness to be sufficient. The experimental results tested this assumption. The substrates all have dimensions of 10 mm × 30 mm. The substrates all have HNAB vapor deposited onto the surface.

2.2.6 Framing Fixture

An apparatus was designed to support the tantalum/ high explosive (HE) sandwich together. This had access ports for the diagnostic equipment. A mock setup of the fixture was created without any HE in order to evaluate the size of the fully-assembled fixture within the confines of the micro-boombox shown in Figure 16.

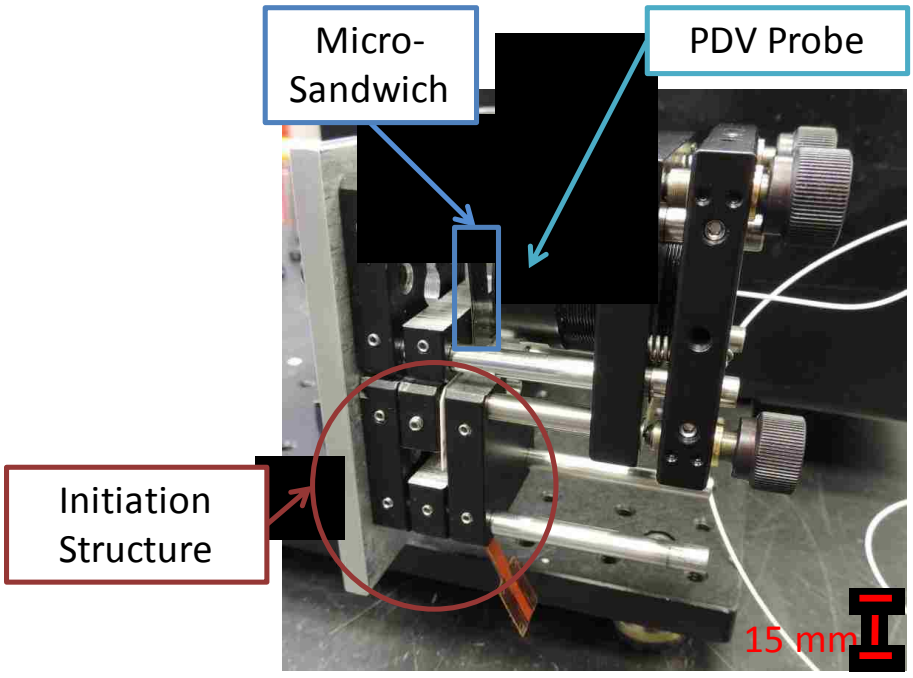

Figure 16: Photograph of the micro-sandwich assembly inside the fixture.

The assembly is constructed on Thorlabs 30 mm cage plates that have been modified for this experiment. The micro-sandwich is glued into a modified cage plate such that the sides of the sandwich can be viewed by the cameras. This modified cage plate is shown in Figure 17.

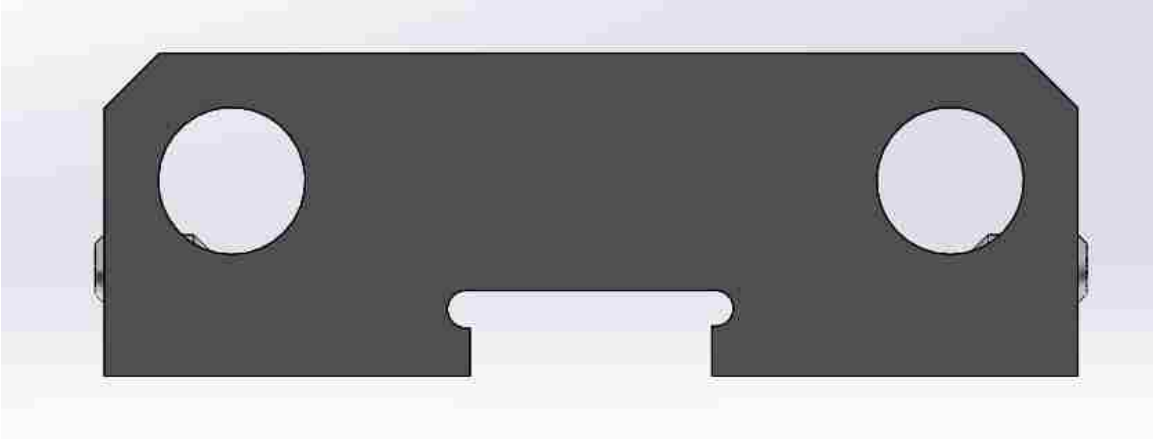

Figure 17: Plan-View of a SolidWorks drawing of the modified cage plate used to hold the micro-sandwich during the experiment.

The cutout on the cage plate is to the dimensions of the micro-sandwich with rounded corners. These rounded corners are useful for the process of applying epoxy to securely hold the micro-sandwich to the cage plate. The bottom sandwich substrate is placed with the HNAB face-up into the cutout of the cage plate with a 1 mm spacer placed on top of it. Sylgard® 527 adhesive is added along the length of the HE. Next, the other half of the sandwich is placed with the explosive face-down on top of the adhesive covered substrate, but not covering the 1 mm spacer. This means that the top substrate of the sandwich is offset by 1 mm from the bottom portion of the sandwich. Once the adhesive cures, the sandwich is epoxied into place with 5-minute epoxy. An image of the pre-assembled sandwich before adding the Sylgard 527 adhesive is shown in Figure 18.

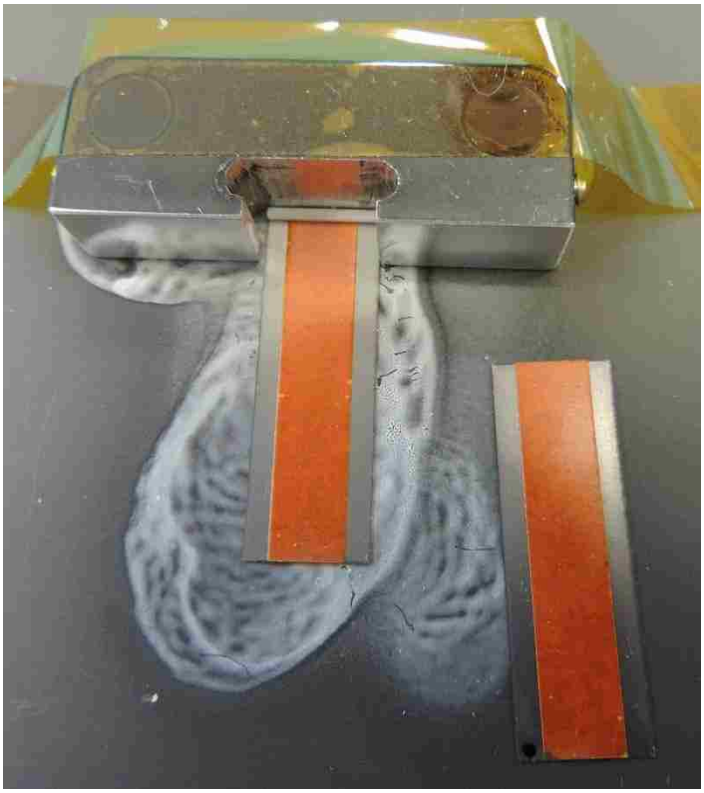

Figure 18: Image of pre-assembled sandwich with mold release agent to prevent adhesion to the flat surface where assembly took place.

Mold-release agent sprayed beneath the sandwich and cage plate appears as white residue in Figure 18. This was used to ensure that the micro-sandwich would not adhere to the flat surface it was assembled on. The bottom portion of the cage plate houses the initiation structure such that a 1 mm portion of the initiation structure is acting on the sandwich. It is used to ensure full contact between the 1 mm portion of the micro-sandwich that is offset below the rest of the sandwich and the 1 mm portion of the initiation structure that is offset above 1 mm from the 30 mm cage system on which it is attached.

A small amount of Parylene C was removed from the face of the sandwich in order to ensure that the PDV laser system had a clear view of the tantalum. A zoomed-in image

of the fixture with full assembly including an alignment laser being used with the PDV probe is shown in Figure 19.

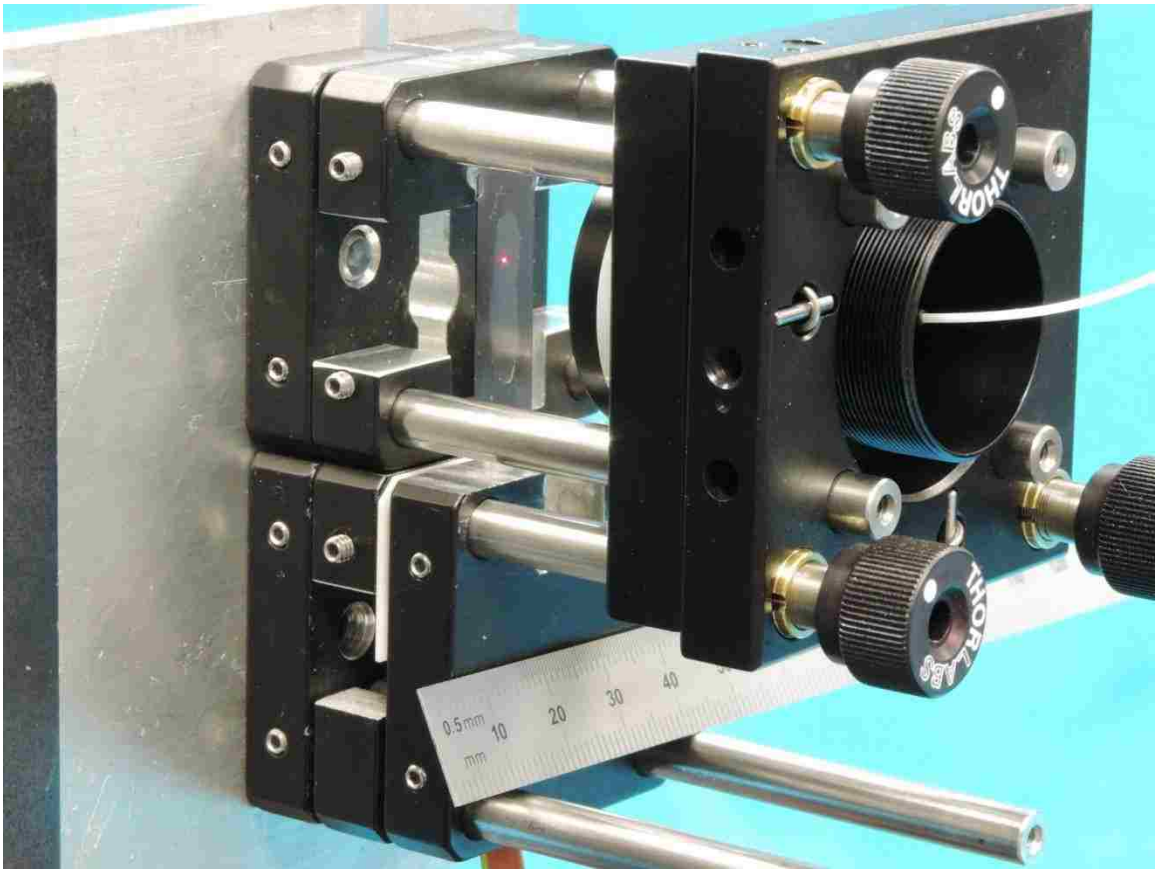

Figure 19: Image of the sandwich assembly fixture with the PDV probe using a red alignment laser to show where the PDV probe laser was located during the experiment.

The initiation structure is assembled separately from the top/sandwich portion of the fixture. The initiation structure is used to cause the detonation of the micro-sandwich. The initiation structure consists of a small amount of pentaerythritol tetranitrate (PETN) explosive that is initiated by a plastic slapper. The PETN initiation was chosen because it has low explosive mass, and it can be shock initiated by a high voltage slapper to initiate HNAB. The slapper utilizes synchronization of diagnostics and allows the use of a small quantity of explosives for ignition.

A high voltage firing set bursts a foil that accelerates a plastic slapper to high velocity to "slap" the deposited PETN initiation and cause it to detonate. The PETN, attached to the micro-sandwich, detonates up its length until the point where it is attached to the 1 mm sandwich. When the detonation reaches the sandwich, it initiates detonation in the HNAB. The detonation propagates up the length of the sandwich, causing the liner to expand. The measured velocity at which the tantalum expands can be used to model the products equation of state (EOS) of the HNAB.

2.2.7 Physical Vapor Deposition of HNAB

Explosive films made by physical vapor deposition (PVD) onto the tantalum substrate are measured using surface profilometry. The surface profilometry measurements were taken using a Bruker DektakXT system. The thickness of HNAB was chosen to be 100 μm thick, but was measured to range between 90.5 μm and 104.3 μm thick. The results for each substrate are listed in Appendix F. The HNAB films were found to be generally uniform across different depositions, which allowed for multiple samples to be made and crystallized, each of the same thickness and conditions. The vapor deposited HNAB has dimensions of 6 mm × 30 mm.

Directly following PVD, the HNAB is in an amorphous state that is put into an oven at 35°C in order to assist the crystallization process. The length of the crystallization process varies depending on substrate conditions between 1 week and 1 month.

2.2.8 Micro-Boombox

This experiment used an enclosure that is used specifically for explosive-related experiments, called a micro-boombox. It is a container in which the explosive detonation

takes place safely. This has an allowable TNT equivalence of 110 mg. Figure 20 shows an assembly diagram of the micro-boombox used in this experiment.

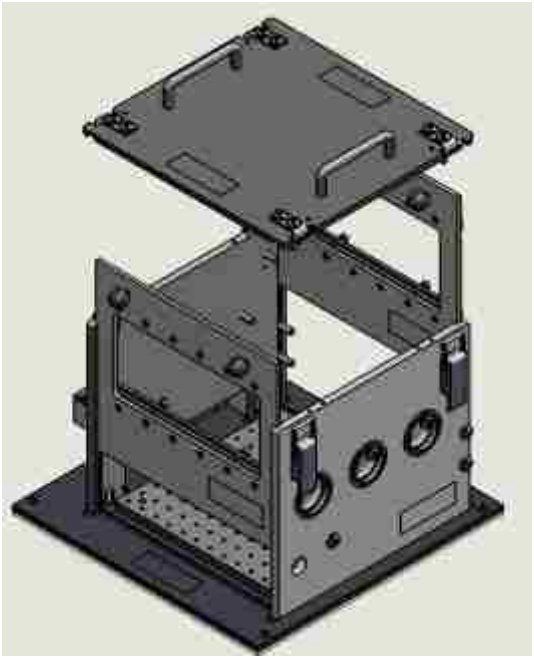

Figure 20: A SolidWorks drawing of the Micro-Boombox used in this experiment.

The micro-boombox limited the amount of explosive that can be used in the micro-sandwich as well as the size of the full micro-sandwich apparatus. The internal volume of the micro-boombox is approximately 0.0283 m^3 (1 ft^3), which must contain the entire micro-sandwich system, including initiation apparatus and PDV probes, as well as allow for clear viewing of the micro-sandwich by the measurement equipment.

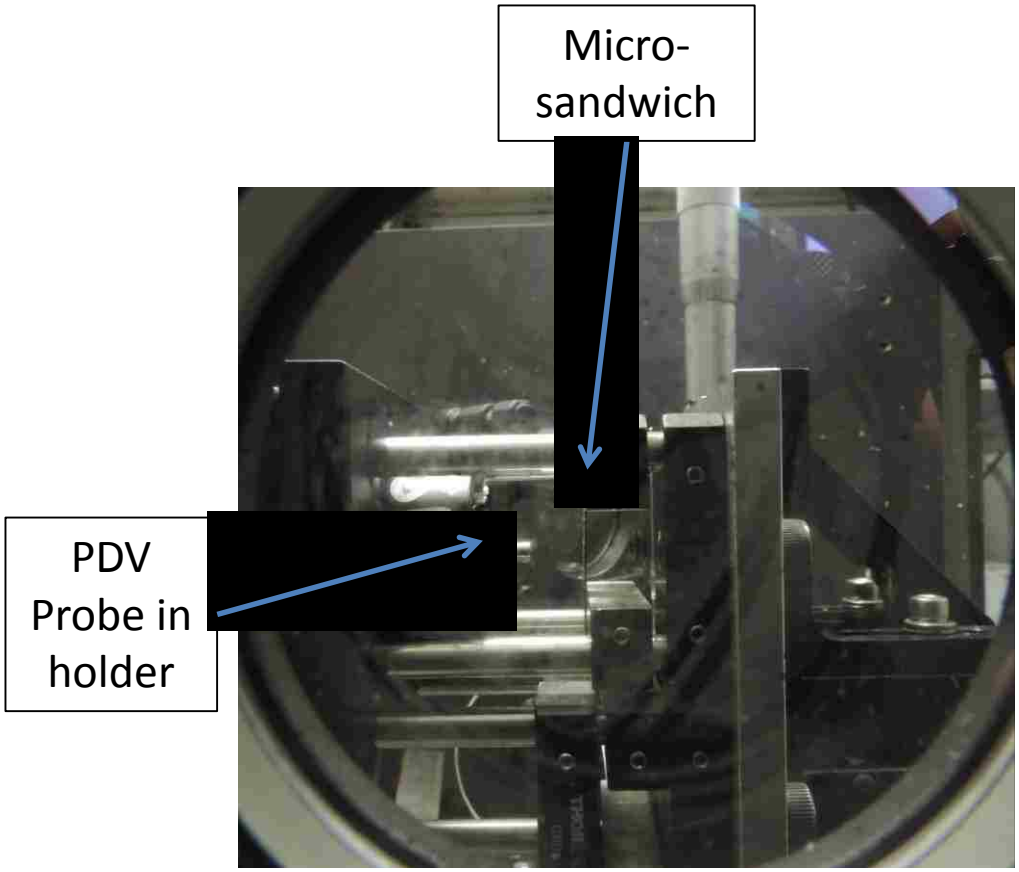

Figure 21: The camera view of the micro-sandwich and fixture inside the micro-boombox.

The framing and streak cameras both gained visual access to the experiment through the center circular window as shown in Figure 21. The experiment was backlit with a SILUX-640 laser that was located outside of the micro-boombox. The laser entered the micro-boombox using the rectangular window at the rear of the micro-boombox and was reflected from a small mirror that was located inside the micro-boombox. The PDV probes was located inside the micro-boombox during the experiment. The PDV probes was built into the fixture that held the micro-sandwich as well as the entire initiation structure.

2.3 Experimental Geometry

There are several areas of concern for the experimental geometry. First, the dimensions of the tantalum liner are crucial to the experiment. The tantalum liner must be large enough to allow for full access of all of the diagnostic equipment as well as small enough that the amount of HE that is deposited onto the surface does not experience too much stress. The desired dimensions of the tantalum substrate were 10 mm × 30 mm with the desired dimensions of HNAB deposited onto the surface of 6 mm × 30 mm × 100 μm.

Second, TNT equivalence of the fully-assembled micro-sandwich must be less than 110 mg. Using the dimensions of the deposited HNAB, it was determined that the TNT equivalence for the fully assembled sandwich, including 10 mg TNT equivalence of the initiation apparatus, was calculated as 81.2 mg, much less than the 110 mg limit.

Third, the location of the PDV probe during the experiment and its angle with respect to the liner are very important to the performance of the diagnostic in this experiment. The probe was located less than 2 cm away from the tantalum liner and was at an angle such that the laser has good reflectivity off the liner surface. This angle was determined experimentally before the experiment.

Finally, the setup for the rest of the diagnostic equipment and the illumination source is significant to this experiment. The framing camera, streak camera, and illumination source were all located outside the micro-boombox. The framing camera, streak camera, and illumination source all needed a clear view of the micro-sandwich during the detonation in order to collect data and measurements. This means that the frame that holds the micro-sandwich was designed to allow visual access for each of these three

pieces of equipment during detonation. The full experimental setup is shown in Figure 22.

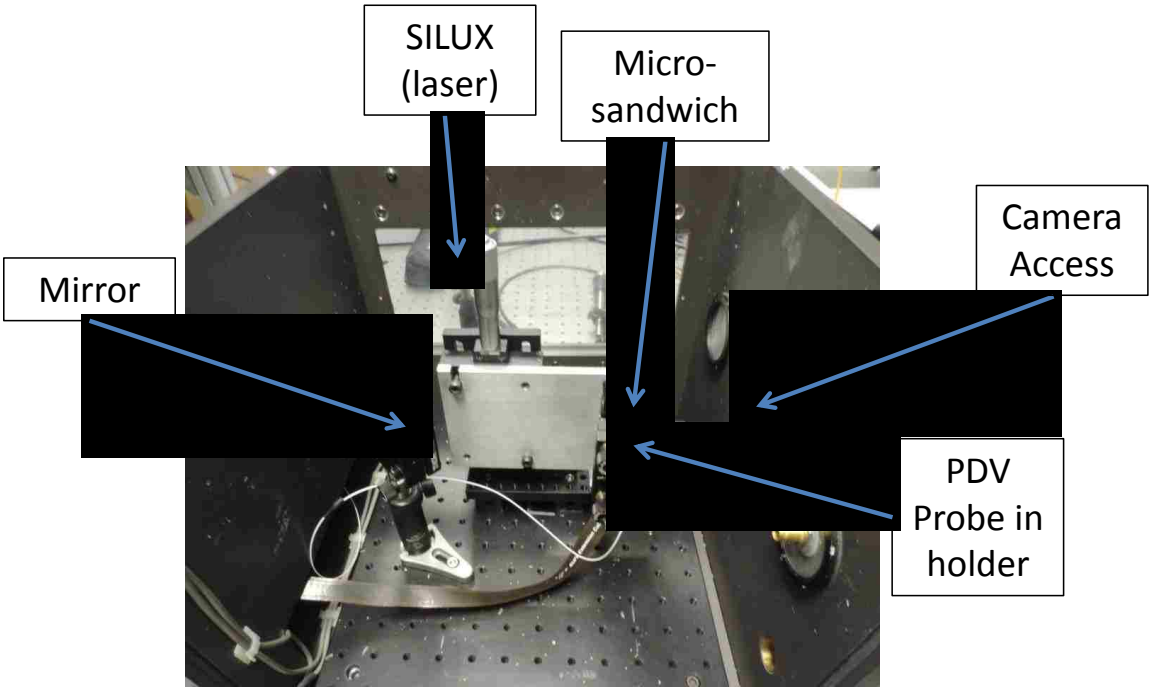

Figure 22: Image of the full setup inside the micro-boombox

The fixture was designed to fit inside the micro-boombox. It consists of several modified Thorlabs 30 mm cage plates. The mirror that was used in this experiment was a Thorlabs 2" front surface mirror. The only function of the mirror was to reflect light from the SILUX illumination laser into the cameras. The cameras gained visual access to the experiment through a circular window on the side of the micro-boombox. The camera system is shown in Figure 23.

Figure 23: Image of the SIMX and SC-10 Camera systems that were used in the experiment.

The camera systems were able to accurately capture the experimental data as desired. The SIMX framing camera was used to capture images of the sandwich as the detonation occurred. The framing camera data is one of the most important diagnostics for this experiment. The images from the framing camera were used to determine the angle of the liner for each thickness of the liner. The SC-10 streak camera was used to gather both time and position data of the sandwich during detonation. The streak camera data was used as complementary qualitative information.

2.4 Testing and Calibration

2.4.1 Parylene C Calibration

The high explosive (HE) must have full contact with the liner material in order to prevent air gaps or jetting that could invalidate the results of the experiment. Parylene C was selected as an adhesion material to promote the contact between the HE and liner.

Parylene C was investigated as an adhesion promoter in order to prevent cracking and lifting. Surprisingly, the Parylene C had the benefit of HNAB crystallizing almost exclusively to the HNAB-II phase. The process for Parylene C chemical vapor deposition process is shown in Figure 24.

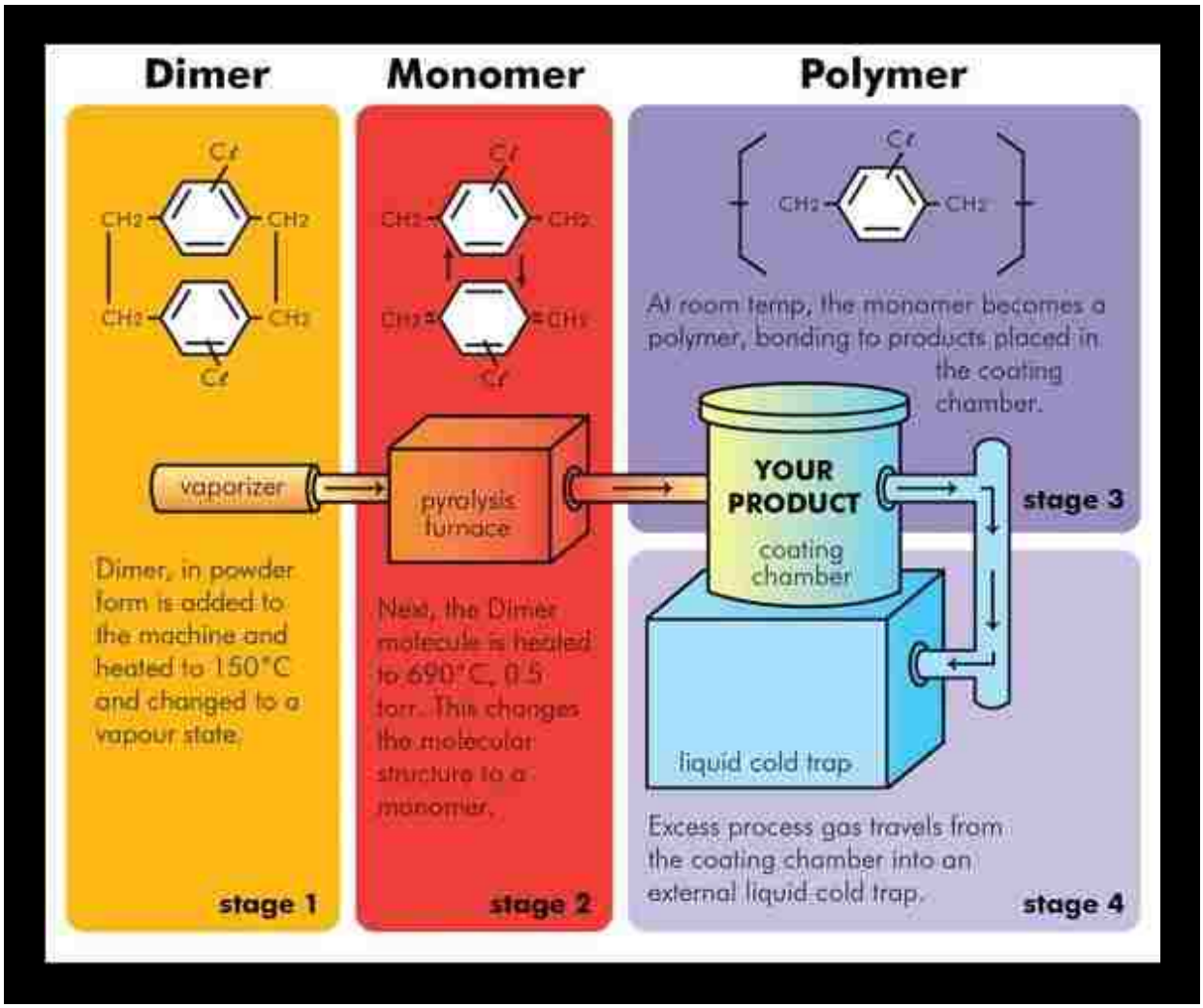

Figure 24: Process for chemical vapor deposition of Parylene C, from (Curtiss-Wright, 2016).

Parylene C is a conformal, protective, polymer coating that adheres to a variety of different material surfaces. It is deposited onto the surface of the substrates inside a coating chamber. It begins as a solid dimer in powder form that is put into a vaporizer. The Parylene C dimer is heated until the Parylene C becomes a vapor form. The Parylene C vapor next goes into a furnace where it is further heated until the dimer breaks into a monomer. The monomer Parylene C gas next goes into the coating chamber where the Parylene C polymerizes onto the desired substrates. Due to the nature of the coating

process, the entire chamber is coated in Parylene C. Any excess gas is sent to an external cold trap.

The coating chamber has a low temperature application process that occurs between 24 - 33°C, as experimentally measured. After the coating process, Parylene C has a relatively high melting point and a low permeability to moisture.

Several experimental runs were completed using the Parylene C coating chamber to determine the coating thickness based on input mass. Experimental data as measured using the DektakXT surface profiler system for Parylene C coating is shown in Table 1.

Table 1: Experimental Data for Parylene C Coatings

Parylene Mass (g)	Resulting Thickness (μm)
18	9.42
9	5.1
2.73	1.66

There is a linear relationship between the amount of Parylene C dimer that is put into the deposition chamber and the resulting thickness of the polymerized Parylene C, as shown in Figure 25. After fitting a linear equation to the data, it was determined that about 2.5 grams of Parylene C dimer should result in the chosen thickness of 1.5 μm of polymer.

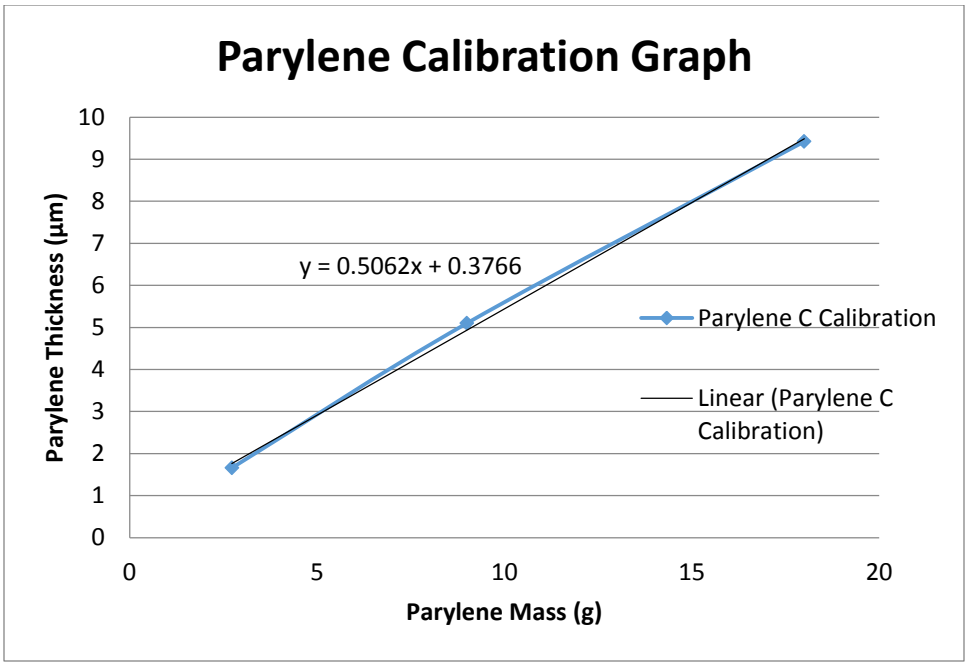

Figure 25: Parylene C calibration curve showing a linear relationship between the amount of Parylene C mass and resulting thickness.

A thin amount of polymerized Parylene is ideal for this experiment as it promotes adhesion of the HNAB onto the substrate without being so thick that it would impact the results. An initial adhesion test run was completed with 2.73 grams of Parylene C that resulted in a 1.66 µm thickness on the substrates as measured using the DektakXT surface profiler system. Adding an additional 2 µm thickness to the liner is insignificant compared to the liner which has a 76.2 ± 5 µm thickness so this should not affect the results. The initial adhesion test run determined that Parylene C coating of crystallized substrates prevented the HNAB from peeling off of the tantalum as well as promoted formation of the HNAB-II phase.

On the other side of the substrate, the small amount of Parylene C is removed from the tantalum in order for the PDV laser to have a clear view of the liner. This process was completed in order to prevent several potential errors, such as low reflection of the laser

light into the PDV probe, extraneous reflection of the laser light off of the Parylene C, and to prevent Parylene C from separating from the liner surface during detonation.

2.4.2 Setup Experiment

A setup experiment was completed in order to test several aspects of the experimental setup. The initial setup experiment was useful in testing that the fixture would work, testing the PETN ignition of Parylene C covered explosives, and testing the timing of the experiment for the cameras.

Because the micro-sandwich fixture is screwed onto a Thorlabs moving stage that is located inside the micro-boombox, the setup experiment helped to determine the best adjustments to the stage to allow the cameras full visual access to the micro-sandwich. Once the stage was set up, it did not move for the experimental tests because they were set up in the same way as the initial setup experiment.

The fixture was tested with less desirable substrates. The substrates were not annealed before deposition, but were coated in Parylene C as were the experimental substrates. First, a still image of the micro-sandwich was acquired while being backlit by the SILUX-640 laser. Next the initiation apparatus was detonated. There were no issues with the initiation of the setup experiment. Some images from the framing camera are shown in Figure 26.

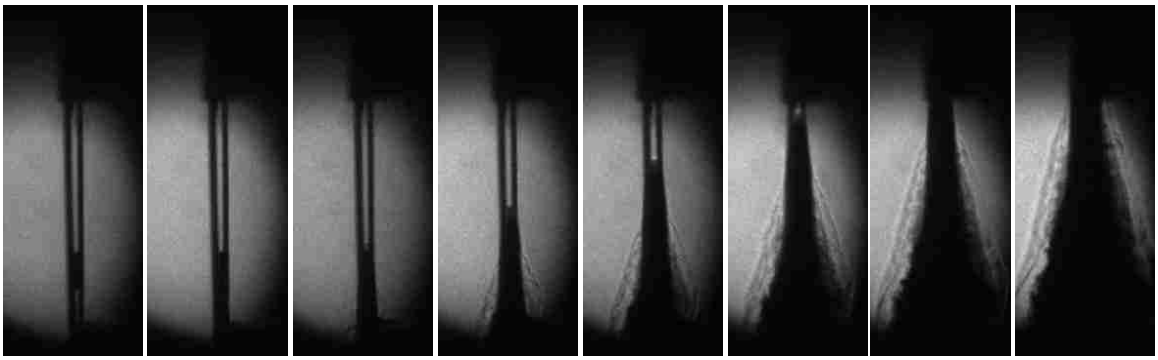

Figure 26: Setup experiment to test the fixture, initiation through Parylene C, and the timing for the cameras, at 5 ns exposure, 2.5 MHz (1/393 ns).

The fact that the substrates were not annealed before deposition meant that there was incomplete contact between the two halves of the sandwich. This can actually be seen in Figure 26 images where the separation between the two "halves" of the micro-sandwich resulted in less than desirable results. Jetting and air gaps made these results unsuitable. These results were useful in testing the setup and camera timing needed to produce desirable conditions for the experimental tests.

2.4.3 Experimental Tests

The experimental tests were carried out with the following protocol. The PDV probe was connected to the 1550 nm laser system. The probe was aligned until it was determined that maximum laser light was returned to the probe. Next, the probe was connected to a low-power 635 nm laser that is visible to the camera. A small wire was used to reflect light into the camera to show the location of the PDV laser on the sandwich. Some still images were taken with both the laser and wire in place to show the location of the laser light from the PDV probe on the micro-sandwich sample. Then the system was backlit with the SILUX-640 laser and more still images were taken. Finally, the initiation apparatus was connected to a high voltage source and detonation was initiated at high voltage. There were no issues with detonation, and data was successfully gathered from

the PDV system, framing camera, and streak camera. The data analysis for these micro-sandwich experiments yields liner velocity data that are used to inform explosive products EOS. This will be discussed further in the Results and Discussion section of this thesis.

3 Results and Discussion

In this section, the results of both deposition and detonation for four separate experiments is presented chronologically. The sandwich test data informed the development of the products equation of state (EOS) for the hexanitroazobenzene (HNAB) explosive.

3.1 Deposition of HNAB on Tantalum Substrate

The following sections will discuss the substrates. The images are all slightly skewed because of the way the images were taken. Using the Keyence VHX-5000 system to take the images, the substrates were not completely square to the imager when the images were taken. The images are all plan-view of a single piece of tantalum covered in crystallized HNAB with the following setup in Figure 27.

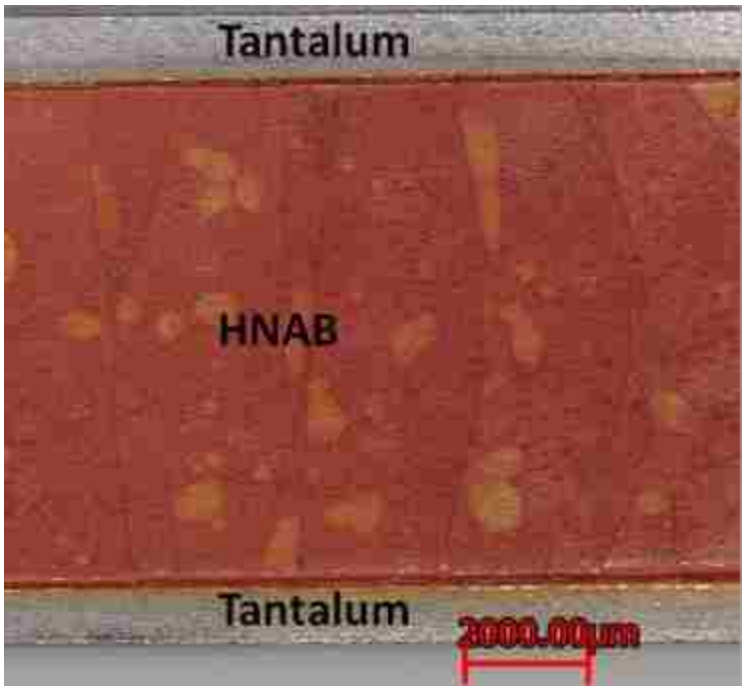

Figure 27: Plan-view of a single substrate that was regular-cleaned and crystallized at 35°C.

The figure shows the plan-view of a single substrate. It is a view from the top of a single tantalum substrate that has HNAB crystallized at 35°C on the surface. These single

substrates were paired and glued together to form the sandwich for this experiment. A diagram of the resulting sandwich is shown in Appendix A.

3.1.1 Tantalum Substrate Preparation Methods

Good adhesion of HNAB to the substrate is critical to this experiment. Any gaps between the explosive and the substrate will result in invalid results. Thus the proper preparation of the substrate is a very important part of this experiment to promote the correct crystallographic polymorph of HNAB to adhere to the tantalum substrate.

It has been previously noted that the physical vapor deposition of HNAB on a substrate has mixed results. The HNAB has a tendency to adhere to very specific surfaces, and a thin chromium layer has been used in past experiments where the HNAB would not adhere to the surface of a metal substrate (Tappan, et al., 2014). A thin chromium or Parylene C layer could be used in the case of the HNAB not adhering to the tantalum. Based on experimental results, the HNAB did not perfectly adhere to the tantalum substrate. Immediately after deposition, the HNAB was very cracked. After crystallization, light handling of the substrates resulted in delamination of the HNAB from the tantalum substrate. Ultimately, it was determined that the chromium or Parylene C adhesion layer would be needed.

Regular preparation methods were chosen for our substrates, as it yielded the best results. The regular preparation method consisted of cleaning the surface of the tantalum substrate with acetone, followed by ethanol. The method consisted of wiping both sides of the substrate with a wipe covered in acetone, waiting for the substrates to dry, and then wiping both sides of the substrate by a wipe covered in ethanol. The substrates were then

covered in a glass specimen dish in order to prevent any exposure to dust or chemicals before deposition.

The color difference between the phases of HNAB allow for easy determination of the crystallized phase. The unknown phase is a bright yellow color, whereas HNAB-II is either red or orange. There were generally more substrates with the correct form of HNAB on these surfaces based on the color of HNAB on the substrate. This is shown in Figure 28.

Figure 28: Plan-View of regular cleaned tantalum substrate with HNAB crystallized at 35°C.

The image shows a red/orange surface that has several yellow spots. The yellow spots correspond to the unknown phase of HNAB, where the red/orange color corresponds to the HNAB-II phase. Using the DektakXT surface profiler system, the thicknesses of the substrates were measured to range between 90.5-104.3 μm thick. The thickness of the HNAB was measured in several different locations on the substrate and found to be uniform. The regular cleaning method seemed to have promoted the HNAB-II phase, which is desired. The spots of the unknown phase were expected to develop, as this is a

known property of HNAB. The large cracks that resulted from the deposition process were not expected. Large cracks have the potential to cause lifting of the HNAB from the liner surface or even delamination of the HNAB off of the liner. The large cracks are indicative of stresses in the film that can affect adhesion.

Another method that was tested was to plasma etch the surface of the tantalum substrate that underwent the regular preparation. It was determined that the unknown phase of HNAB was promoted on the surfaces after crystallization. The difference between the plasma etched and regular cleaned substrates is shown in Figure 29.

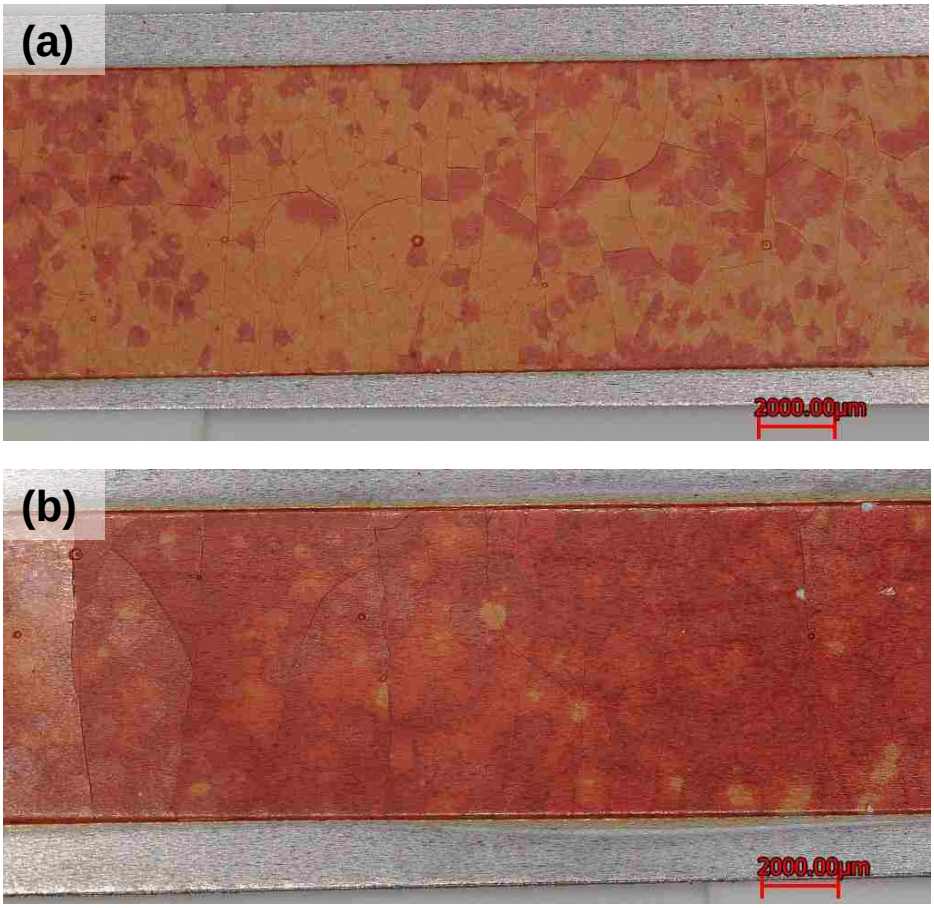

Figure 29: Plan-View of two images of HNAB films on tantalum substrates after crystallization at 35°C using (a) plasma etching cleaning method and (b) regular cleaning methods. Color difference due to unknown phase of HNAB (yellow) and HNAB-II (red/orange).

The prominent color differences are due to the fact that the plasma etched surface (a) seemed to promote the unknown phase of HNAB during crystallization. The other image (b) shows the regular cleaned substrate that has only a few spots of the unknown phase of HNAB, with the rest being HNAB-II. Even though there are spots of the unknown phase of HNAB on the regular cleaned substrate, it can still be detonated. In order to detonate the explosive substrate, there needs to be an uninterrupted path of HNAB-II phase (red/orange color) along the length of the substrate (left to right on the image). The unknown phase of HNAB is not detonable in this configuration. This means that any unknown phase of HNAB will not detonate like the HNAB-II. Each substrate will have at least a few spots of the unknown phase of HNAB on them, but by minimizing the amount of unknown phase in the substrates, better results will be produced.

Large cracks can also interrupt the detonation path of the HNAB-II explosive. Large cracks are indicative of a gap between the different edges. Any large gap in the HNAB means that there is a possibility of lifting, delamination, or even jetting. Jetting via cracks has an effect on the liner that would invalidate the results. Additionally, the detonation front could be stopped and the detonation will not propagate throughout the entire substrate. An interrupted detonation would also invalidate the results of the experiment.

The main issue with the regular cleaned substrates is that they tend to have large cracks and some even have HNAB lifting from the substrate in places. The HNAB deposited onto the substrate is very difficult to handle and is very brittle, which will make sandwich assembly incredibly difficult or impossible.

3.2 Substrate Stresses

The HNAB that was deposited onto the tantalum substrate without an adhesion layer showed cracking and lifting from the substrate. There are several potential sources of stress that explain the cracking of the HNAB, including residual stresses in the tantalum and stresses that result from the deposition and crystallization processes. The HNAB was very brittle and any attempts to handle the substrates resulted in pieces of HNAB cracking off and peeling away. The amorphous HNAB that was deposited onto the substrates showed cracking immediately. The cracks stayed the same during the crystallization process, meaning they did not worsen or improve. This is shown in Figure 30 and Figure 31.

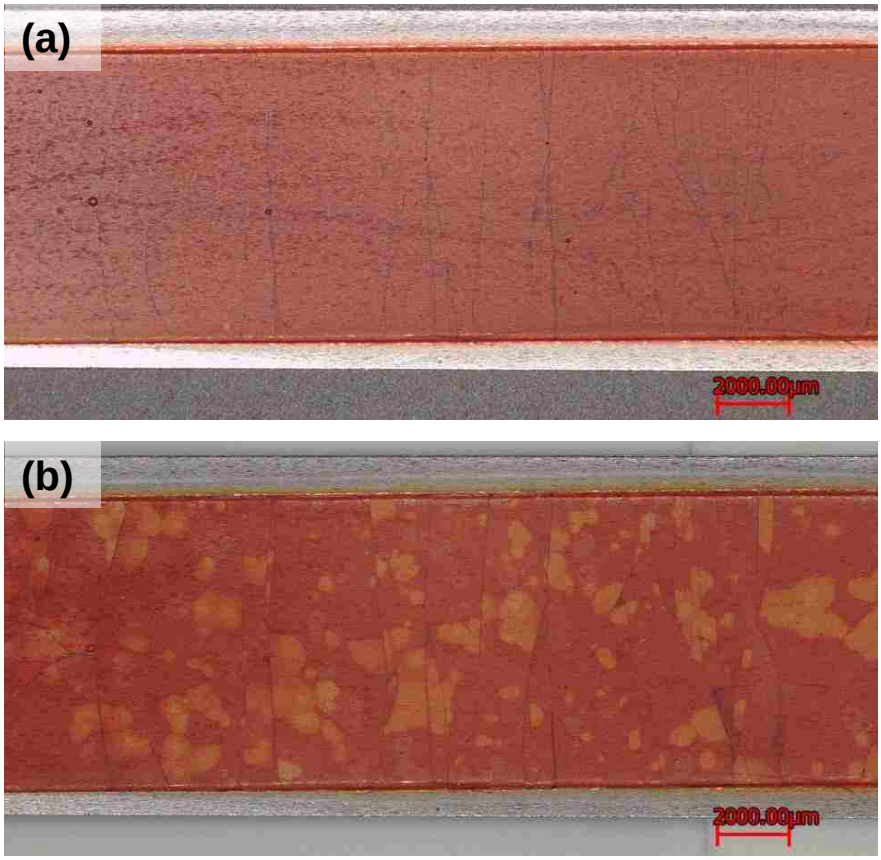

Figure 30: Plan-Views of two images of HNAB films on tantalum substrates before crystallization (a) and after crystallization at 35°C (b) using regular cleaning methods.

The amorphous HNAB appears as uniformly dark red color Figure 30 (a). The crystallization process did not show a visual change in cracks. Substrates were found to have brittle HNAB that did not allow the substrates to be handled without delamination. The main difference between the regular cleaned substrates and the plasma etched substrates was the phase of HNAB that resulted on the surfaces. There was not a noticeable difference between the substrate types with regards to the cracks in the films. In both cases, the cracks stayed relatively the same during the crystallization process, but with some resulting lifting.

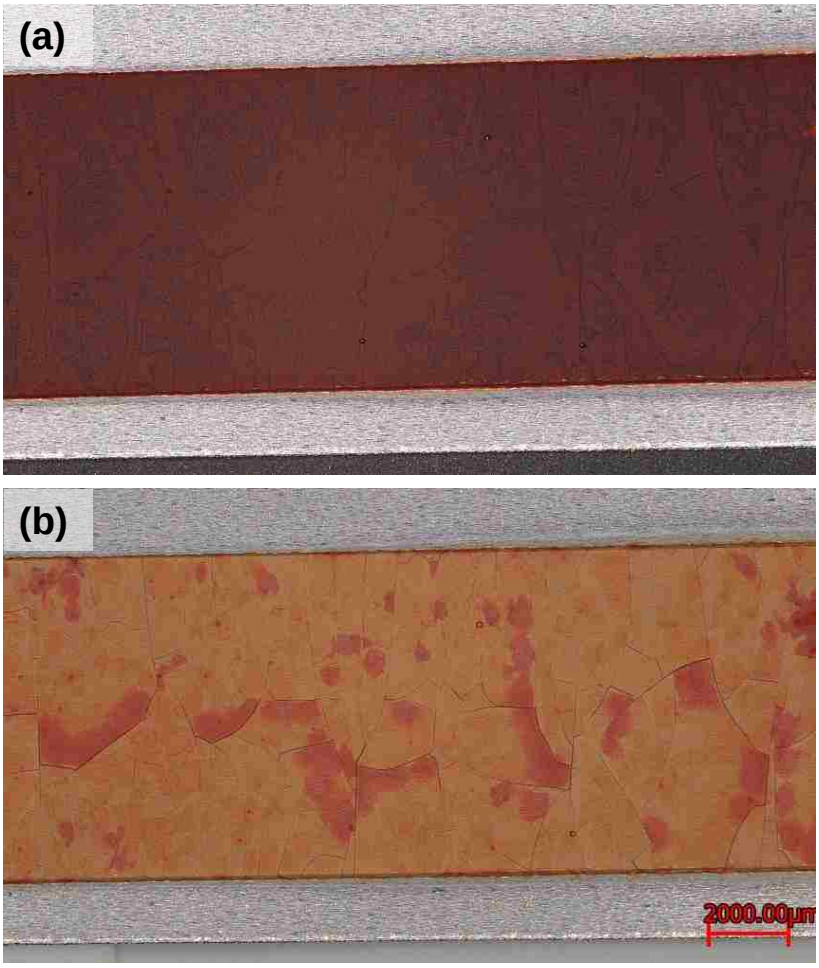

Figure 31: Plan-Views of two images of HNAB films on tantalum substrates before crystallization (a) and after crystallization at 35°C (b) using plasma etching cleaning methods.

The cracks that developed during the deposition process stayed relatively the same during the crystallization process, but lifting resulted. The lifting of the HNAB off of the substrate is due the crystallization process which caused stresses to develop in the film. HNAB was crystallized at 35°C in an oven that is specially used for explosive samples.

Coefficient of thermal expansion (CTE) mismatches are likely causing some of the stresses in the film. There is a CTE mismatch between tantalum metal and HNAB. The HNAB deposition process occurs around 20°C, but the tantalum substrate heats up slightly during the process as the HNAB condenses onto it. Both the tantalum and HNAB reduce in size as the temperature lowers, but at different rates. This causes the HNAB to crack as the substrate cools down. The tantalum/HNAB substrates are subjected to additional heat inside the oven during the crystallization process, which causes more stresses to be introduced into the substrate. The CTE differential expansion can be the cause for the lifting of the HE from the liner.

Other sources of stress in the substrate may be due to the orientation of the tantalum during the deposition process. The curvature of the substrate during deposition seems to have a large impact on the resulting crystallized substrate. For this reason, the substrates were annealed.

3.2.1 Annealing

The substrates were cleaned using acetone and ethanol. The substrates were placed on smooth alumina and had weight added on top. They were placed under high vacuum (~3.7 × 10-7 torr) in a furnace. The furnace was heated at a rate of 10°C/minute until

100°C was reached. The temperature then was increased at a rate of 8 1/3°C/minute until 1250°C was reached. The substrates were kept at 1250 °C for 60 minutes. For the cool-down process, the furnace was cooled at a rate of 12°C/minute until the cooling process was no longer driven. At this point, the cooling of the substrates became an asymptotic process that was no longer controlled. The annealing process is shown graphically in Figure 32.

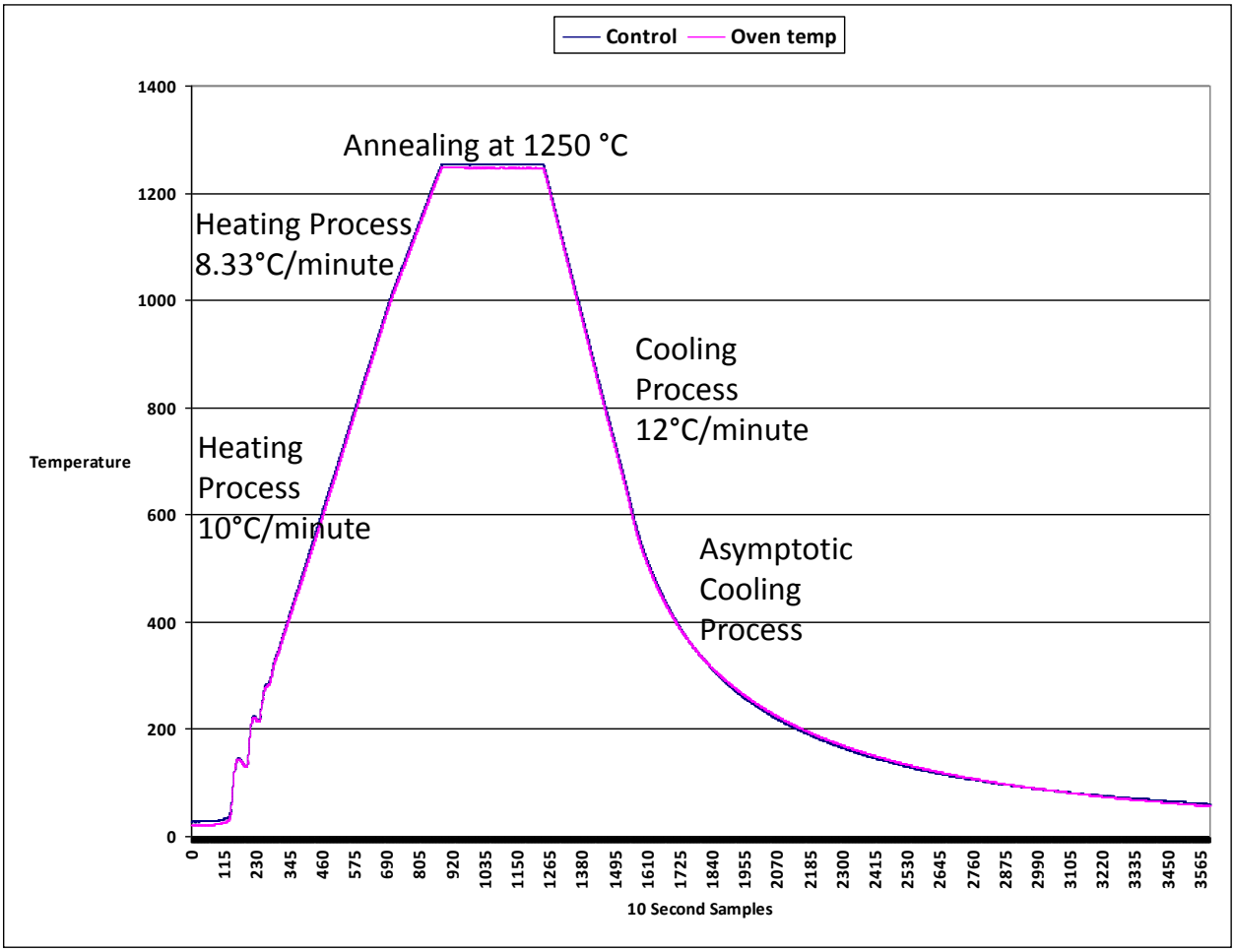

Figure 32: Graphical representation of annealing process.

The process was kept at or below 1250°C in order to not change the chemistry of the tantalum foil. It was determined that around 1350°C is where the tantalum would

become oxidized, which significantly increases the hardness of the material (Richards, et al., 2003). The annealing process was very successful.

The flat annealed substrates performed much better during deposition than the slightly curved substrates in terms of viability for this experiment. The flat substrates had fewer stresses in the film, allowing for easier handling of the substrates.

3.2.2 Mask Sizing

The deposition process uses mask coverings in order to hold the substrates in place during the process. These masks also designate what areas get deposited on. They act as a sort of stencil that allows the HNAB to be deposited only onto certain desired areas of the substrate. There were two different size masks that were considered for this experiment, an 8 mm wide mask and a 6 mm wide mask. Both masks allowed for deposition onto the full 30 mm length of the substrate. Experimental results found that the 6 mm mask was better suited to this experiment. The 8 mm mask resulted in greater cracking of the HNAB as well as more lifting. The 6 mm mask resulted in fewer cracks in the film and easier handling of the substrate.

3.2.3 Substrate Adhesion Layer

Initial tests showed that HNAB did not adhere very well to the tantalum substrate. The HNAB was very cracked, which made it difficult to handle the substrates. Light handling of the substrates resulted in some HNAB delaminating off of the tantalum, which would not allow for sandwich assembly. Additionally, in some cases the large cracks caused the HNAB to lift from the surface of the tantalum. This is an issue for the experiment, as HNAB lifting from the tantalum substrate means that full contact between the HE and

liner is not fully achieved. These cracks also mean that the HNAB layer on the substrate is very brittle and is therefore very difficult to handle the substrate without damaging the substrate. It is imperative that the HE has full contact with the liner material in order to prevent air gaps or jetting during the initiation process. Either air gaps or jetting could invalidate the results of the experiment. The contact between HE and liner must also be strong enough for the sandwich to be assembled without any of the HE lifting or delaminating. Some lifting, cracking, and HE delamination is shown in Figure 33.

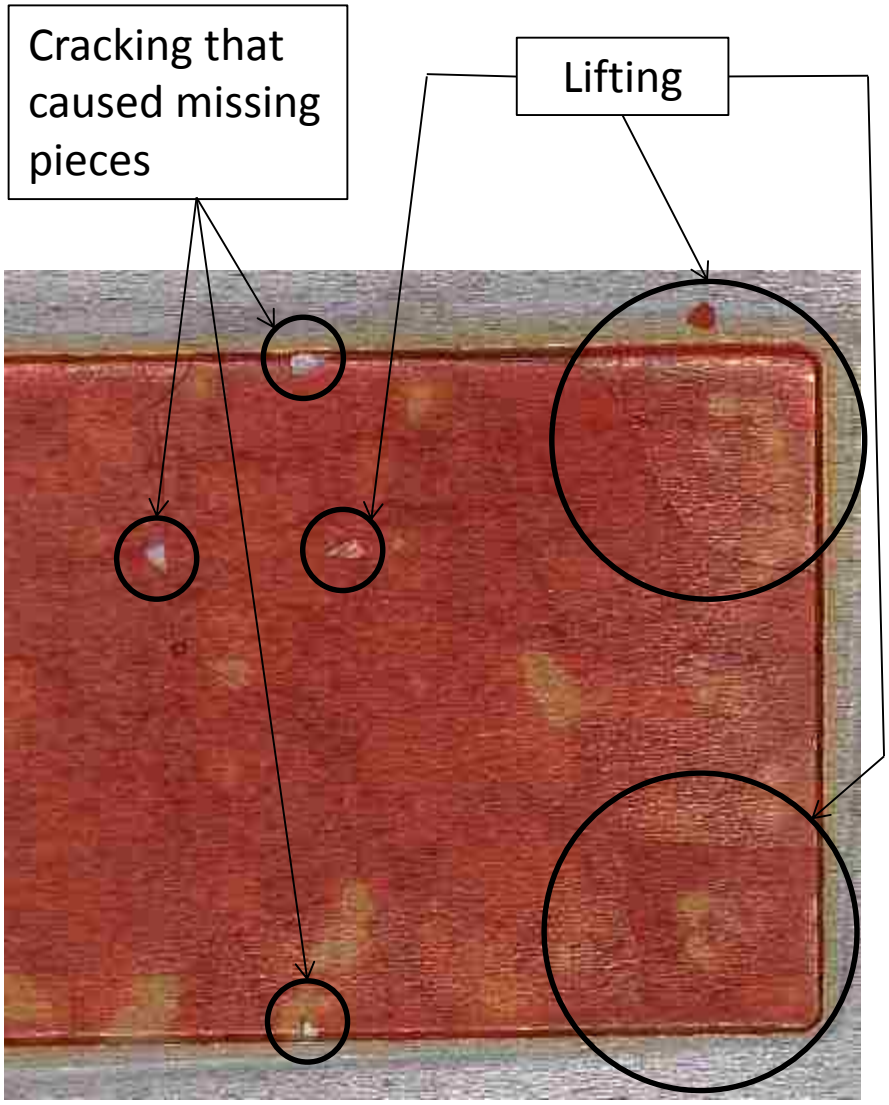

Figure 33: Plan-View of HNAB crystallized on tantalum at 35°C. The substrate shows lifting, cracking, and HE delamination which causes missing pieces.

The delamination of the HNAB off the tantalum surface can be easily seen by the distinct color difference of metal inside the red of HNAB. These missing pieces are a strong indicator that the HNAB did not adhere to the tantalum substrate effectively. This means that an adhesion layer must be used.

There were two different materials tested for adhesion between the HNAB and tantalum substrate, Parylene C and chromium. The Parylene C coating was chosen due to the fact that HNAB has a history of consistently adhering to plastic and acrylic surfaces. It was

also advantageous that the material and deployment system were readily available. On the other hand, chromium has been previously used in the case of vapor-deposited copper onto substrates where it helped to promote adhesion of HNAB (Knepper, et al., 2014).

Two depositions of 6 substrates each were completed to test the different adhesion layers. Deposition 1 consisted of 2 conditions. Essentially, the depositions were as follows:

Deposition 1:

- (3 each) Ta – Chromium – HNAB
- (3 each) Ta – Chromium – HNAB amorphous – Parylene C*

Deposition 2:

- (2 each) Ta – Parylene C – HNAB
- (2 each) Ta – Parylene C – HNAB amorphous – Parylene C*
- (2 each) Ta – HNAB amorphous – Parylene C*

*Several of the substrates were tested with a Parylene C coating of the deposited amorphous HNAB. These samples were coated with Parylene C before being crystallized in the oven.

The adhesion experiment that was completed had several interesting results. Overall, the methods used in Figure 34 (a), (b), and (d) resulted in promotion of the unknown yellow phase of HNAB, which is not desirable for this experiment. Figure 34 (a) and (b) also had too much lifting of HNAB from the tantalum substrate. The method used in Figure 34 (c) had more unknown yellow phase than the method used in Figure 34 (e). This means that the method used for Figure 34 (e) was used in this experiment, with both an

adhesion and capping layer of Parylene C. The results are shown in Figure 34 which correlates to the methods listed in Table 2.

Table 2: Description of adhesion and capping layers with correlation to plan-view images in Figure 31 after HNAB crystallized at 35°.

Image	Base Layer	Adhesion Layer	Explosive Deposition	Capping Layer
a	Tantalum	Chromium	HNAB amorphous	
b	Tantalum	Chromium	HNAB amorphous	Parylene C
c	Tantalum	Parylene C	HNAB amorphous	
d	Tantalum		HNAB amorphous	Parylene C
e	Tantalum	Parylene C	HNAB amorphous	Parylene C

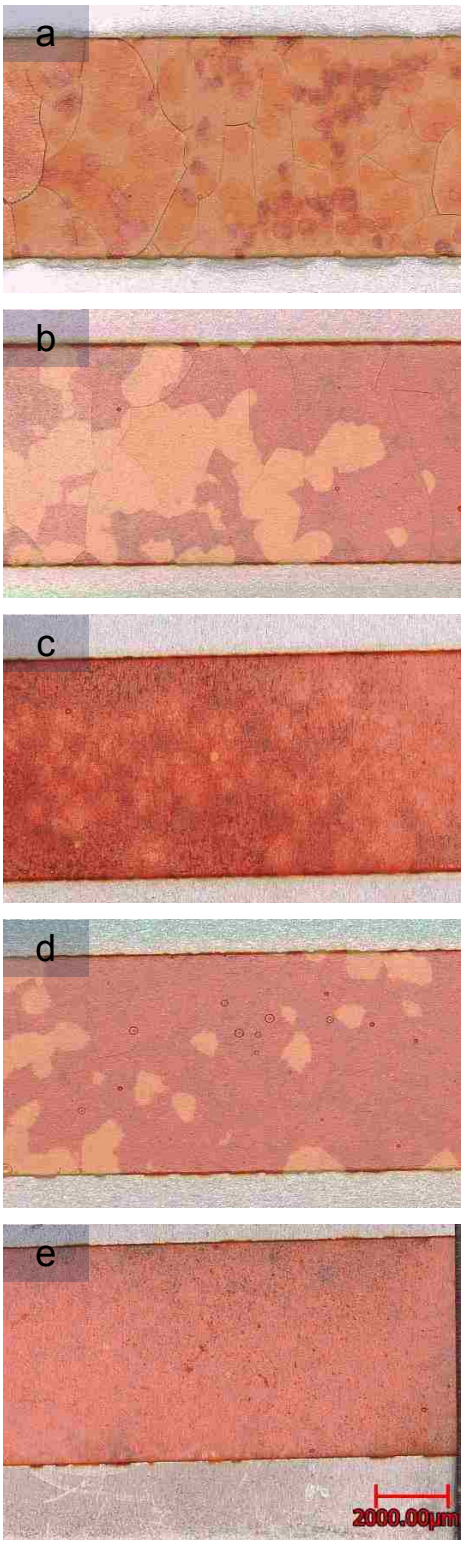

Figure 34: Plan-view images of HNAB adhesion layers that correlates to Table 2. HNAB was crystallized at 35°C.

These substrates were prepared as follows:

Deposition 1 consisted of 2 conditions. First, all 6 substrates were coated with about 50 nm thick chromium followed by about 100 µm thick HNAB. Next, 3 substrates were put into the oven to crystallize while the other 3 had about 1.5 µm thickness of Parylene C coating on the amorphous HNAB.

Deposition 2 consisted of 3 conditions. Of the 6 substrates, 4 were covered in about 1.5 µm thickness of Parylene C followed by about 100 µm thick HNAB. Next, 2 substrates were put into the oven to crystallize while the other 2 had about 1.5 µm thickness of Parylene C coating on the amorphous HNAB. The final 2 substrates had about 100 µm thick HNAB deposited directly onto the tantalum followed by about 1.5 µm thickness of Parylene C coating on the amorphous HNAB.

3.2.3.1 Chromium

Coating the tantalum substrate in a thin layer of chromium proved ineffective. The process occurs much the same way as the HNAB deposition. The tantalum substrates were covered in about 50 nm of chromium while inside the custom deposition chamber. Without breaking the vacuum seal, the HNAB was then deposited onto the chromium surface. Previous experiments have successfully used this chromium layer to promote the adhesion of HNAB onto copper substrates.

The chromium layer did not promote the adhesion of HNAB onto the tantalum substrate. There was significant cracking and lifting on the chromium substrates, as shown in Figure 35.

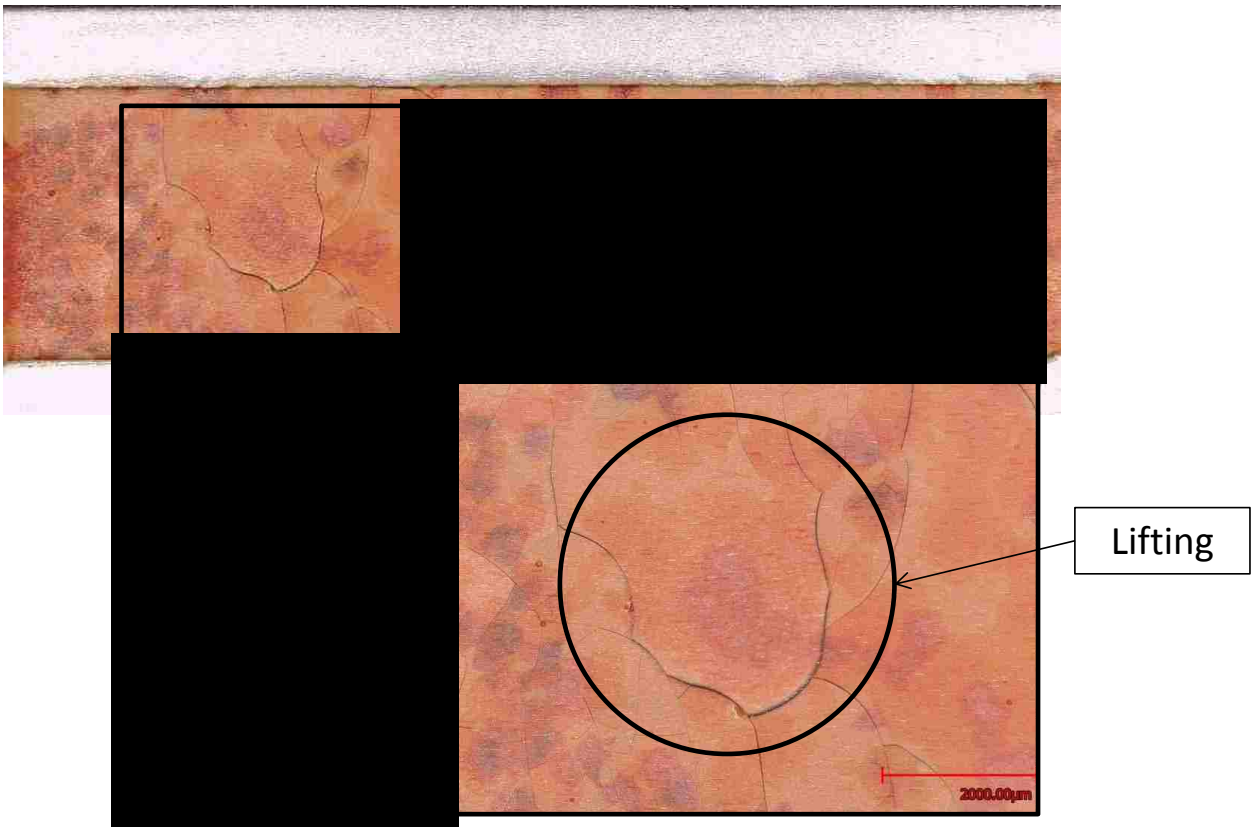

Figure 35: Plan-View showing cracking and lifting of HNAB crystallized at 35°C that was deposited onto chromium-covered tantalum.

Figure 35 shows that the chromium seemed to have the reverse effect from what was desired. The unknown phase of HNAB was promoted, with large cracks and lifting.

Additional experiments of Parylene C coating the amorphous HNAB on chromium proved effective. The HNAB was found to adhere well to the chromium-covered substrate with the Parylene C cover; the Parylene C prevented lifting and missing pieces. The Parylene C coating of the HNAB made the substrate easier to handle, as shown in Figure 36.

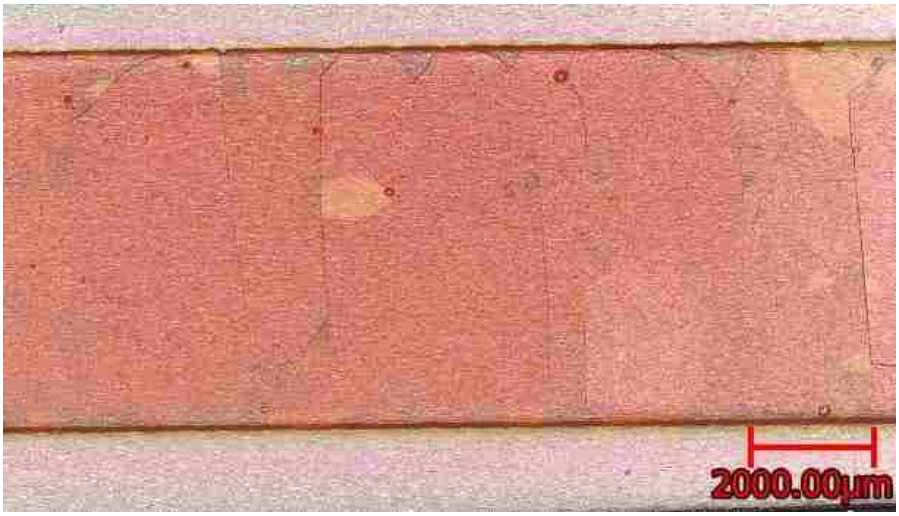

Figure 36: Plan-View of HNAB deposited onto chromium-covered tantalum. The amorphous HNAB was coated in Parylene C then crystallized in oven at 35°C.

While the chromium layer on the tantalum seemed to promote the unknown phase of HNAB with much cracking and lifting, the Parylene C layer seemed to have the opposite effect, as seen in Figure 36. The Parylene C seemed to promote the desired HNAB-II phase with little cracking and virtually no lifting. For this reason, the chromium layer was determined to be undesirable for this experiment and Parylene C was further explored.

3.2.3.2 Parylene C

The methods of testing were to coat the tantalum substrate in Parylene C coating using a Parylene coating chamber before and/or after HNAB deposition. Parylene C is a conformal protective polymer coating material. It is generally used to uniformly protect any component configuration. It adheres to many different types of surfaces. The Parylene C had no difficulty adhering to tantalum.

Previous experiments with HNAB revealed that HNAB adheres best to acrylics (such as PMMA), silicon, and plastics (Tappan, et al., 2014; Tappan, et al., 2015; Knepper, et al.,

2012). For this reason, Parylene C coatings were discussed as an adhesion layer to prevent the HNAB from lifting from the substrate.

Due to the fact that Parylene adheres to all surfaces, protecting the outer surface of the tantalum substrate from Parylene was deemed important. Only the surface that the HNAB is deposited onto was fully covered in Parylene. Due to the fact that the Parylene deposition process occurs with vaporized Parylene, the non-deposition side of the substrate could not be fully protected from the Parylene. This means that there are varying thicknesses of Parylene C coating on the non-deposition side of the tantalum substrate. These varying amounts are all less than the thickness on the deposition side of the substrate, with the center of the non-deposition side estimated to be approximately 0-0.1 μm thick. This allowed for accurate reading of the tantalum substrate during the detonation process of the experiment as measured by the photonic Doppler velocimetry (PDV) system. The Parylene C thicknesses varied between 1-2 μm on the deposition side of the tantalum.

The crystallized HNAB was found to adhere very well to the Parylene C covered substrate. Surprisingly, the HNAB-II phase seemed to be promoted by the chemical vapor deposition of Parylene C. This means that the Parylene C promoted adhesion of the correct phase of HNAB to the substrate. Additional experiments of Parylene C coating the amorphous HNAB also proved effective. The HNAB was found to adhere well to the substrate, with the Parylene C preventing lifting and missing pieces. The Parylene C coating of the HNAB made the substrate easier to handle without damaging the substrate.

3.3 Experimental Results and Data Analysis

Three micro-sandwich experiments were conducted. Three different liner thicknesses were investigated experimentally and the experimental data showed significant variation with tantalum thickness as expected. The liner angle was found to increase with decreasing liner thickness. Additionally, the liner velocity was found to increase as liner thickness decreased.

3.3.1 Data Analysis

The liner angle was determined for each thickness of tantalum. Media Cybernetics, Inc. Image-Pro Plus software was used to measure the liner angles and compare them to the initial backlit still images. The frames were compared to the corresponding still image frame. For example, if Frame 8 showed the liner expanding, the still image Frame 8 was used to determine the numerical value of the liner angle. A comparison of the different experiments is shown in Figure 37.

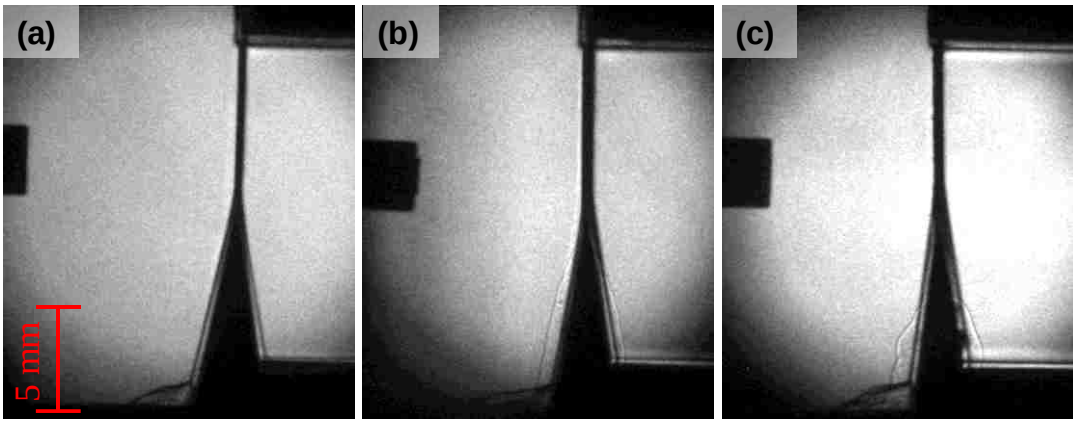

Figure 37: Framing camera images of the (a) 50.8 µm (2 mil), (b) 76.2 µm (3 mil), and (c) 101.6 µm (4 mil) thick tantalum experiment on HNAB micro-sandwich test, 5 ns exposure, 2.4 MHz (1/417 ns).

Surprisingly, the 50.8 µm experiment seems to have the best looking results. The images were clearer on the 50.8 µm experiment than the other two experiments; however, all

three experiments yielded useful data. The process that was used to determine the angles in Image-Pro Plus software is shown in Figure 38.

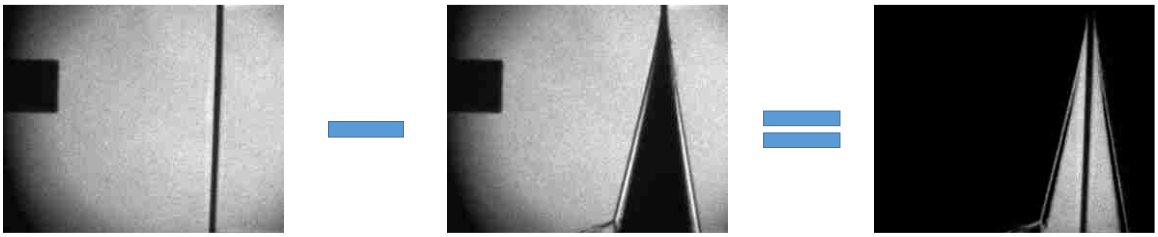

Figure 38: Pictorial representation of the mathematical process that occurred using Image-Pro Plus software to analyze framing camera images.

The detonation image that showed the liner angle was subtracted from the still image that corresponded to that detonation image. Next, measurements were taken using the same software. The angle was measured in 4 separate places on the image and the angle values were averaged. The greatest difference between a measurement and the average value is considered to be the error associated with that angle measurement. This process was repeated for each framing camera image that showed the liner angle during detonation. The full images from the framing camera can be found in Appendix D.

The PDV data analysis was much more complicated. Given that the experiment will be modeled in CTH as a theoretical particle moving on an expanding surface, the liner velocity as measured by the PDV is not the desired velocity. The material velocity is defined as the movement of a single theoretical tantalum particle during detonation. An exaggerated cartoon of the experimental geometry at and above the PDV laser location during detonation is shown in Figure 39.

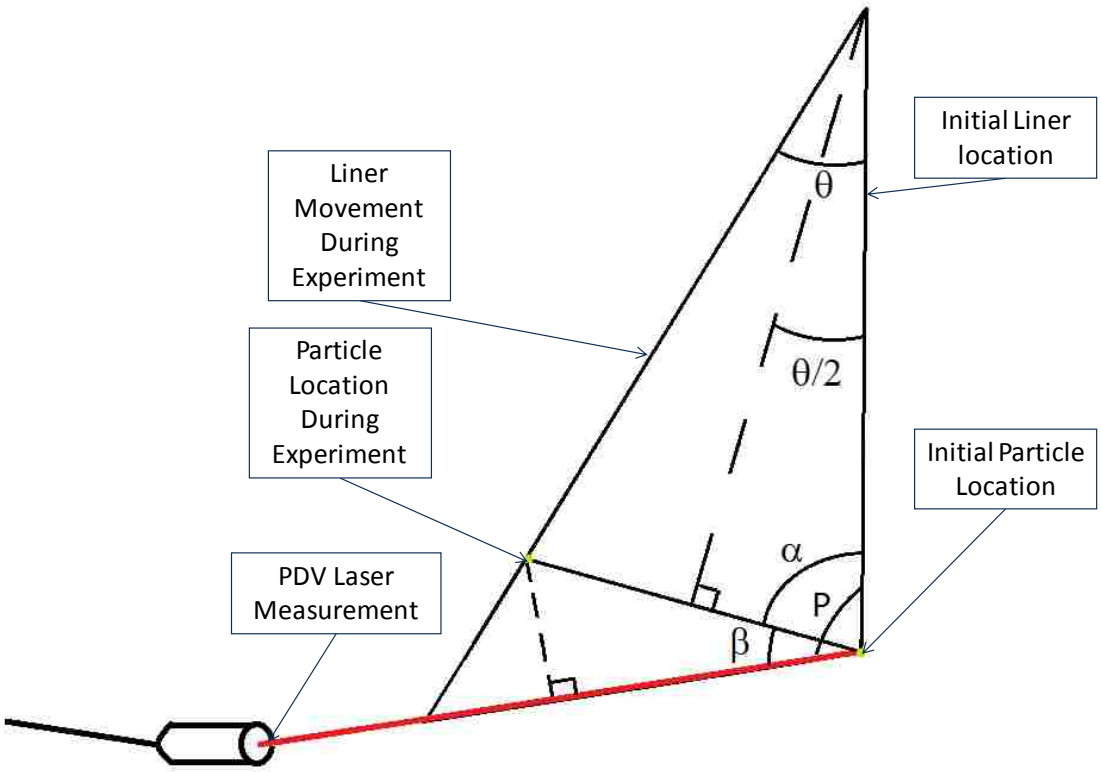

Figure 39: Cartoon of experiment geometry during detonation to aid in PDV analysis.

The assumption is that the liner does not stretch (Hill, 2002). This means that the liner length from the initial particle point to the top of the sandwich is assumed to be the same length after the liner expands during detonation. From this assumption, it can be determined that an isosceles triangle results between the initial liner location and the liner location during detonation, which simplifies the geometry of the analysis.

The PDV measures the liner velocity, but not the velocity of the particle. The velocity of the particle, denoted as material velocity, is at a different angle from the velocity measured by the PDV system. This is shown in Figure 40.

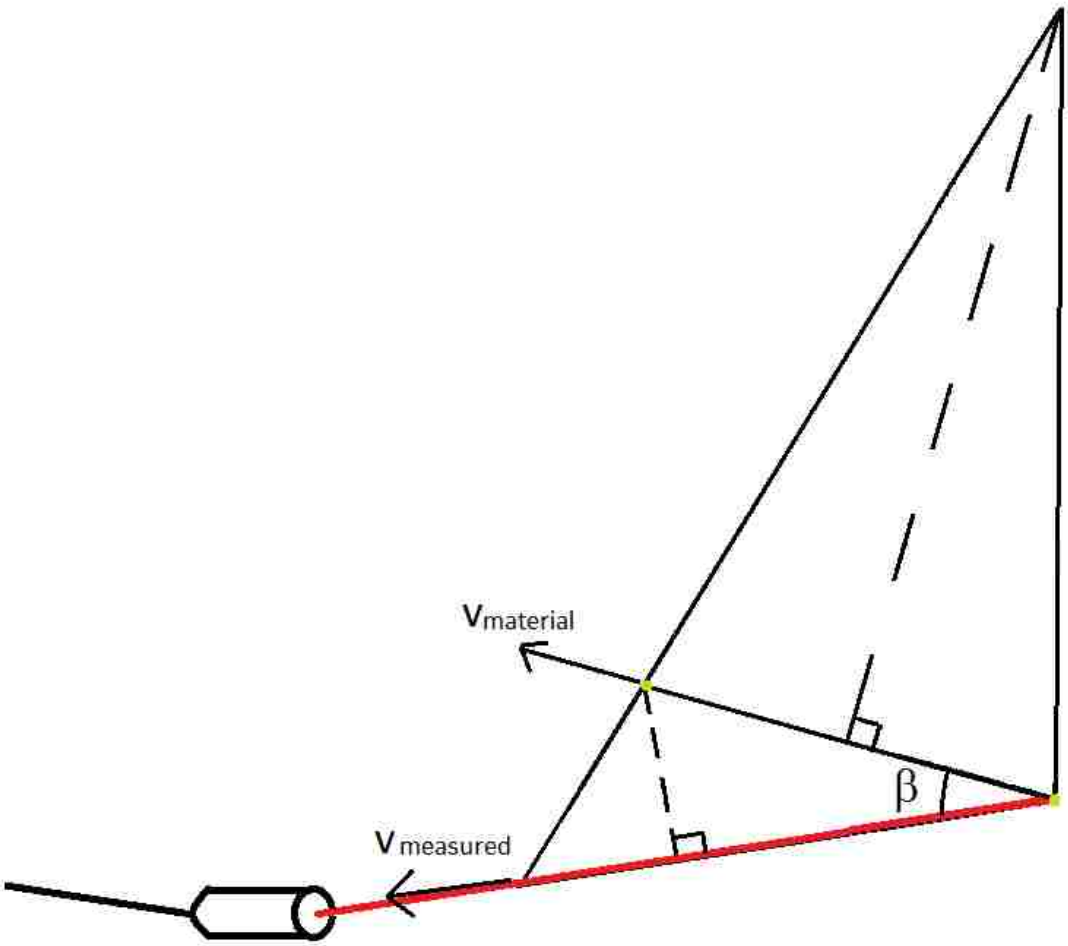

Figure 40: Cartoon of experiment geometry during detonation showing location of desired velocity vectors.

The angle between the two velocity vectors has been called β. The relationship between the two velocity vectors is

$$v_{material} = \frac{v_{measured}}{\cos\beta} \quad (12)$$

where $v_{material}$ is the velocity of the theoretical particle during detonation, $v_{measured}$ is the PDV measured velocity, and β is the angle between the two velocity vectors.

For each of the three experiments, the PDV angle is found compared to the initial location of the liner. This angle is labeled as P in Figure 39 and is used to determine the angle between the velocity vectors, β.

The measured velocity of the liner was determined using PDV data. Software called pTool was used to perform a Fourier transform on the data (Los Alamos National Laboratory & NSTec, 2008).

3.3.2 Uncertainty Analysis

The uncertainty analysis for the data gathered in this experiment is very important. This data will lead to the development of a computational model, so the data must be validated. The process to determine the error associated with each of the measured and calculated variables follows.

In order to propagate errors through the analysis, the uncertainty in the measurement of any variable r is represented in terms of the uncertainty in each independent measurement used to determine variable r as (American Institute of Aeronautics and Astronautics, 2003)

$$\varepsilon_r = \left[\sum_{i=1}^{N}\left(r_i \frac{\varepsilon_{m_i}}{m_i}\right)^2\right]^{1/2} \quad (13)$$

where ε_r refers to the associated uncertainty in the measurement r, ε_m refers to the uncertainty in the independent variable m, N refers to the total number of independent variables, and r refers to the measurement.

Calculation of material velocity

$$v_{material_i} = (\frac{v_{measured_i}}{\cos(ß_i)}) \quad (142)$$

depends on the PDV velocity measurement and determination of angle ß. The tool used to complete the PDV analysis specified values for the uncertainty associated with each measured velocity data point. Thus the uncertainty in the material velocity measurement depends on the uncertainties in PDV velocity and angle ß measurement as

$$\varepsilon_{material_i} = v_{material_i}\left[\left(\frac{\varepsilon_{ß_i}}{ß_i}\right)^2 + \left(\frac{\varepsilon_{measured_i}}{v_{measured_i}}\right)^2\right]^{1/2} \quad (15)$$

Angle ß is computed from liner angle Θ and angle P between the PDV laser and the initial liner location, so the uncertainty in angle ß is

$$\varepsilon_{ß} = ß_i\left[\left(\frac{\sigma_{\Theta_i}}{\Theta_i}\right)^2 + \left(\frac{\sigma_{P_i}}{P_i}\right)^2\right]^{1/2} \quad (16)$$

where P is the angle the PDV laser makes with the initial liner location as measured using framing camera images and Θ refers to the liner angle as measured using framing camera images. The values for the uncertainties associated with angles Θ and P were estimated using the standard deviation of measured values (Christian, 1986)

$$\sigma = \sqrt{\frac{\sum(x_i - \bar{x})^2}{(NS-1)}} \quad (17)$$

where σ refers to the standard deviation of the mean, NS refers to the total number of independent variables, x_i refers to the individual measurement, and $\bar{x}$ refers to the mean.

This method was used to propagate error for the material velocity measurements. Graphs showing the associated error bars for the material velocity are shown in Appendix G.

3.3.2.1 Sample Uncertainty Calculation

For the 76.2 µm (3 mil) case, a sample calculation will be performed on a single data point. After performing the PDV analysis, the measured velocity with associated uncertainty is

$$v_{measured} = 1143.495 \pm 1.472\ [m/s] \quad (18)$$

Next, the liner angle Θ was measured from framing camera images as discussed in the Results section. The uncertainty in the liner angle measurement was estimated to be the standard deviation. With x representing liner angle Θ measurements, and $\bar{x}$ being the average of the 16 measurements, the data analysis yields an average liner angle Θ of 9.148°.

Table 3: Liner angle Θ data with uncertainty calculations.

xi	xi- $\bar{x}$	$(xi-\bar{x})^2$	σ
8.641286	-0.50707	0.257117	0.40435
9.644285	0.495932	0.245948	
8.846507	-0.30185	0.091111	
9.80380	0.655443	0.429605	
9.206692	0.058339	0.003403	
9.139893	-0.00846	7.16E-05	
9.513332	0.364979	0.13321	
8.895289	-0.25306	0.064041	
9.266908	0.118555	0.014055	
9.050423	-0.09793	0.00959	
9.676921	0.528568	0.279384	
8.232751	-0.9156	0.838327	
9.192638	0.044285	0.001961	
8.993443	-0.15491	0.023997	
9.308373	0.16002	0.025606	

	8.961113	-0.18724	0.035059
NS	16		
Average, $\bar{x}$	9.148	$\Sigma(xi-\bar{x})^2$	2.452488

The uncertainty in liner angle was estimated to be the

$$\sigma = \sqrt{\frac{\sum(x_i - \bar{x})^2}{(NS-1)}} = \sqrt{\frac{2.452}{(16-1)}} = 0.404 \quad (19)$$

standard deviation for Θ equal to 0.404°.

The same process was completed for the PDV liner angle P that was also measured using framing camera images.

Table 4: PDV liner angle P data with uncertainty calculations.

	xi	xi- $\bar{x}$	$(xi-\bar{x})^2$	σ
	91.19349	0.366957	0.134657	0.376745
	91.30195	0.475417	0.226021	
	90.46963	-0.3569	0.12738	
	90.97102	0.144487	0.020876	
	90.47745	-0.34908	0.121859	
	90.54566	-0.28087	0.07889	
NS	6	$\Sigma(xi-\bar{x})^2$	0.709684	
Average, $\bar{x}$	90.82653333			

The average was angle P equal to 90.827° with uncertainty estimated to be the standard deviation of 0.377°

$$\sigma = \sqrt{\frac{\sum(x_i - \bar{x})^2}{(NS-1)}} = \sqrt{\frac{0.710}{(6-1)}} = 0.377 \quad (20)$$

These angles were used to calculate ß, the angle between the velocity vectors

$$ß = P - \left(90 - \left(\frac{\Theta}{2}\right)\right) = 90.827 - \left(90 - \left(\frac{9.148}{2}\right)\right) = 5.401° \quad (21)$$

with uncertainty

$$\varepsilon_ß = ß_i \left[\left(\frac{\sigma_{\Theta_i}}{\Theta_i}\right)^2 + \left(\frac{\sigma_{P_i}}{P_i}\right)^2\right]^{1/2} = (5.401°)\sqrt{\left(\frac{0.404}{9.148}\right)^2 + \left(\frac{0.377}{90.827}\right)^2} = 0.240° \quad (22)$$

Finally, the material velocity was

$$v_{material_i} = \left(\frac{v_{measured_i}}{\cos(ß_i)}\right) = \frac{1143.495\ [\frac{m}{s}]}{\cos(5.401°)} = 1148.594\ [m/s] \quad (23)$$

with uncertainty

$$\varepsilon_{material_i} = v_{material_i}\left[\left(\frac{\varepsilon_{ß_i}}{ß_i}\right)^2 + \left(\frac{\varepsilon_{measured_i}}{v_{measured_i}}\right)^2\right]^{1/2} \quad (24)$$

$$= \left(1148.594\ \left[\frac{m}{s}\right]\right)\sqrt{\left(\frac{0.240}{5.401}\right)^2 + \left(\frac{1.472}{1143.495}\right)^2} = 51.011\ [\frac{m}{s}]$$

Thus the material velocity for the data point selected for the 76.2 µm case came out to be 1148.6 ± 51.0 m/s. The uncertainty is dominated by error in measuring the angle between the velocity vectors, which is in turn dominated by error in measuring liner angle from framing camera images.

3.3.3 50.8 µm Thick Experiment

The data analysis for the liner angle consisted of measuring framing camera images, whereas the velocity of the liner was calculated based on PDV data.

3.3.3.1 Framing Camera

First, the framing camera images were viewed in sequence in order to determine that the camera timing was appropriate for the experiment. A few framing camera images are shown in Figure 41 in sequential order.

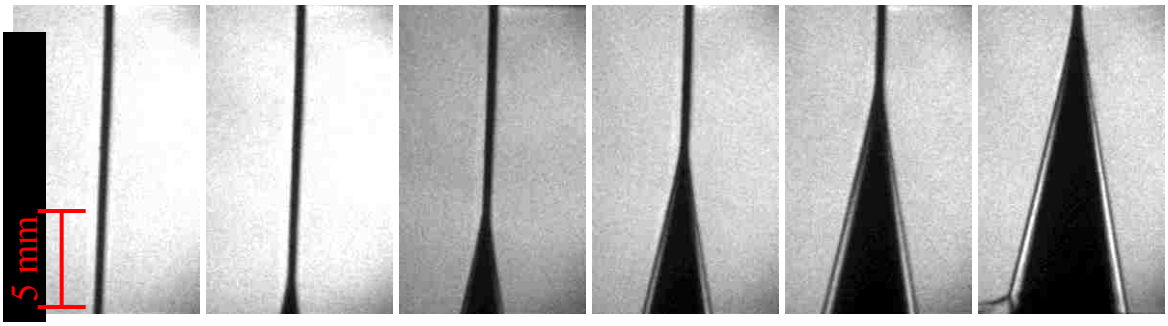

Figure 41: Cross-section view of the 50.8 µm tantalum experiment on HNAB micro-sandwich test, 5 ns exposure, 2.4 MHz (1/417 ns). Each frame has a height of about 15 mm.

The next step was to compare the experimental detonation images to the still images. It was important to compare these images to the same frame or charge-coupled device (CCD) that took the image. This eliminates any disparities between the different CCD sensors. Completing the image subtracted that was previously described in Figure 38, the measurements were able to be taken. This is shown in Figure 42 for Frame 8. Image subtraction was previously illustrated in Figure 38. Figure 42 shows a sample image for the last frame in Figure 41 for which angle measurements were taken.

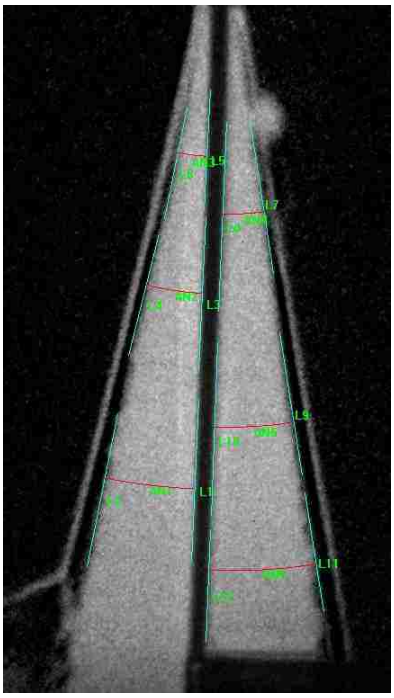

Figure 42: Angle measurements taken with Image-Pro Plus software.

The angle was determined to be 11.1° ± 0.1°. This was determined using Image-Pro Plus software and comparing the framing camera images to the initial still images. Three different framing camera images were chosen for measurements. These images showed the liner expanded at or past the point where the PDV probe measured the velocity. Six measurements were taken on each image, meaning 18 total measurements were taken. Three measurements were taken on either side of the expanding sandwich per frame in order to determine if initiation of one side of the micro-sandwich affected final results. It was determined that the difference in the angle measurements on either side of the sandwich due to initiation was negligible. These values were averaged to find the nominal liner angle. These measurement values are shown in Table 5.

Table 5: Liner angle measurements for the 50.8 µm micro-sandwich experiment. All measurements are in degrees.

Frame 8		Frame 9		Frame 10		Average	
Left	Right	Left	Right	Left	Right	Left	Right
11.1197	11.1489	11.1811	11.1156	11.2005	10.9797	11.1217	11.1221
11.1163	11.1952	11.2418	11.0021	10.8983	11.1582		
11.1055	11.0289	10.9559	11.2632	11.2761	11.2072		

As can be seen, the measurements taken on the left and right sides of the sandwich are comparable. This confirms the theory that the initiation of only half of the sandwich does not impact the sandwich detonation process. The mean value among all of the measurements came out to be 11.1° between the initial setup of the sandwich and the expanded liner during detonation.

Next, the error was calculated using the methods described earlier. The standard deviation for the 50.8 µm case was found to be 0.1°. This means that the 50.8 µm thick tantalum liner had a liner angle of 11.1° ± 0.1°.

3.3.3.2 Velocity Calculations

Prior to performing the Fourier transform on the data, the data from the oscilloscope was hard to decipher. This data is shown in Figure 43.

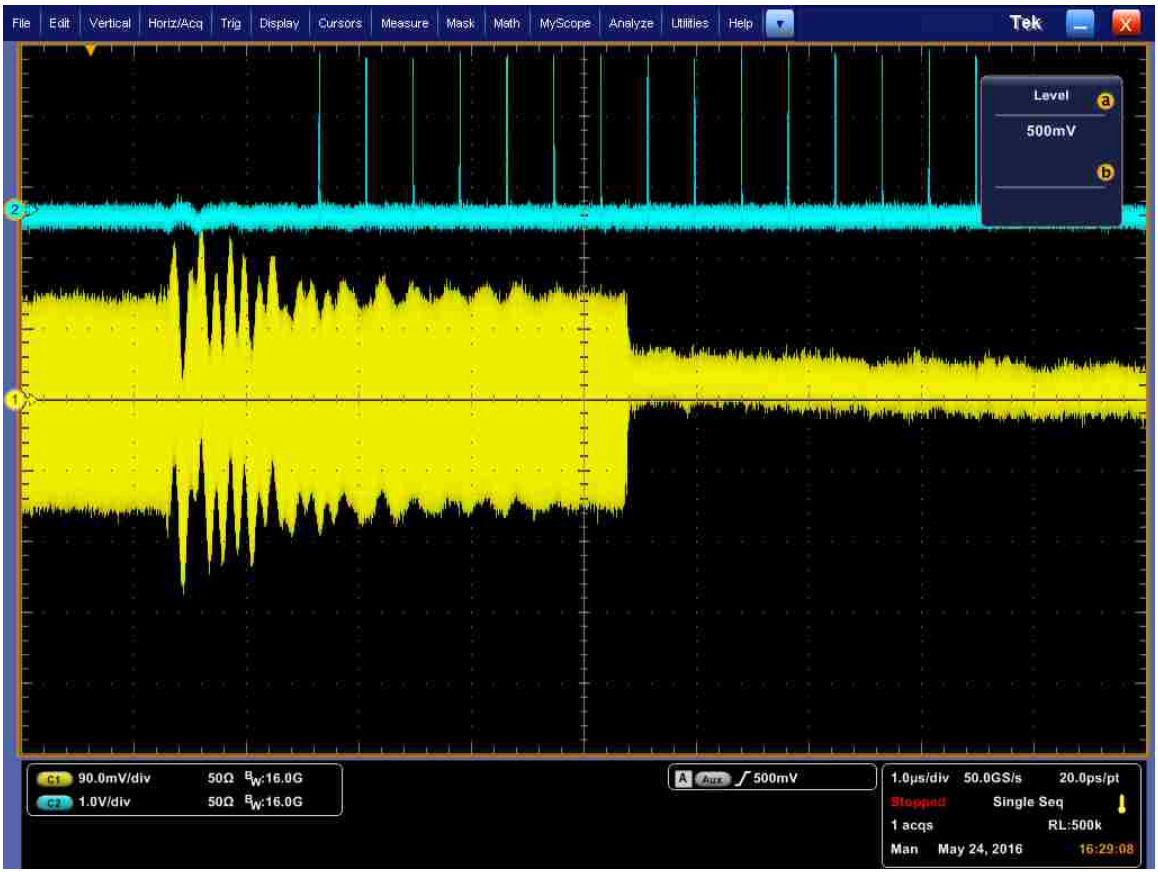

Figure 43: PDV oscilloscope data for the 50.8 µm experiment.

The timing of the PDV system was correlated to when the camera CCD channels were triggered. The CCD triggers, shown as blue pulses in Figure 43, give a way to correlate the timing of the PDV data to the framing camera images. Given that the PDV was measuring velocity information during the entire course of the experiment, it is important to only analyze the PDV data that correlates to the time where the liner moved past the probe. Based on framing camera images, Frame 8 showed the start of the expansion of the liner past the location where the PDV probe was measuring the liner velocity. Therefore, the beginning of the 8th PDV signal past the trigger pulse line is the beginning of the velocity data. This time corresponded to between 5.1 to 8 µs as measured by the oscilloscope. After performing a Fourier transform using pTool, the data was viewed graphically as shown in Figure 44.

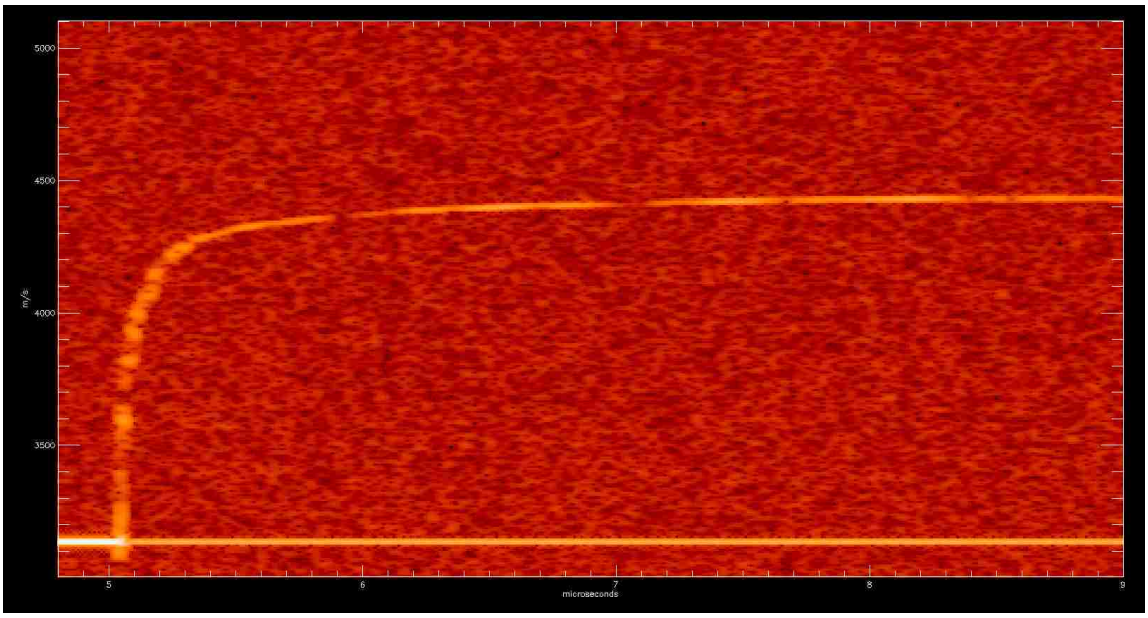

Figure 44: PDV data for the 50.8 μm experiment after performing a Fourier Transform on the data. Graphical representation of the measured velocity. Looking at time corresponding to where the liner expanded past the PDV probe. The x-axis is time in μs, and the y-axis shows the velocity of the liner in m/s.

The data was analyzed using pTool to yield a relationship between time and measured velocity. Subtracting out the baseline value that was an artifact of the upshifted system, the measured values were established. Next, calculations were performed on the data to determine the material velocity as a function of time and the data was graphed to describe the behavior. A graphical representation of the material velocity as a function of time is presented in Figure 45.

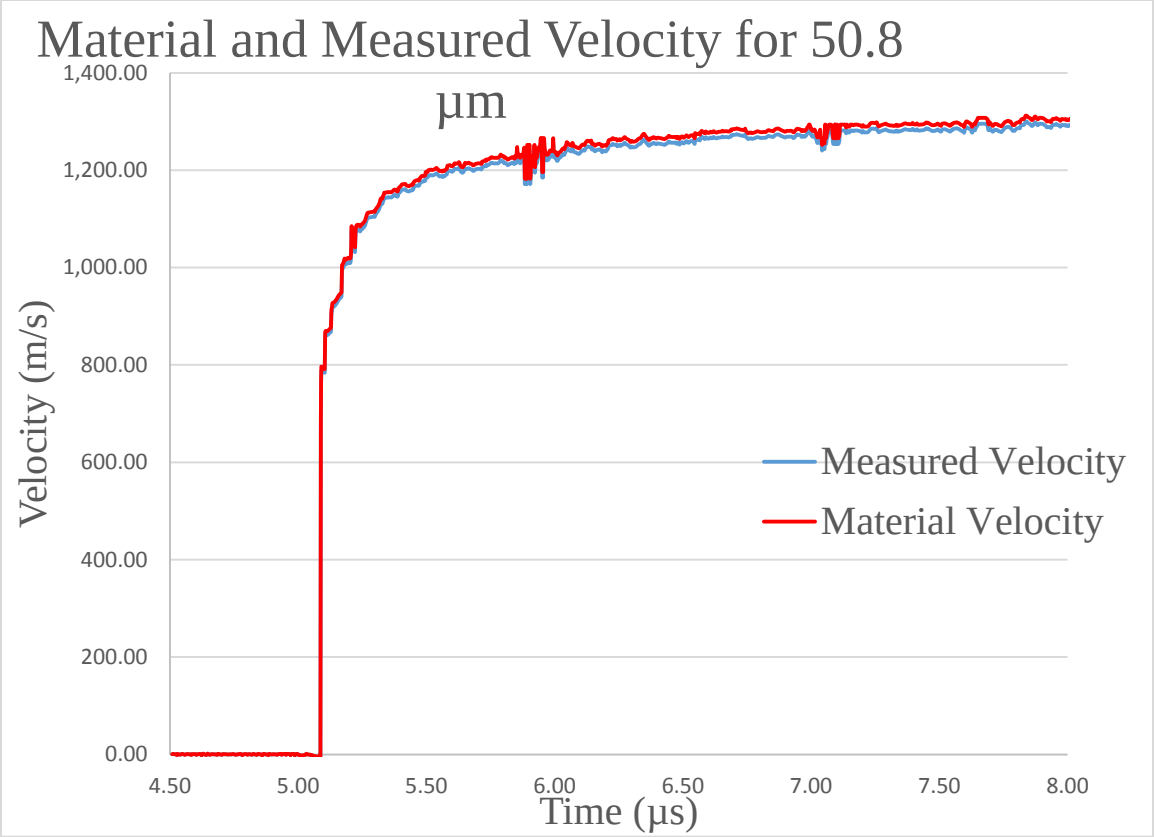

Figure 45: Graph showing the measured and material velocity data for the 101.6 µm thick experiment.

It was found that the maximum value of the PDV measured liner velocity is 1303.0 ± 3.9 m/s. Performing the calculation, the maximum material velocity was found to be 1315.2 ± 21.4 m/s.

3.3.4 76.2 µm Thick Experiment

The data analysis for the liner angle consisted of measuring framing camera images, whereas the velocity of the liner was calculated based on PDV data.

3.3.4.1 Framing Camera

First, the framing camera images were viewed in sequence in order to determine that the camera timing was appropriate for the experiment. A few framing camera images are shown in Figure 46 in sequential order.

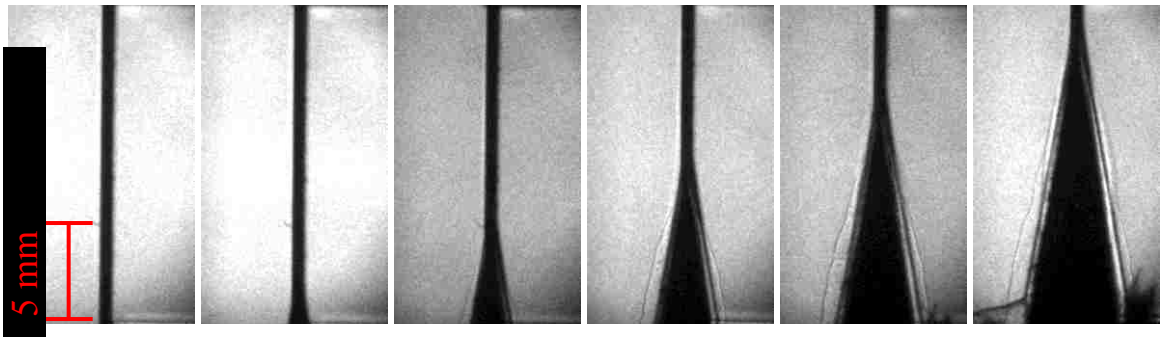

Figure 46: Cross-section view of the 76.2 µm tantalum experiment on HNAB micro-sandwich test, 5 ns exposure, 2.4 MHz (1/417 ns). Each frame has a height of about 15 mm.

The next step was to compare the experimental detonation images to the still images. It was important to compare these images to the same frame or charge-coupled device (CCD) that took the image. This eliminates any disparities between the different CCD sensors. Completing the image subtracted that was previously described in Figure 38, the measurements were able to be taken. This is shown in Figure 47.

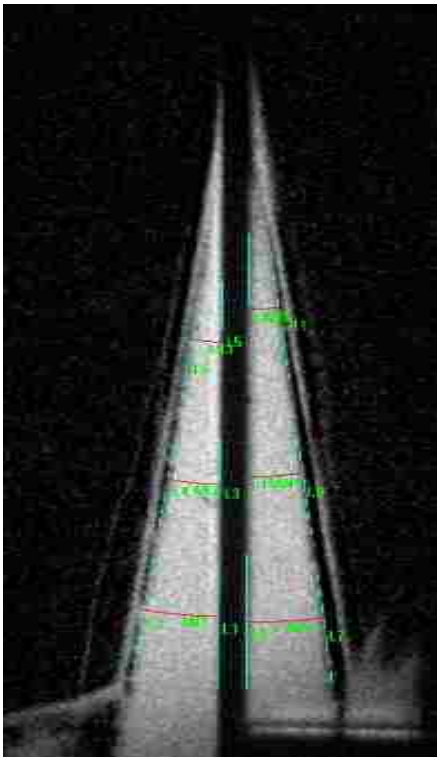

Figure 47: Angle measurements taken with Image-Pro Plus software.

The angle was determined to be 9.1° ± 0.1°. This was again determined using Image-Pro Plus software and comparing the framing camera images to the initial still images. Three different framing camera images were chosen for measurements. These images showed the liner expanded at or past the point where the PDV probe measured the velocity. Six measurements were taken on each image, meaning 18 total measurements were taken. Three measurements were taken on either side of the expanding sandwich per frame in order to determine if initiation of one side of the micro-sandwich affected final results. It was determined that the difference in the angle measurements on either side of the sandwich due to initiation was negligible. These values were averaged together to find the nominal liner angle. These measurement values are shown in Table 6.

Table 6: Liner angle measurements for the 76.2 μm micro-sandwich experiment. All measurements are in units of degree.

Frame 8		Frame 9		Frame 10		Average	
Left	Right	Left	Right	Left	Right	Left	Right
8.9905	9.0860	9.0267	8.8953	9.0769	8.9934	9.0709	9.0710
9.1602	9.0554	9.1329	9.2669	8.9328	9.2584		
9.0620	9.0713	9.0533	9.0504	9.2026	8.9622		

Once again, it can be observed that the difference in angle measurements between the left and right sides of the sandwich are negligible. The mean value among all of the measurements came out to be 9.1° between the initial setup of the sandwich and the expanded liner during detonation. Next, the error was calculated the same way as previous. The resulting standard deviation came out to be 0.1°. This means that the 76.2 μm thick tantalum liner had a liner angle of 9.1° ± 0.1°.

3.3.4.2 Velocity Calculations

The velocity of the liner was determined using PDV data. Once again, the data prior to performing the Fourier transform on the data, is shown in Figure 48.

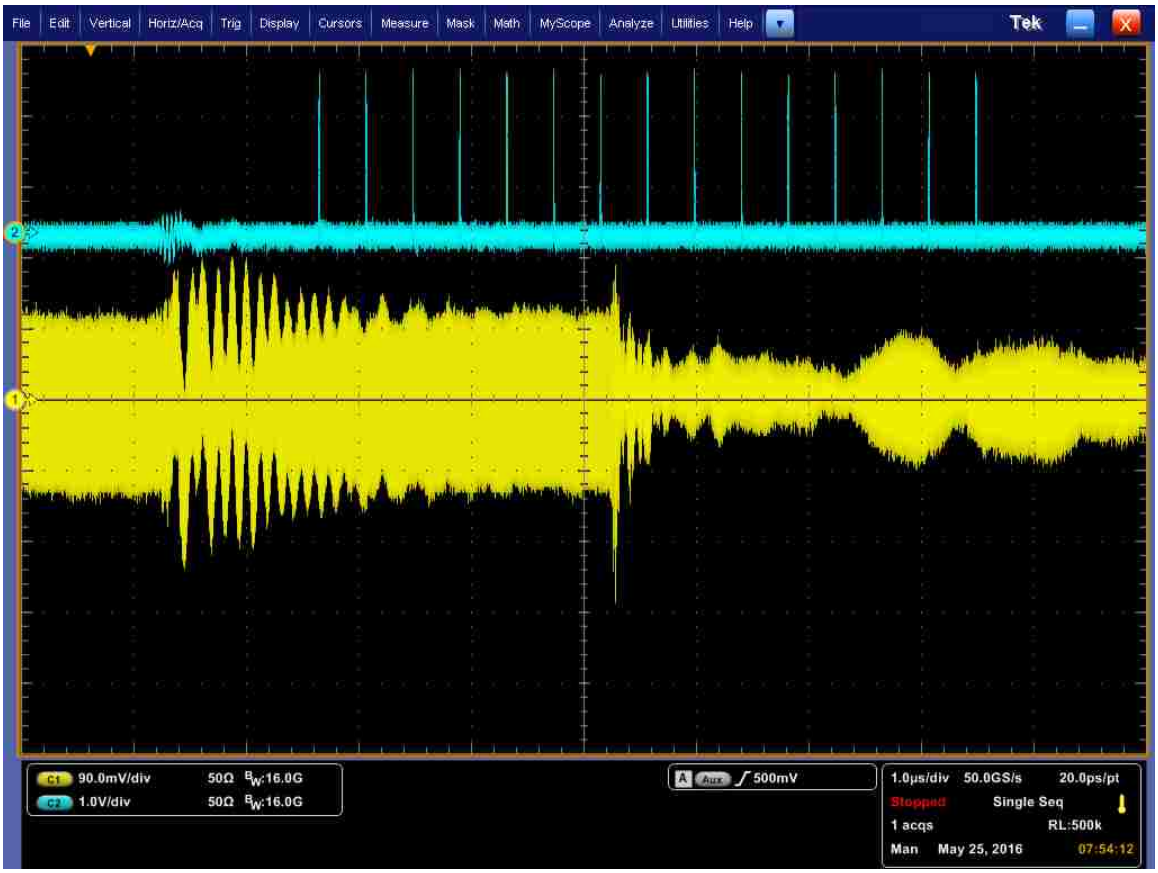

Figure 48: PDV oscilloscope data for the 76.2 µm experiment.

The timing of the PDV system was correlated to when the camera CCD channels were triggered. The CCD triggers, shown as blue pulses in Figure 48, give a way to correlate the timing of the PDV data to the framing camera images. Given that the PDV was measuring velocity information during the entire course of the experiment, it is important to only analyze the PDV data that correlates to the time where the liner moved past the probe. Based on framing camera images, Frame 8 showed the start of the expansion of the liner past the location where the PDV probe was measuring the liner velocity. Therefore, the beginning of the 8th PDV signal past the trigger pulse line is the start of the velocity data. This time corresponded to between 4.9 to 8 µs as measured by the oscilloscope. After performing a Fourier transform using pTool, the data was viewed graphically as shown in Figure 49.

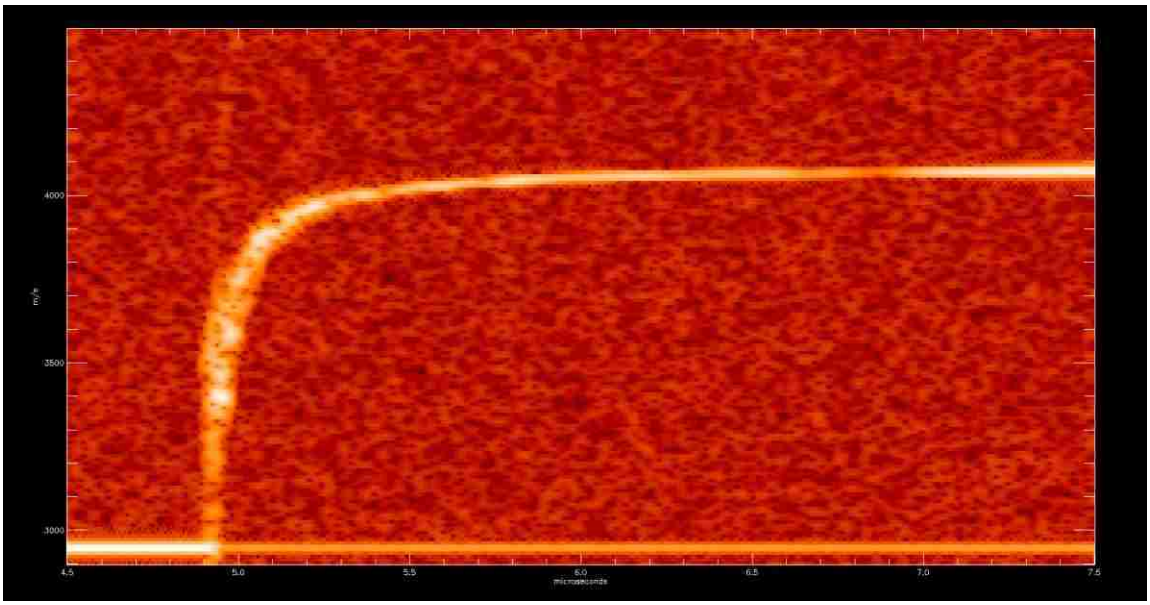

Figure 49: PDV data for the 76.2 μm experiment after performing a Fourier Transform on the data. Graphical representation of the measured velocity. Looking at time corresponding to where the liner expanded past the PDV probe. The x-axis is time in μs, and the y-axis shows the velocity of the liner in m/s.

The data was again analyzed using pTool. The measured data was again corrected for the baseline artifact by subtracting the baseline from the data. The relationship between time and measured velocity was established for the 76.2 μm case as well as the material velocity as a function of time. A graphical representation of the data for the material velocity as a function of time is shown in Figure 50.

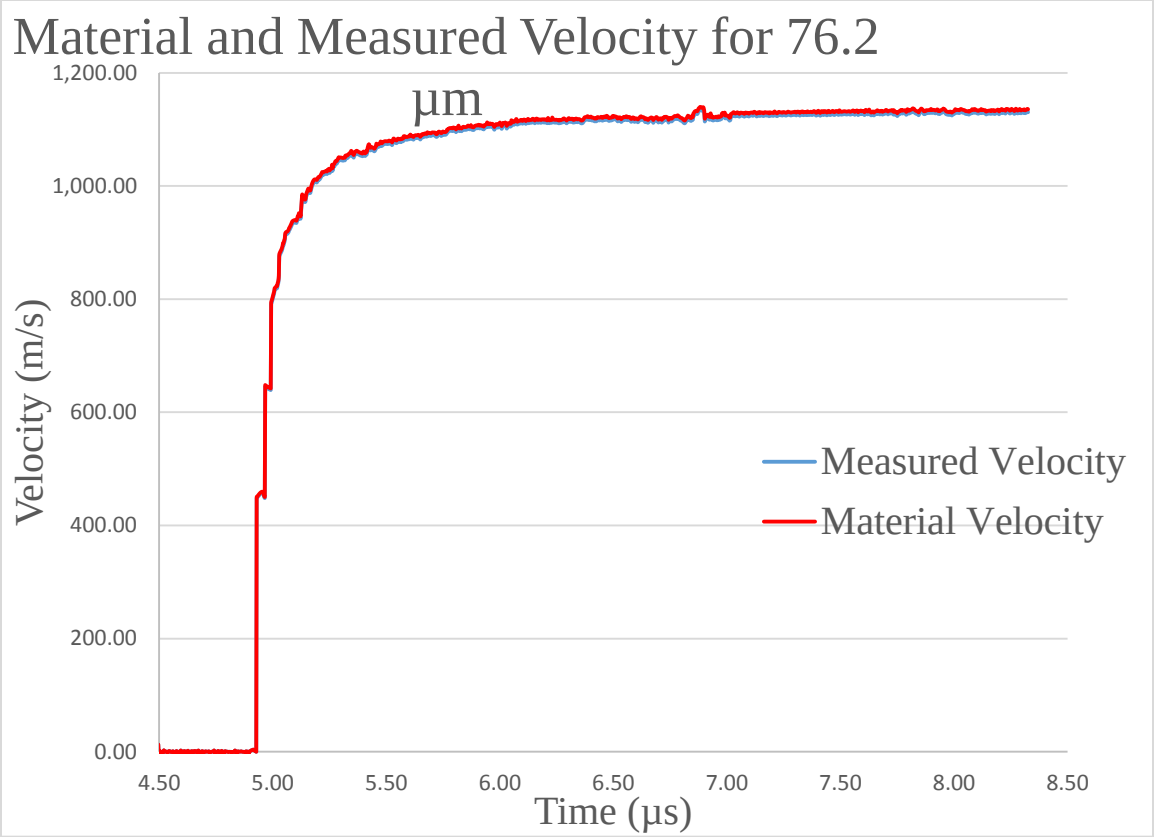

Figure 50: Graph showing the measured and material velocity data for the 101.6 µm thick experiment.

It was found that the maximum value of the PDV measured liner velocity is 1143.5 ± 1.5 m/s. Performing the calculation, the maximum material velocity was found to be 1148.6 ± 51.6 m/s.

3.3.5 101.6 µm Thick Experiment

3.3.5.1 Framing Camera

First, the framing camera images were viewed in sequence in order to determine that the camera timing was appropriate for the experiment. A few framing camera images are shown in Figure 51 in sequential order.

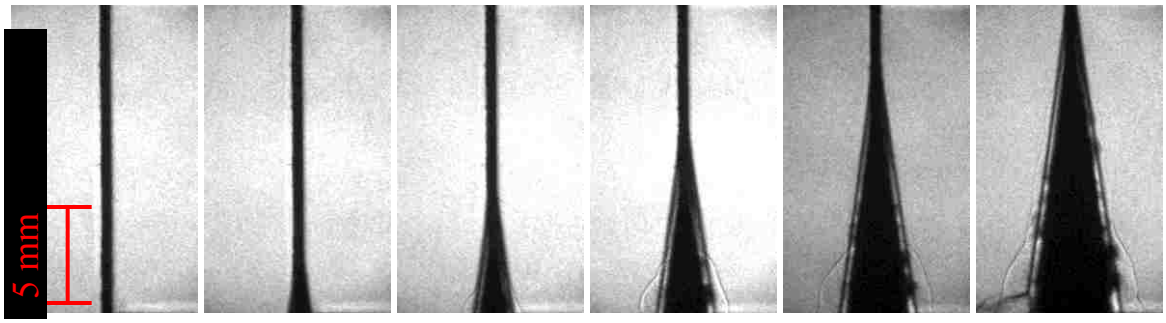

Figure 51: Camera-view of the 101.6 µm tantalum experiment on HNAB micro-sandwich test, 5 ns exposure, 2.4 MHz (1/417 ns). Each frame has a height of about 15 mm.

The next step was to compare the experimental detonation images to the still images. It was important to compare these images to the same frame or charge-coupled device (CCD) that took the image. This eliminates any disparities between the different CCD sensors. Completing the image subtracted that was previously described in Figure 38, the measurements were able to be taken. This is shown in Figure 52.

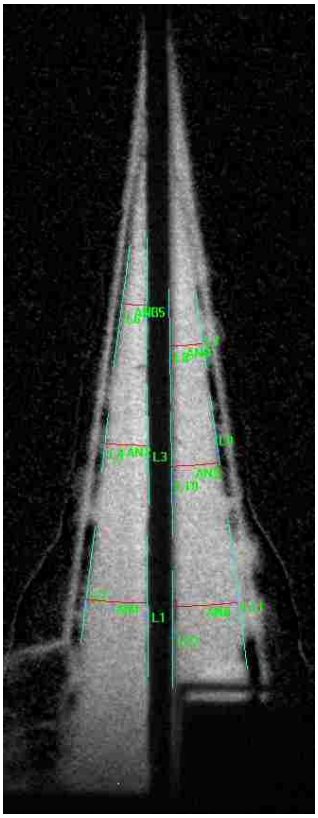

Figure 52: Angle measurements taken with Image-Pro Plus software.

The angle was determined to be 7.3° ± 0.1°. This was again determined using Image-Pro Plus software and comparing the framing camera images to the initial still images. Three different framing camera images were chosen for measurements. These images showed the liner expanded at or past the point where the PDV probe measured the velocity. Six measurements were taken on each image, meaning 18 total measurements were taken. Three measurements were taken on either side of the expanding sandwich per frame in order to determine if initiation of one side of the micro-sandwich affected final results. It was determined that the difference in the angle measurements on either side of the sandwich due to initiation was negligible. These values were averaged together to find the nominal liner angle. These measurement values are shown in Table 7.

Table 7: Liner angle measurements for the 101.6 μm micro-sandwich experiment.

Frame 6		Frame 7		Frame 8		Average	
Left	Right	Left	Right	Left	Right	Left	Right
7.6441	7.2343	7.3349	7.3132	7.2214	7.2236	7.2726	7.2713
6.9272	7.3195	7.2568	7.2157	7.2890	7.2820		
7.2243	7.2206	7.2702	7.3058	7.2855	7.3274		

Observing the data, it is obvious from the average values of the measurements taken on both the left and right sides of the sandwich that the liner angle is virtually the same on both. This means that the initiation of only half of the sandwich did not impact the results. The mean value among all of the measurements came out to be 7.3° between the initial setup of the sandwich and the expanded liner during detonation. Next, the error was calculated the same way as previous. The resulting standard deviation came out to

be 0.1°. This means that the 101.6 µm thick tantalum liner had a liner angle of 7.3° ± 0.1°.

3.3.5.2 Velocity Calculations

The velocity of the liner was determined using PDV data pTool was used to perform a Fourier transform on the data. The data that was gathered from the experiment of the 101.6 µm case is shown in Figure 53.

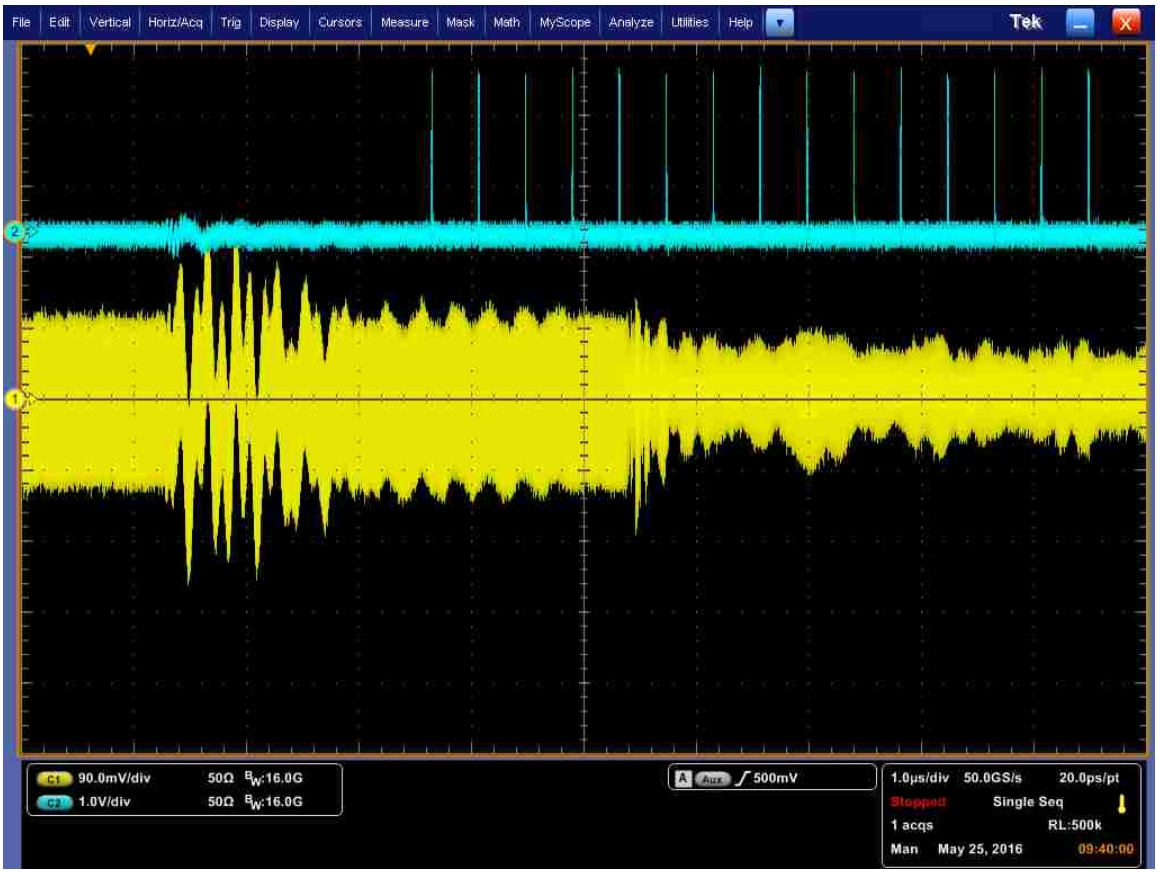

Figure 53: PDV oscilloscope data for the 101.6 µm experiment.

The timing of the PDV system was correlated to when the camera CCD channels were triggered. The CCD triggers, shown as blue pulses in Figure 53, give a way to correlate the timing of the PDV data to the framing camera images. Given that the PDV was measuring velocity information during the entire course of the experiment, it is important

to only analyze the PDV data that correlates to the time where the liner moved past the probe. Based on framing camera images, Frame 6 showed the start of the expansion of the liner past the location where the PDV probe was measuring the liner velocity. Therefore, the start of the 6th PDV signal past the trigger pulse line is the start of the velocity data. This time corresponded to between 4.9 to 8 µs as measured by the oscilloscope. After performing a Fourier transform using pTool, the data was viewed graphically as shown in Figure 54.

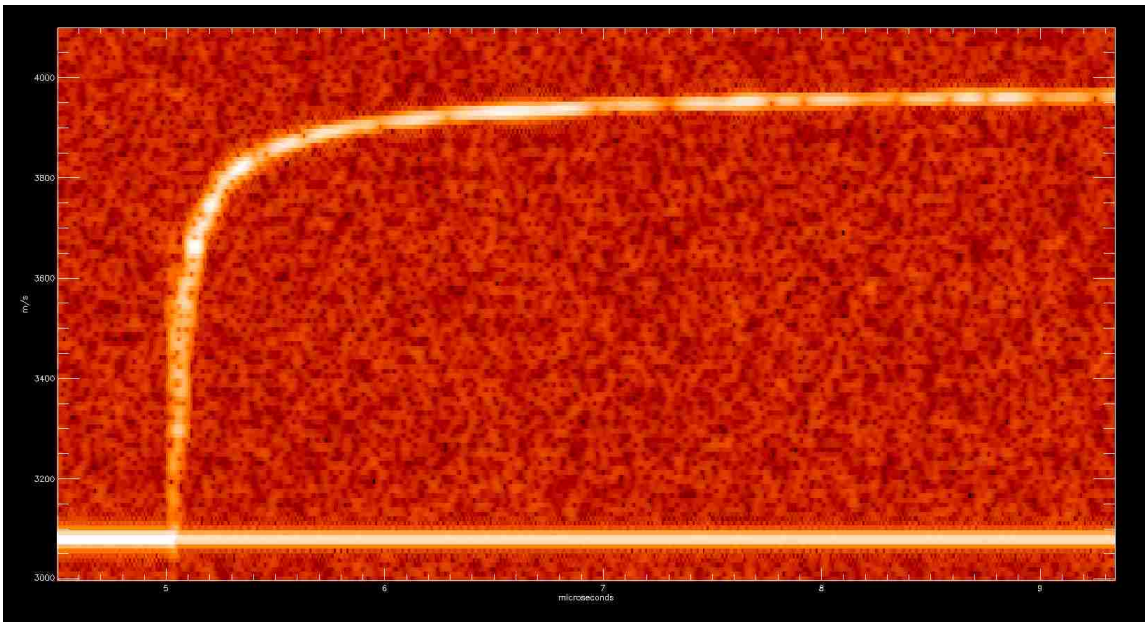

Figure 54: PDV data for the 101.6 µm experiment after performing a Fourier Transform on the data. Graphical representation of the measured velocity. Looking at time corresponding to where the liner expanded past the PDV probe. The x-axis is time in µs, and the y-axis shows the velocity of the liner in m/s.

pTool was again used to yield a relationship between time and measured velocity, allowing the calculations to be completed to determine the material velocity as a function of time. A graph describes the behavior of the material velocity as a function of time. A graphical representation of the data for the material velocity as a function of time is shown in Figure 55.

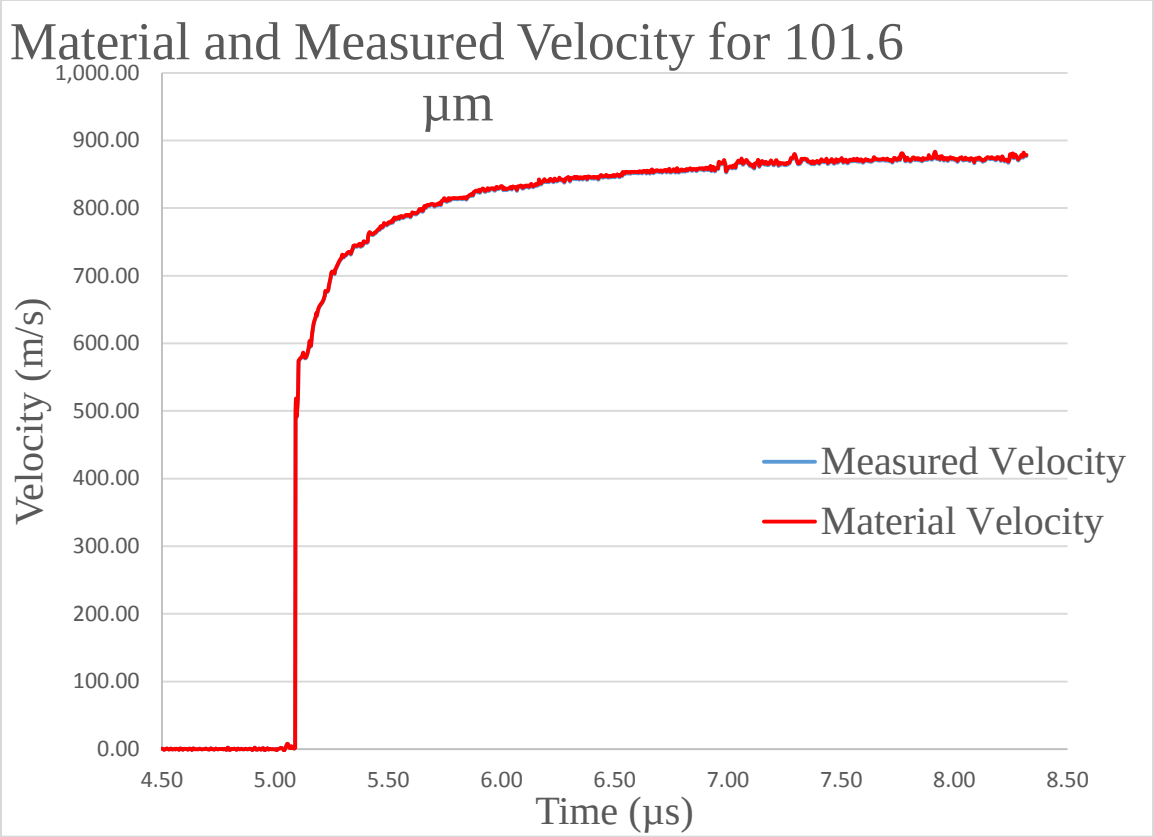

Figure 55: Graph showing the measured and material velocity data for the 101.6 µm thick experiment.

The maximum value of the PDV measured liner velocity is 886.8 ± 4.8 m/s. Performing the calculation, the maximum material velocity was found to be 888.5 ± 4.8 m/s.

3.3.6 Velocity Results

The micro-sandwich experiment was completed on three different thicknesses of tantalum liners, 50.8 µm, 76.2 µm, and 101.6 µm.

The full Gurney equation yields information for the Gurney characteristic velocity, V, for the case of the symmetrical slab geometry (Cooper, 1996)

$$\frac{V}{\sqrt{2E}} = \left(2\frac{M}{C} + \frac{1}{3}\right)^{-1/2} \qquad (25)$$

where $\sqrt{2E}$ is the Gurney constant that is unique to each explosive, M is the mass of the liner, C is that charge of the liner, and V is the velocity of the liner.

In order to calculate the Gurney constant, an approximation must be used. The approximation correlates the Gurney constant to the detonation velocity and pressure of the explosive as well as the explosive density (Cooper, 1996). The detonation velocity for HNAB is 7.42 km/s (Tappan, et al., 2014), meaning the Gurney constant is 2.50 km/s.

$$\sqrt{2E} = \frac{D}{2.97} = \frac{7.42\ \left[\frac{km}{s}\right]}{2.97} = 2.498\ \left[\frac{km}{s}\right] \qquad (26)$$

where D is the detonation velocity. Knowing this, the Gurney characteristic velocity can be calculated for the three different cases. For the thinnest case, 50.8 μm thick, the mass of the tantalum is found to be 253.8 mg and for all cases, the HNAB mass is found to be 62.46 mg.

$$\boldsymbol{V = \sqrt{2E}\left(2\frac{M}{C}+\frac{1}{3}\right)^{-1/2} = 2.50\ \left[\frac{km}{s}\right]\left(2\frac{253.8}{62.46}+\frac{1}{3}\right)^{-1/2} = 858.9\ \left[\frac{m}{s}\right]} \qquad (27)$$

This value is significantly different from the experimental results for the liner velocity. A table showing the comparison of the material and Gurney velocities is presented in Table 8.

Table 8: Results of the three experiments for the maximum material velocity compared to the Gurney characteristic velocity.

	50.8 µm	76.2 µm	101.6 µm
Gurney Velocity [m/s]	858.9 ± 42.3	706.0 ± 47.2	613.4 ± 7.8
Maximum Material Velocity [m/s]	1315.20 ± 21.43	1148.60 ± 51.63	888.50 ± 4.78

The significant differences between the material velocity and the Gurney characteristic velocity may show that the empirically-derived Gurney method breaks down for the micro-sandwich. It might not apply for cases with thin metal liners or high density metal. In order to fully test the Gurney method for the micro-sandwich, more experimental data is needed.

There is an obvious trend among the data that as the liner thickness increases, the liner angle and material velocities decrease. This result is expected because greater thicknesses of liner material would have lower velocities when undergoing the same amount of pressure and force. None of the three cases violated the Gurney approximation

3.3.7 Framing Camera Velocity calculations

As a method to check the PDV material velocity calculations, the framing camera images were used. First, the framing camera images were calibrated in order to get measurement data. Then measurements were taken among different frames and velocity data was calculated.

Calibration was completed using a Ronchi Rule image that was taken with the framing camera prior to the experiment. The Ronchi rule shows light and dark lines interspersed

throughout the length of the camera field of view. For this experiment, a Ronchi rule of 50 line pairs per inch was used, meaning there are 100 lines per inch. These images were taken before the experiment took place and were used to calibrate the dynamic images from the experiment. An image of the Ronchi rule with measurements is shown in Figure 56.

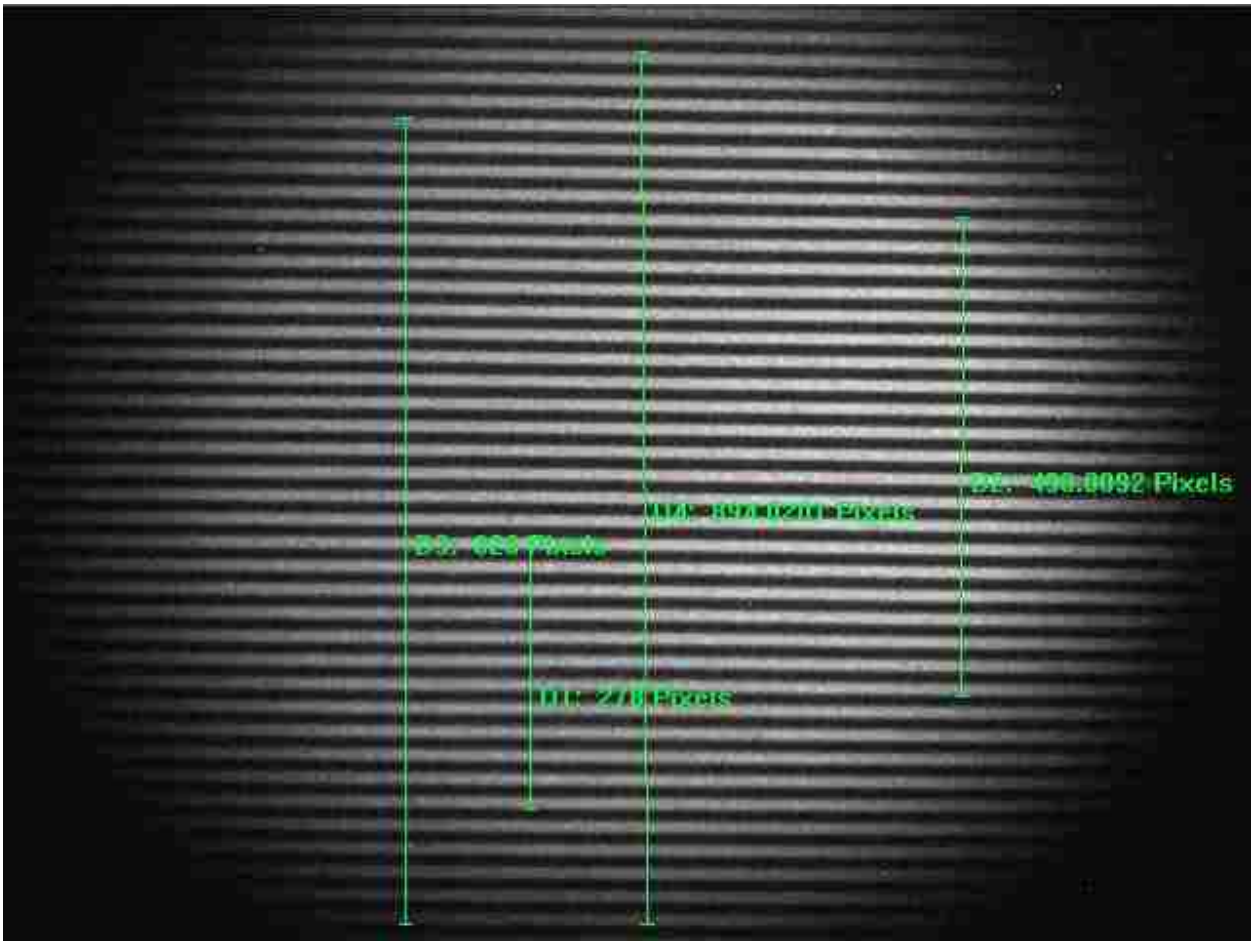

Figure 56 - Ronchi rule calibration image used to calibrate the framing camera images.

Comparing a number of lines to the amount of corresponding pixels with the knowledge that there are 50 line pairs per inch for this particular case, length measurements are able to be taken from framing camera images. The relationship between pixels in each image and length is

$$100\frac{[lines]}{[inch]} * \frac{x\,[pixels]}{y\,[lines]} * \frac{1\,[inch]}{25400\,[\mu m]} = \frac{z\,[pixels]}{[\mu m]} \quad (28)$$

where x refers to the number of pixels that was measured on a line and y is the corresponding number of lines; z refers to the resulting conversion factor between the number of pixels and a length in µm.

For this experiment, it was determined that there are 0.042 pixels per µm. Using this, length measurements are able to be taken from framing camera images. Comparing the length of expansion between two different dynamic frames at the same point and dividing those lengths by 417 ns (which is the time between frames), we can determine the measured velocity. Completing the data analysis in the same way as the PDV measurement, we can determine the material velocity. The results came out to be fairly similar to the PDV results. This is shown in Table 9.

Table 9: Comparison of Framing camera and PDV material velocity calculations.

	50.8 µm		**76.2 µm**		**101.6 µm**	
Framing Camera Material Velocity	1334.1	m/s	1173.7	m/s	916.8	m/s
PDV Material Velocity	1315.2	m/s	1148.6	m/s	888.5	m/s
Difference	18.9	m/s	25.1	m/s	28.3	m/s

There is a slight difference between the two methods of calculating the material velocity, but overall they are fairly similar. The same trend is shown, that as the thickness increases, the material velocity decreases. The material velocity that was calculated from

the PDV data is considered to be more accurate than the framing camera data which has more sources of potential error. These sources of error include the fact that the framing camera did not continuously take data unlike the PDV as well as the fact that the framing camera calibration process introduced error. The results show only slight differences between the two diagnostics, which are within 30 m/s of each other. This means that the framing camera measurements confirms the PDV material velocity measurements.

3.3.8 Transit time

The transit time for each case was calculated. The transit time refers to the amount of time for the shock to travel through the tantalum liner. We expected the results to show a proportional relationship between the ratio of the transit times to the ratio of the liner thicknesses. For example, we expected the ratio of the transit times of the 76.2 µm case to that for the 50.8 µm case to be approximately 1.5. A graphical representation of the 50.8 µm case with the transit time "steps" marked is shown in Figure 57.

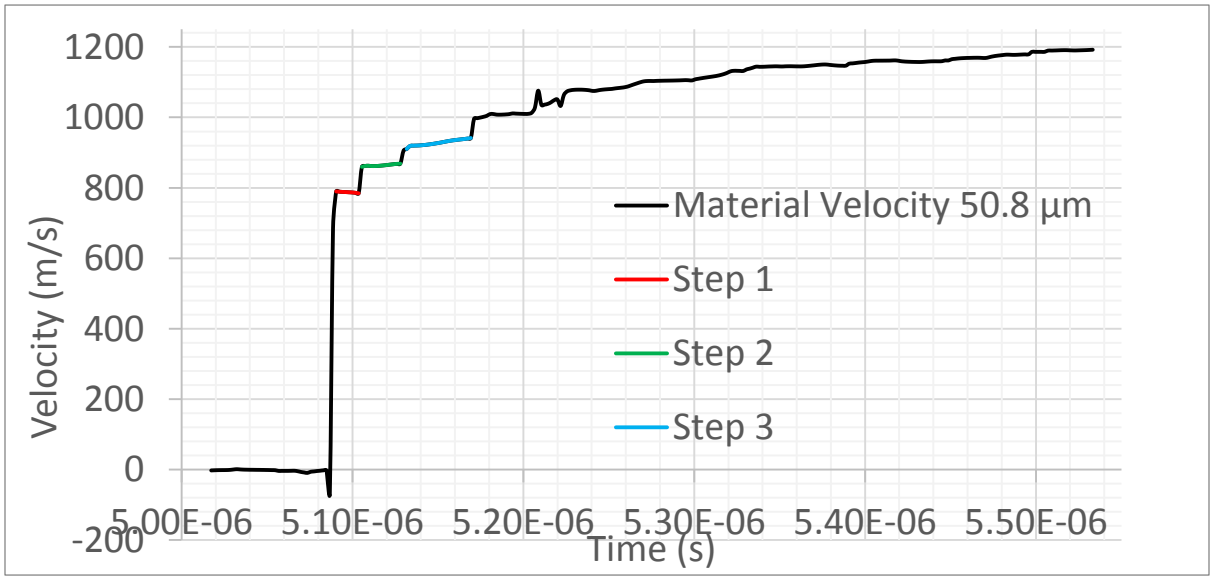

Figure 57 - Graph showing the material velocity with transit time "steps" for the 50.8 µm case.

The data presented in Table 10 showed an unexpected result for the case of the first "transit step." Transit times in step 1 do not increase linearly with liner thicknesses as expected. This may be due to an artifact of the PDV, and will require more experimental data to test. Results for the second "transit step" showed behavior that was more nearly what was expected.

Table 10 - Transit time data for each of the three tantalum liner thicknesses.

	50.8 µm	76.2 µm	101.6 µm
Step	t (µs)	t (µs)	t (µs)
1	1.313	3.564	7.579
2	2.251	3.377	5.684

The ratio of transit times for the 76.2 µm case to that for the 50.8 µm case was 1.5, as expected. The ratio of transit times for the 76.2 µm case to that for the 101.6 µm case was about 1.68, which is slightly higher than the expected value of 1.33. Finally, the ratio of transit times for the 101.6 µm case to that for the 50.8 µm case was 2.53, which is higher than the expected value of 2. Additional experimental data would be necessary in order to fully investigate the differences between expected and actual results.

4 Conclusion

Overall, the sandwich test is a very useful experiment for determining data that leads to development of products equation of state (EOS) for an explosive. The sandwich test consists of slab geometry with a liner, generally metal, on either side of the explosive that is being tested. The sandwich test is similar to the cylinder expansion test, which consists of a metal cylinder filled with explosives.

For specific cases, the sandwich test had several advantages over the cylinder test, including thinner liner materials and more versatile temperature ranges. This especially holds true for explosives that undergo physical vapor deposition (PVD) like hexanitroazobenzene (HNAB). Vapor-deposited HNAB is a useful model for studying detonation behavior at small scales because it has a uniform microstructure with low surface roughness. These characteristics make HNAB ideal for a small-scale version of a sandwich test, the micro-sandwich test.

Tantalum was chosen as the liner material for this experiment because it is stiff, has high density, and has higher values of acoustic impedance that provide better confinement of the explosive. Additionally, the tantalum foils were relatively easy to procure and cut into the 10 mm × 30 mm substrate.

The course of the experiment yielded some interesting results. Based on the fact that HNAB crystallizes into two different crystallographic polymorphs, this experimental process had several setbacks with the PVD process. Initial tests found that the HNAB did not adhere well to the manufacturer provided tantalum liner. This would have been catastrophic to the experiment as any delamination would cause gaps which result in

jetting during detonation and invalidate the results. Also, the undesirable, yellow unknown phase of HNAB was promoted on the surface of the tantalum liner in much higher percentages than were preferred. The tantalum was flattened annealed in order to prevent any further stresses being introduced to the HNAB film. Further investigations found that Parylene C was the key ingredient in the process to promote adhesion as well as the desired HNAB-II phase of crystallized HNAB. The Parylene C was initially investigated as a method to prevent cracking and lifting of the HNAB from the substrate, but was found to promote the crystallization of HNAB-II at much faster rates than substrates that did not get Parylene C coated. Ultimately, the flattened annealed, Parylene C coated substrates were found to be desirable for the micro-sandwich test.

The sandwich assembly proved relatively problem-free compared to the PVD process. Two identical substrates were bonded together using a very low viscosity adhesive. This very low viscosity adhesive was chosen because it did not visually react with the HNAB and it provided a thin bond thickness. A thin bond was desired in order to keep the micro-sandwich as symmetrical as possible, while still eliminating any air gaps which could allow hot gas jetting and invalidate the results. One of the assembly issues that occurred was the removal of the Parylene C from the back of each substrate liner. This was completed in order to allow for greater return signal for the photonic Doppler velocimetry (PDV) probe during the experiment. The Parylene C introduced several potential error sources, particularly the possibility of the Parylene C separating from the tantalum liner surface during detonation as well as the Parylene C causing extraneous reflections and giving low return to the PDV probe. This removal process did not hinder the experiment and was completed quickly allowing for the assembly process to continue.

Once the micro-sandwich was assembled into the pre-designed fixture, which allowed full visual access of the cameras to observe the side of the sandwich during detonation and the PDV access to the back of the tantalum surface, the pentaerythritol tetranitrate (PETN) initiation structure was added and the experiment took place.

An initial experiment was completed in order to test the ability of the PETN to initiate the HNAB through the Parylene C coating as well as to test the timing of the cameras and other diagnostic equipment. The initial experiment used less desirable substrates that were not annealed and had much cracking. The Parylene C prevented the cracking from causing any interruptions in the detonation propagation as well as prevented any air gaps from causing jetting. The initial experiment yielded successful timing data for the diagnostics.

Next, the micro-sandwich experiment was completed on three different thicknesses of tantalum liners, 50.8 μm, 76.2 μm, and 101.6 μm. These experiments resulted in useful data. The data analysis of the three different thickness of tantalum liners yielded the trend that as the liner thickness increased, the liner angle and material velocities decreased. This result was expected because greater thicknesses of liner material would have lower velocities when undergoing the same amount of pressure and force.

The next step for this experimental process is to provide the material velocities as a function of time to a computational modeler who will develop the products EOS for HNAB. The modeling process falls outside of the scope of this thesis.

5 References

American Institute of Aeronautics and Astronautics. (2003). Assessing Experimental Uncertainty *Guide: Assessing Experimental Uncertainty - Supplement to AIAA S-071A-1999*. Reston, VA: American Institute of Aeronautics and Astronautics, Inc.

Ao, T., & Dolan, D. H. (2010). SIRHEN: A Data Reduction Program for Photonic Doppler Velocimetry Measurements, Sandia National Laboratories, Technical Report SAND2010-3628.

Aslam, T. D., Bdzil, J. B., & Hill, L. G. (2004). *Analysis of the LANL Detonation-Confinement Test.* in Proceedings of the Conference of the American Physical Society Topical Group on Shock Compression of Condensed Matter, Portland, OR. pp. 831-834.

Briggs, M. E., Hull, L., & Shinas, M. (2009). *Fundamental Experiments in Velocimetry*. in Proceedings of the Annual Meeting of the American Physical Society Division on Shock Compression of Condensed Matter, Nashville, TN. pp. 577.

Bruker. (2016). DektakXT Stylus Profiler. 2016, from https://www.bruker.com/products/surface-analysis/stylus-profilometers/dektak-xt/overview.html

Christian, G. D. (1986). Analytical Chemistry (Fourth ed.), pp. 70-96, New York: John Wiley and Sons.

Cooper, P. W. (1996). Section IV: Detonation *Explosives Engineering*, pp. 251-313, New York: Wiley-VCH.

Curtiss-Wright. (2016). What is the Parylene Coating process? http://www.parylene.co.uk/about-parylene/faqs/

Dobratz, B. M., & Crawford, P. C. (1985). LLNL Explosives Handbook – Properties of Chemical Explosives and Explosive Simulants, 'HNAB', Lawrence Livermore National Laboratory, Technical Report UCRL-52997-Chg.2, pp. 8-21.

Fried, L. E. (1994). CHEETAH 1.0 users manual, Lawrence Livermore National Laboratory, Technical Report UCRL-MA-117541.

Graeber, E. J., & Morosin, B. (1974). The Crystal Structures of 2,2',4,4',6,6'-hexanitroazobenzene (HNAB), Forms I and II. *Acta Crystallographica Section B, 30*(2), 310-317.

Hamamatsu. (2015). Guide to Streak Cameras. 2015, from http://www.hamamatsu.com/resources/pdf/sys/SHSS0006E_STREAK.pdf

Held, M. (1983). TNT - Equivalent. *Propellants, Explosives, Pyrotechnics, 8*(5), 158-167.

Hertel Jr., E. S., Bell, R. L., Elrick, M. G., Farnsworth, A. V., Kerley, G. I., McClaun, J. M., Petney, S. V., Silling, S. A., Taylor, P. A., & Yarrington, L. (1992). CTH: A Software Family for Multi-Dimensional Shock Physics Analysis, Sandia National Laboratories, Technical Report SAND92-2089C.

Hill, L. G. (2002). *Development of the LANL Sandwich Test*. in Proceedings of the Conference of the American Physical Society Topical Group on Shock Compression of Condensed Matter, Atlanta, GA. pp. 149-152.

Jackson, S. I., & Short, M. (2015). Scaling of Detonation Velocity in Cylinder and Slab Geometries for Ideal, Insensitive and Non-ideal Explosives. *Journal of Fluid Mechanics, 773*, 224-266.

Jensen, B. J., Holtkamp, D. B., Rigg, P. A., & Dolan, D. H. (2009). Accuracy Limits and Window Corrections for Photon Doppler Velocimetry. *Journal of Applied Physics, 101*(1), 013523.

Jones, H., & Miller, A. R. (1948). The Detonation of Solid Explosives: The Equilibrium Conditions in the Detonation Wave-Front and the Adiabatic Expansion of the Products of Detonation. *Proceedings of the Royal Society of London A: Mathematical, Physical and Engineering Sciences, 194*(1039), 480-507.

Kennedy, J. E. (2003). The Gurney Model of Explosive Output for Driving Metal. In J. A. Zukas & W. P. Walters (Eds.), Explosive Effects and Applications, pp. 221-257. High-Pressure Shock Compression of Condensed Matter: Springer.

Knepper, R. (2014). *Physical Vapor Deposition of HNAB.* Gordon Research Conference, Newry, ME.

Knepper, R., Browning, K., Wixom, R. R., Tappan, A. S., Rodriguez, M. A., & Alam, M. K. (2012). Microstructure Evolution During Crystallization of Vapor-Deposited Hexanitroazobenzene Films. *Propellants, Explosives, Pyrotechnics, 37*, 459 – 467.

Knepper, R., Marquez, M. P., & Tappan, A. S. (2014). *Effects of Confinement on Detonation Behavior of Vapor-Deposited Hexanitroazobenzene Films.* Fifteenth International Detonation Symposium, San Francisco, CA.

Kuhl, A. L. (2010). *Thermodynamic States in Explosion Fields*. in Proceedings of Fourteenth International Detonation Symposium, Coeur d'Alene, ID.

Los Alamos National Laboratory, & NSTec. (2008). pTool Photon Doppler Velocimetry Analysis Tool *User Manual*: Los Alamos National Laboratory.

LPKF:Laser&Electronics. (2016). ProtoLaser U3. from http://www.lpkfusa.com/products/pcb_prototyping/machines/protolaser_u3/

Maisey, M. P., & Bowden, M. D. (2008). Characterization of Detonator Performance Using Photonic Doppler Velocimetry. *Proceedings of SPIE, the International Society for Optics and Photonics, 7070*, 70700P.

OMEGA-Laser-Facility. Streak Camera Overview. *Training Material*. http://opto-mech.lle.rochester.edu/Training%20Material/General/streak%20cameras.pdf

Optronis. (2010). SC-10 Streak Camera Main Unit. from http://www.optronis.com/de/support/downloads/optoscope/datenblaetter-sc-10.html

Polk, J. F. (1984). Determination of the Equation of State of Explosive Detonation Products from the Cylinder Expansion Test, Aberdeen Proving Ground, MD, US Army Armament Research and Development Center Ballistic Research Laboratory, Technical Report ARBRL-TR-02571.

Richards, D. W., Kramer, M. P., House, J. W., & De Angelis, R. J. (2003). Annealing Studies of Pure and Alloyed Tantalum Employing Rocking Curves. *Advances in X-Ray Analysis, 46*, 285-290.

Sargis, P. D., Molau, N. E., Sweider, D., Lowry, M. E., & Strand, O. T. (1999). Photonic Doppler Velocimetry, Lawrence Livermore National Laboratory, Technical Report UCRL-ID-133075.

Specialised-Imaging. Detailed Specifications SIMX. from www.specialised-imaging.com

Tappan, A. S., Wixom, R. R., & Knepper, R. (2014). *Critical Detonation Thickness in Vapor-Deposited Hexanitroazobenzene (HNAB) Films with Different Preparation Conditions*. in Fifteenth International Detonation Symposium, San Francisco, CA, pp. 5002.

Tappan, A. S., Wixom, R. R., & Knepper, R. (2015). *Geometry Effects on Detonation in Vapor-Deposited Hexanitroazobenzene (HNAB)*. in Nineteenth Biennial APS

Topical Conference on Shock Compression of Condensed Matter, Tampa, FL, pp. 1003.

Thorlabs. (2016). 50-1550A-APC - Single Mode GRIN Fiber Collimator, 1550 nm, FC/APC Connector. 2016, from http://www.thorlabs.us/thorproduct.cfm?partnumber=50-1550A-APC

Valenzuela, A. R., Rodriguez, G., Clarke, S. A., & Thomas, K. A. (2007). Photonic Doppler Velocimetry of Laser-Ablated Ultrathin Metals. *Review of Scientific Instruments, 78*, 013101.

Weseloh, W. N. (2014). JWL in a Nutshell, Los Alamos National Laboratory, Technical Report LA-UR-14-24318.

Wharton, R. K., Formby, S. A., & Merrifield, R. (2000). Airblast TNT Equivalence for a Range of Commercial Blasting Explosives. *Journal of Hazardous Materials, 79*(1), 31-39.

Appendices

The appendices include specification sheets and any other extraneous information.

Appendix A – Sandwich Assembly

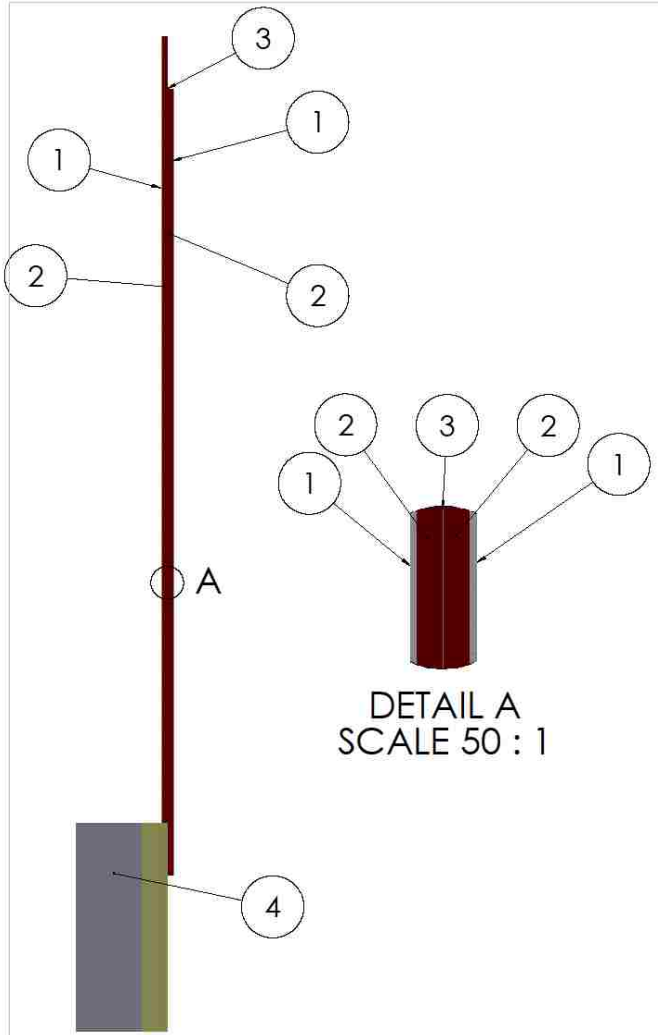

DETAIL A
SCALE 50 : 1

ITEM NO.	PART NUMBER	DESCRIPTION	QTY.
1	Tantalum Substrate	Tantalum, various thicknesses	2
2	HE	HNAB, ~100 μm thick	2
3	Glue Layer	SYLGARD 527, ~3 μm	1
4	Initiation	PETN with polycarbonate line wave generator	1

Thickness Tantalum
50.8 μm
76.2 μm
101.6 μm
127 μm

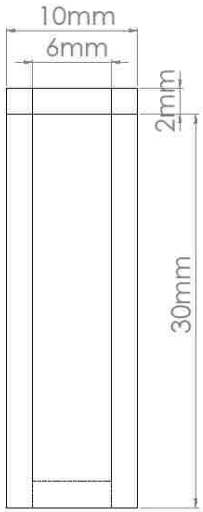

FullSandwich_6mm A2

b

Appendix B – Specification Sheets

B-1: Keyence VHX-5000

Model			VHX-5000
Camera	Camera		1/1.8-inch, CMOS image sensor Virtual pixels: 1600 (H) x 1200 (V)
	Scan method		Progressive
	Frame rate		50 frames/sec. (max.)
	Resolution	Normal	1600 (H) x 1200 (V) Approx. 1000 TV lines
		3CMOS[1,3]	1600 (H) x 1200 (V) Approx. 1200 TV lines(2 million pixels x 3CMOS mode, Excellent color reproducibility)
		High resolution[3]	3200 (H) x 2400 (V) Approx. 1600 TV lines
		Super high resolution[3]	4800 (H) x 3600 (V) Approx. 2000 TV lines or more
		Super high resolution x 3CMOS[2,3]	4800 (H) x 3600 (V) Approx. 2000 TV lines or more(18 million pixels x 3CMOS mode, Excellent color reproducibility)
	High Dynamic Range		16-bit resolution through RGB data from each pixel
	Back-focus adjustment		Not required
LCD monitor[5]	Size		Color LCD (IPS) 23"
	Number of pixels		1920 (H) x 1080 (V) (FHD)
	Display color		Approx. 16,770,000 colors[4]
	Brightness		300 cd/m^2 (Center 1 Point, typical)
	Contrast ratio		1000:1 (typical)
Hard disk drive unit	Storage capacity		500 GB (including 165 GB reserved area) Approx. 1680000 images (When a 2 million-pixel image is compressed) to approx. 55000 images (When a 2 million-pixel image is not compressed)
Image format			JPEG (With compression), TIFF (No compression)
Light source	Lamp		High brightness LED
Interface	LAN		RJ-45 (10BASE-T/100BASE-TX/1000BASE-T)
	USB 2.0 Series A		6 types
	USB 3.0 Series A		2 types

B-2: Specialised Imaging SIMX Framing Camera

Detailed Specifications

SIMX

MODELS

	SIMX4	SIMX8	SIMX16
Number of Channels	4	8	16

OPTICAL

Optics	Single input beam splitting optics Channels can be fitted with individual filters
Lenses	Nikon F-Mount
System Aperture	f2.8
Shutter	Electro-mechanical
Distortion	Nominally zero
Channel Registration	Within one pixel after software correction
Intensity Variation	Better than 5% across the image
Auxiliary Optical Channel Interface	Nikon F-mount bayonet (Optional)

INTENSIFIER/CCD

Image Sensor	ICX285AL
Active CCD Pixel	1360 (H) x 1024 (V)
Pixel Size	6.45 µm (H) x 6.45 µm (V)
Dynamic Range	12 bits
Intensifier	18mm High resolution MCP Input window Fused Silica Output window Fibre Optic Photocathode S25, others on request Phosphor screen P43
Gain	Variable up to 10,000
Dynamic resolution	>50 lp/mm

TIMING PARAMETERS

System Clock	1GHz quartz crystal controlled
Inherent Delay	50ns
Exposure Mode (each image)	Single exposure or multiple exposures (Max. 8) per channel
Exposure Time	3ns - 10ms in 1ns steps independently variable
Interframe Time	0ns - 20ms in 1ns steps independently variable
Delay to 1st exposure	50ns - 10ms in 1ns steps independently variable
Flash Outputs	3ns - 1ms in 1ns steps independently variable
Framing rates	up to 1 Billion fps
Separation Time (Multiple exposures on same channel)	30ns - 20ms in 1ns steps independently variable

INPUT/OUTPUT SIGNALS

Trigger 1	Electrical signal (BNC connector) Threshold variable from ± 25V Positive or Negative polarity, Make/Break 50Ω or 1KΩ termination
Trigger 2	Electrical signal (BNC connector) Threshold variable from ± 25V Positive or Negative polarity, Make/Break 50Ω or 1KΩ termination
Timing Monitor Pulses	Pulse width (min. 5ns) and position user programmable TTL into 50Ω
Flash Trigger Outputs	Pulse width (min. 5ns) and position user programmable TTL into 50Ω
Camera Interface	Data and command transfer via 100Mbps ethernet cable length 10m (standard), other lengths up to 100m available 100FX fibre optic ethernet link (up to 2Km) - optional
Software	Custom software compatible with Microsoft Windows Operating Systems for camera control, image data archiving in various file formats.

ENVIRONMENTAL

Storage temperature	-10°C to +50°C
Operating temperature	-5°C to +40°C
Humidity	10 - 90% RH non condensing
Vibration shock	10 - 40 Hz Max. 10g in any direction
EMC	Meets all EC harmonized standards

B-3: Optronis SC-10 Streak Camera

Streak Camera Main Unit

Description

The streak camera main unit is the central part of a streak camera system. The main unit consist of a streak tube with supply and control electronics as well as an electro-mechanical shutter. The fiber optically coupled image intensifier II125 is a modular part of SC-10 based systems. Using a separate image intensifier within the electro-optical singal chain provides photon counting sensitivity combined with high detection efficiency and low amplification noise.

Photocathodes

The streak tube is available with different photocathodes having different spectral responses and noise characteristics. Typical data are listed below.

Type	Ref.	Spectral Range	Dark Noise
Bialkali	/BI	200 - 700 nm	50 e⁻/cm²/s
S20LN	/S20LN	200 - 750 nm	100 e⁻/cm²/s
S20	/S20	200 - 850 nm	500 e⁻/cm²/s
S25	/S25	200 - 950 nm	2k e⁻/cm²/s

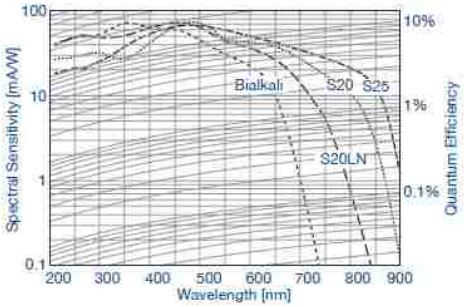

Main Unit

Temporal System Resolution	2 ps (TSU11-10 or SSU11-10 at fastest speed, no /PG option
Photocathode	Active area 8 mm x 2 mm horizontally oriented, available types see above
Gatng Option /PG	Extinction ratio >10^6 / T_r < 1 µs / T_f < 1µs / Frequency <200 Hz / temporal resolution < 5 ps
Gatng Option /PT	Idetntical to /PG option / additional disable mode for temporal resolution = 2 ps
Input Window	Fused silica (others on request)
Streak tube magnification	2 (typicall)
Screen	Area 20 mm (fast axis) x 15 mm (slow axis) / Type P43
Static system resolution	< 100 µm refered to screen
Sweep direction	Vertical (bottom to top for fast axis) / Horizontal (left to right for slow axis)
Interface	Ethernet 10/100 BaseT / RJ45
Dimensions	365 mm x 180 mm x 245 - 250 mm / Weight 16 kg (including SH25-10 and II125)
Environment	5 - 35°C / 20 - 80 % relative humidity not condensing / altitude < 3000 m
Power Supply	AC/DC converter / input 100-240 V, 45-60 Hz / output 24 V, 5 A

Shutter SH25-10

Type	Electro-mechanical
Aperture	Ø 25 mm
Delay	< 20 ms
Frequency	< 10 Hz
Operation modes	open / closed / external control

Intensifier II125

Type	Single stage MCP
Active area	Ø 25 mm
Gain	adjustable 1 - 1000 typ.
Gating time	> 10 ms
Operation modes	continuous / gated

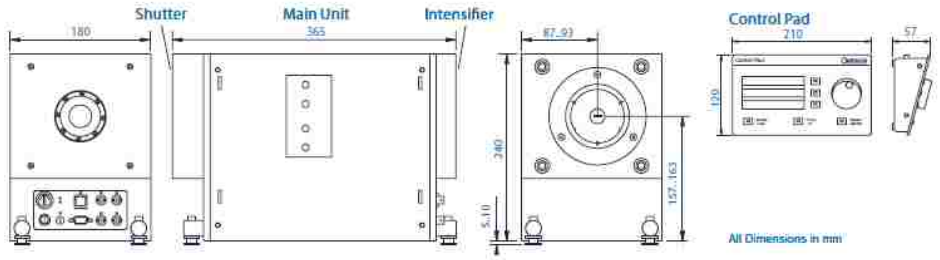

B-4: DektakXT

Specifications	
Measurement Technique	Stylus profilometry (contact measurement)
Measurement Capability	Two-dimensional surface profile measurements; Optional three-dimensional measurement/analyses
Sample Viewing	Digital magnification, 0.275 to 2.2 mm vertical FOV
Stylus Sensor	Low Inertia Sensor (LIS 3)
Stylus Force	1 to 15 mg with LIS 3 sensor
Low Force Option	N-Lite+ Low Force with 0.03 to 15 mg (optional)
Stylus Options	Stylus radius options from 50 nm to 25 µm; High Aspect Ratio (HAR) tips 200 µm x 20 µm; Custom tips available upon request
Sample X/Y Stage	Manual 100 mm (4 in.) X/Y, manual leveling; Motorized 150 mm (6 in.) X/Y, manual leveling
Sample R-Theta Stage	Manual, continuous 360 degrees; Motorized, continuous 360 degrees
Computer System	64-bit multi-core parallel processor, Windows® 7.0; Optional 24 in. flat panel display
Software	Vision64 Operation and Analysis Software; Stress Measurement; Microform; Stitching; 3D Mapping; Optional: Stitching; Pattern Recognition; Advanced Production Interface (API)
Vibration Isolation	Vibration isolation solutions available
Scan Length Range	55 mm (2 in.); 200 mm (8 in.) with scan stitching capability
Data Points Per Scan	120,000 maximum
Max. Sample Thickness	50 mm (1.95 in.)
Max. Wafer Size	200 mm (8 in.)
Step Height Repeatability	4Å, 1 sigma on steps ≤1 µm (30 scans using a 12.5 µm stylus)
Vertical Range	1 mm (0.039 in.)
Vertical Resolution	1Å (@ 6.55 µm range)
Input Power	100 – 240 VAC, 50 – 60Hz
Temperature Range	Operating Range, 20 and 25°C (68 to 77°F)
Humidity Range	≤80%, non-condensing
System Dimensions and Weight	455 mm W x 550 mm D x 370 mm H (17.9 in. W x 22.6 in. D x 14.5 in. H); 34 kg (75 lbs.); Enclosure: 550 mm L x 585 mm W x 445 mm H (21.6 in. L x 23 in. W x 17.5 in. H); 5.0 kg (11 lbs.)

B-5: SI-LUX 640

Detailed Specifications

SI-LUX640

LASER HEAD UNIT

Wavelength	640 ± 6 nm*
Light output power	200 W (-10/+30 %) or 400 W (-10/+20 %)
Min single pulse duration	~10 ns
Max single pulse duration	30 µs (max power drop 20 %)
Rise time approx.	10 ns (10...90 %)
Fall time approx.	5 ns
Delay	sync input to start of light pulse max 70 ns (including control cable delay)
Jitter	< 5 ns
Power drop	approx. 0.2% / µs at short pulses, below 5 µs
Protective electronics	for preventing unacceptable pulse parameters max 0.03 % duty cycle is possible for unlimited operation time max 100 % duty cycle is possible for max 30 µs laser active time
LED Indicator	Solid green: laser is powered and ready for operation
Casing	anodized aluminum
Weight	approximately 0.5 kg
Dimensions	150 mm (L) x 62 mm (W) x 36 mm (H)

LASER CONTROL AND SAFETY UNIT

(to fulfill laser safety requirements)

Key-operated master control for power on/off
Indicator led: green when system is powered
connector for Remote Interlock
connector for system power supply (operating voltage 12 VDC ±10 %, approx. 7W)
connector for 5 V TTL sync in (pulse duration equals the duration of the high state)

CONTROL CABLE

2 m cable between the laser unit and the laser safety feature box

LIGHT GUIDE

2 m long light guide between the laser unit and illumination optics
core Ø 3 mm for 200 W laser and core Ø 5 mm for 400 W laser

ILLUMINATION OPTICS

Ø 25 mm version or Ø 50 mm version (beam expanders)
includes mechanical beam stopper

LASER SAFETY GOGGLES

to protect the operator from laser radiation

Appendix C - Cheetah Results

Run completed by Caitlin O'Grady on 3/30/2016

Input:

```
                                THE COMPOSITION

 Name              % weight     % mol      % volume     Formula
 hnab-ii ast       100.000      100.000    100.000      c12h4n8o12

 Name              Heat of formation  Standard volume  Standard entropy  Molar weigh
t
                   [cal/mol]          [cc/mol]         [cal/(K mol)]     [g]
 hnab-ii ast        6.9073e+004         2.5929e+002       0.0000e+000        452.208

 Heat of formation   = 1.5275e+002 cal/g
 Energy of formation = 1.6846e+002 cal/g
 Standard volume     = 5.7339e-001 cc/g
 Standard entropy    = 0.0000e+000 cal/(K g)
 Standard energy     = 1.5273e+002 cal/g
 Standard density    = 1.7440e+000 g/cc

 Molecular formula
 Elements       mols          % mol          % mass
 c             12.000         33.333         31.872
 h              4.000         11.111          0.892
 n              8.000         22.222         24.779
 o             12.000         33.333         42.457
 The average molecular weight = 452.208  g/mol

 Oxygen balance (by mass): -49.533%             (-7.076% to CO instead of CO2)
```

Output:

```
JWL fit results:
Initial omega =    0.33263, Final omega =    0.49651
E0 [kJ/cc] = -8.257e+000
R[1] =  5.908e+000, R[2] =  2.000e+000, omega =  4.965e-001
A [GPa] =  9.048e+002, B [GPa] =  4.636e+001, C [GPa] =  1.829e+000
Final fitting error =   1.131 %
```

Appendix D – Framing Camera Images

D-1: 50.8 µm (2 mil)

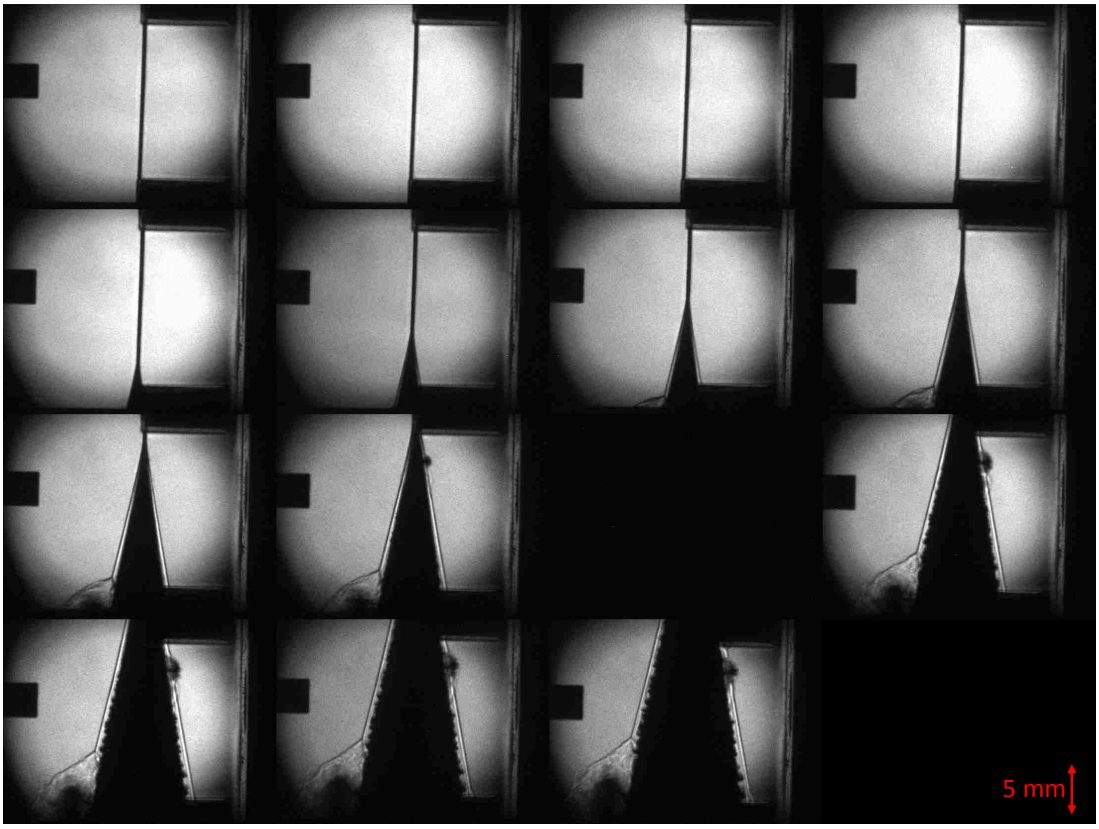

D-2: 76.2 µm (3 mil)

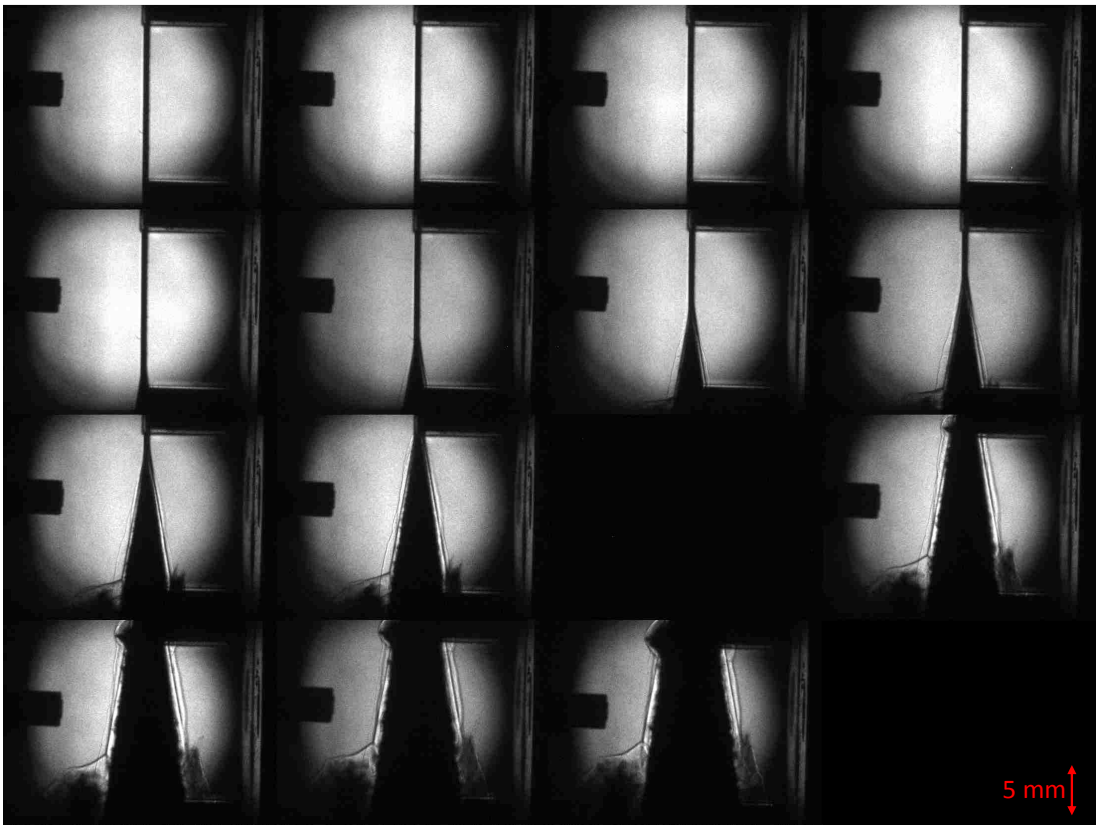

D-3: 101.6µm (4 mil)

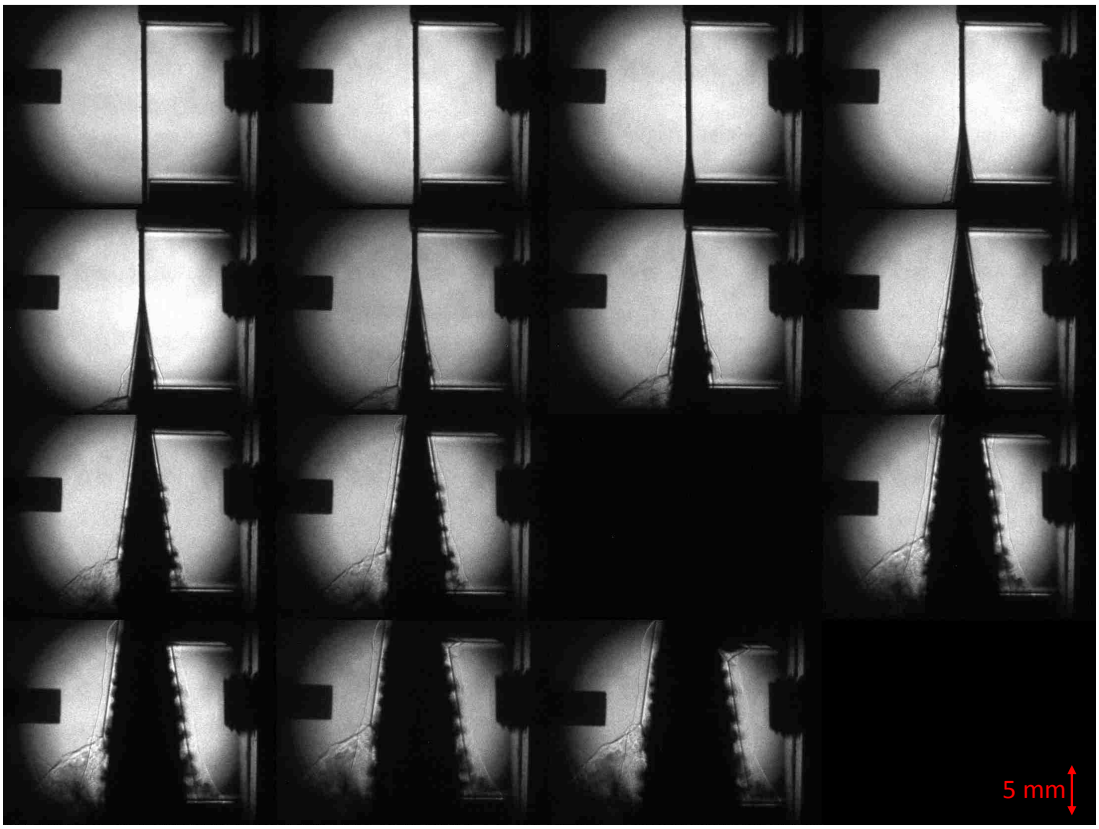

Appendix E: Streak Camera Images

E-1: 50.8 µm (2 mil)

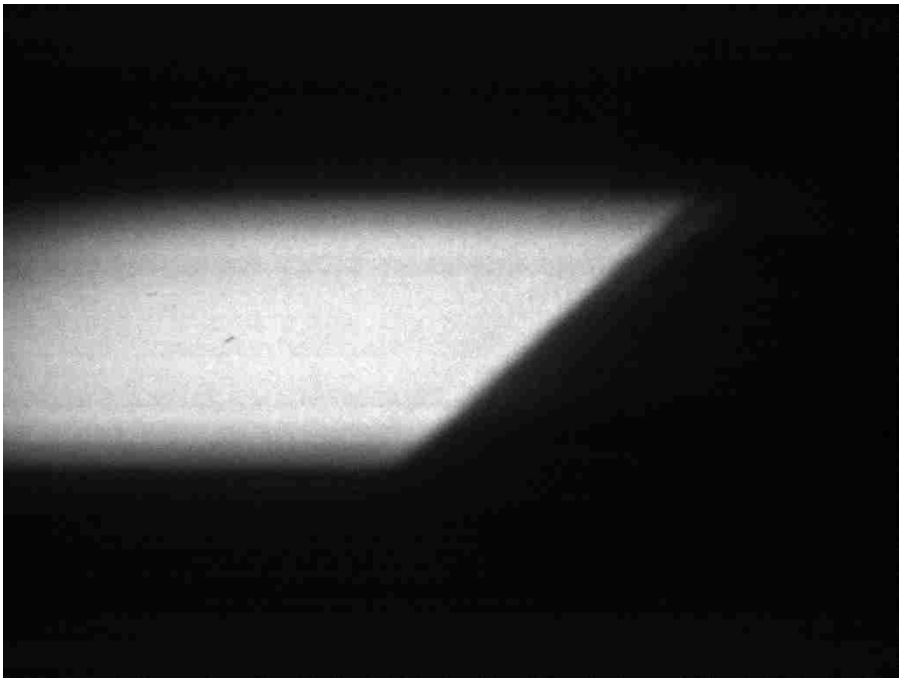

E-2: 76.2 µm (3 mil)

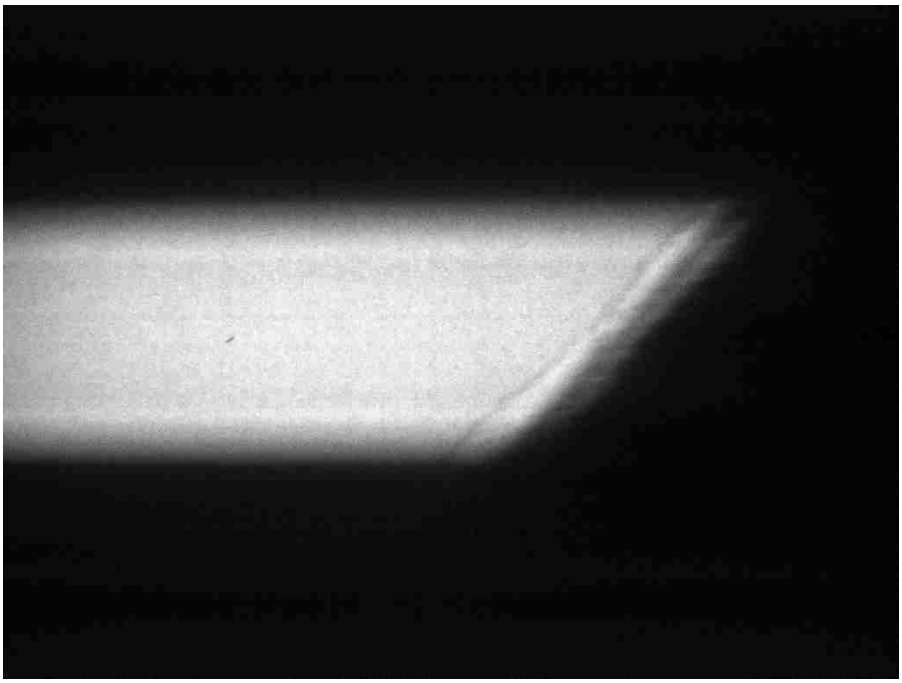

E-3: 101.6µm (4 mil)

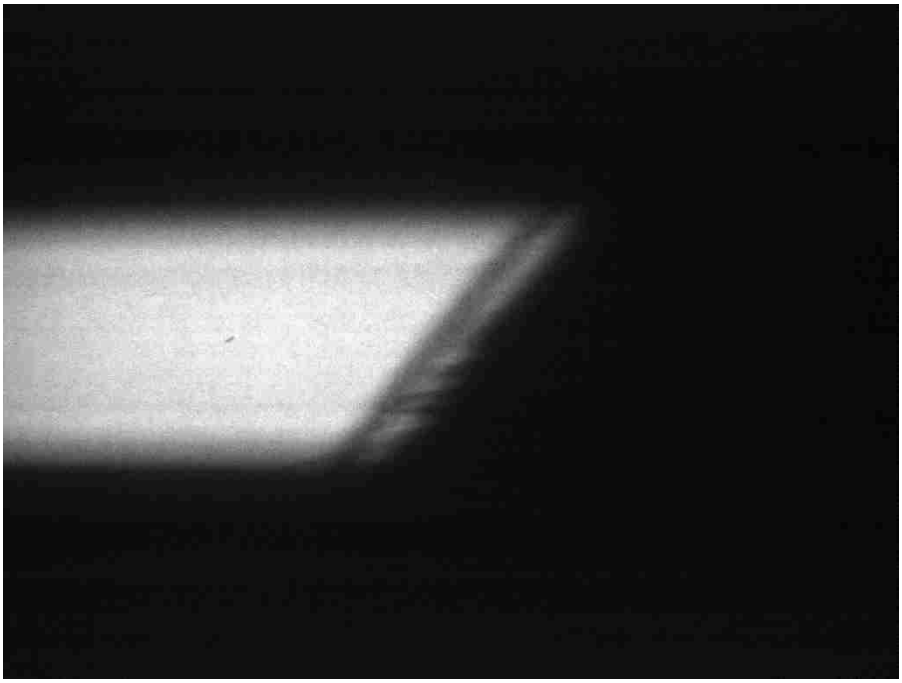

Appendix F: DektakXT Map Scans

Scans were taken using the DektakXT surface profiler system to take thickness surface measurements. Thirteen scans were completed per substrate. A 4 mm length was used to take the average thickness across the substrate per scan.

F-1: 50.8 µm (2 mil)

Side A:

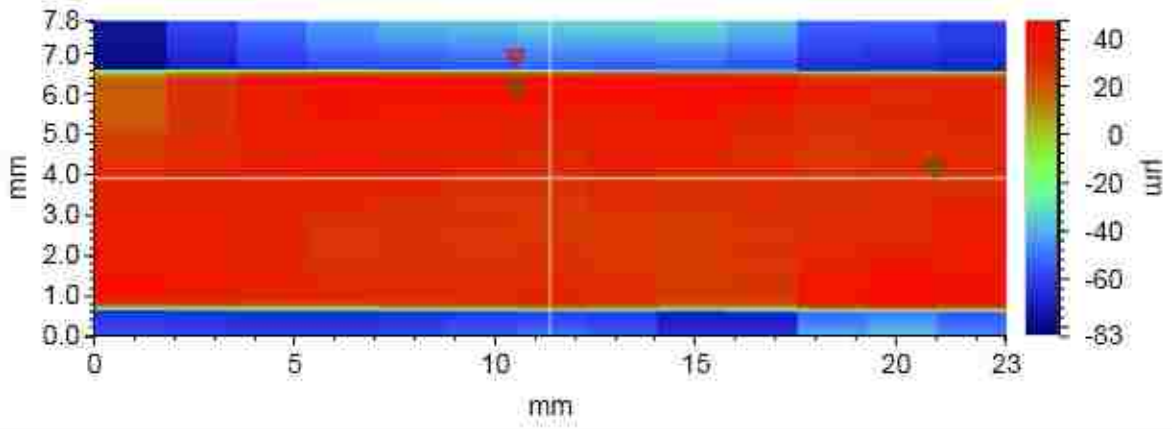

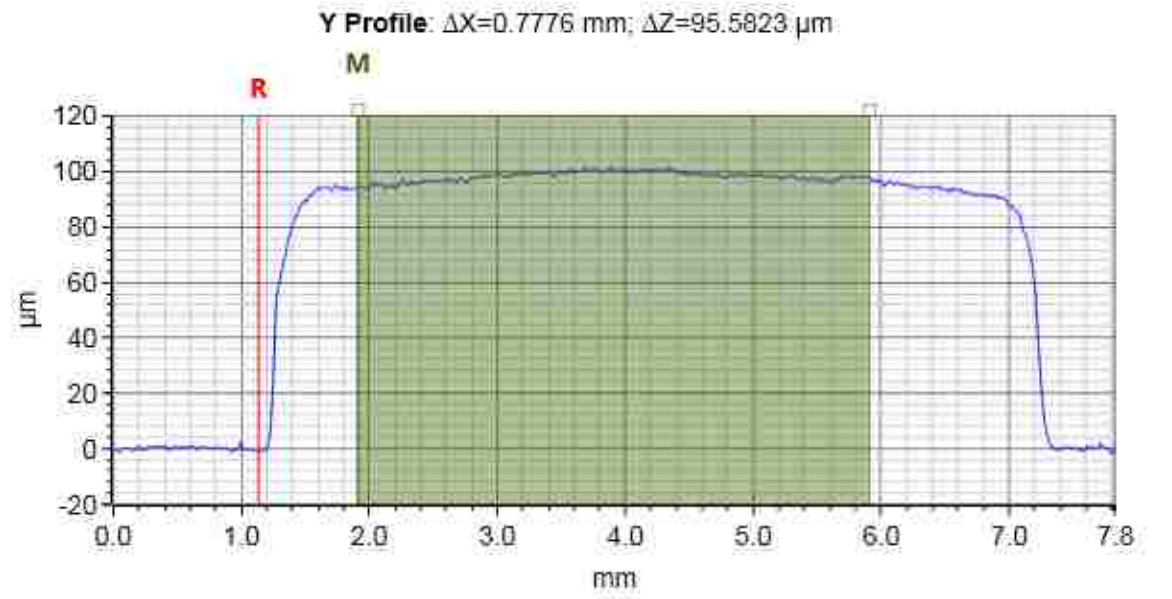

n

Scan (Left to Right)	Thickness Measurement (µm)
1	99.8608
2	98.1907
3	99.0862
4	97.9173
5	94.9152
6	92.6671
7	94.0842
8	93.5936
9	94.0542
10	93.1098
11	94.0758
12	94.5636
13	97.3057

Average Value: 95.648 ± 2.461 µm

o

Side B:

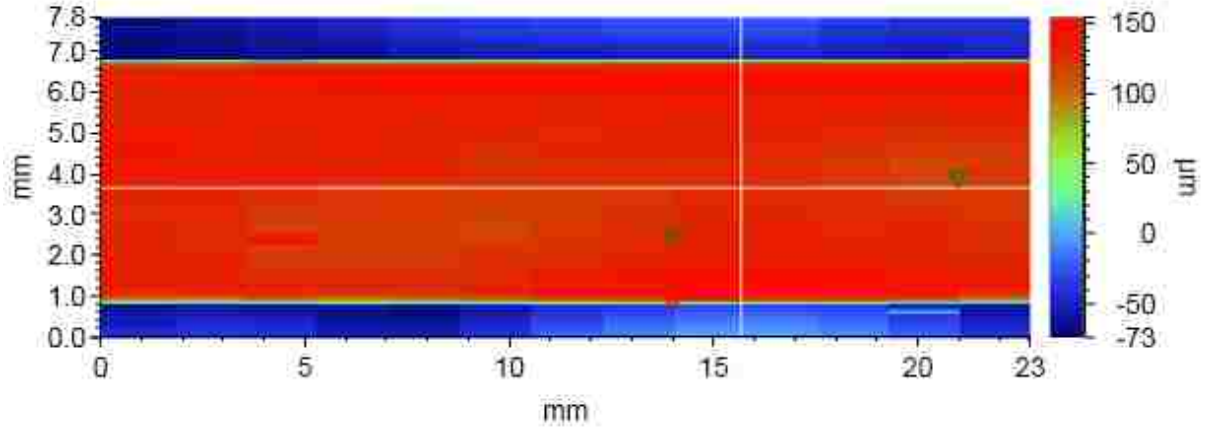
7.8
7.0
6.0
5.0
4.0
3.0
2.0
1.0
0.0
mm
0
5
10
15
20
23
mm
150
100
50
0
-50
-73
µm

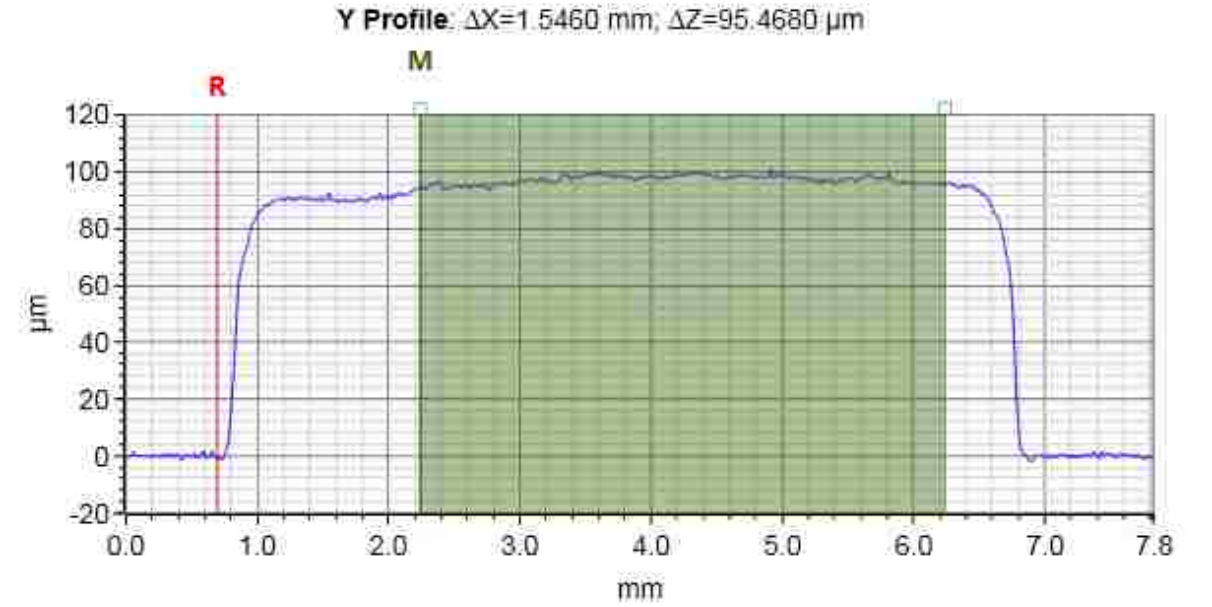
Y Profile: ΔX=1.5460 mm; ΔZ=95.4680 µm
M
R
120
100
80
60
40
20
0
-20
µm
0.0
1.0
2.0
3.0
4.0
5.0
6.0
7.0
7.8
mm

Scan (Left to Right)	Thickness Measurement (µm)
1	97.7254
2	97.4262
3	98.1578
4	95.0886
5	95.0275
6	95.002
7	97.6965
8	94.649
9	95.9775
10	95.0899
11	94.6631
12	93.046
13	94.4103

Average Value: 95.689 ± 1.575 µm

F-2: 76.2 µm (3 mil)

Side A:

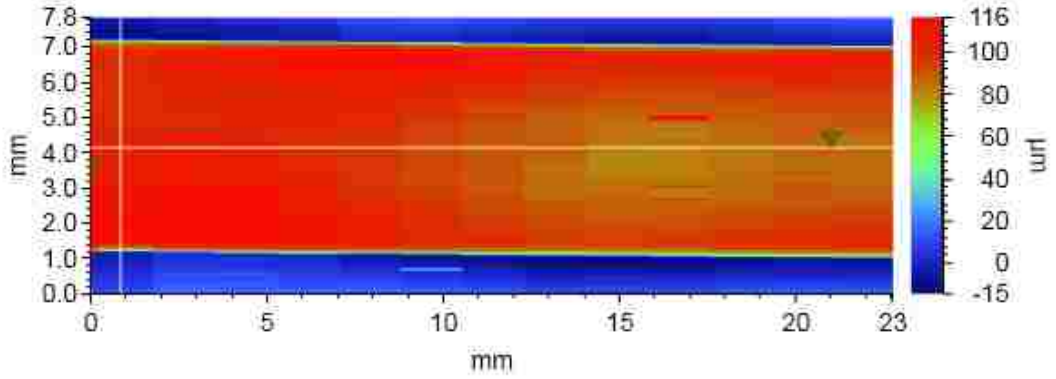

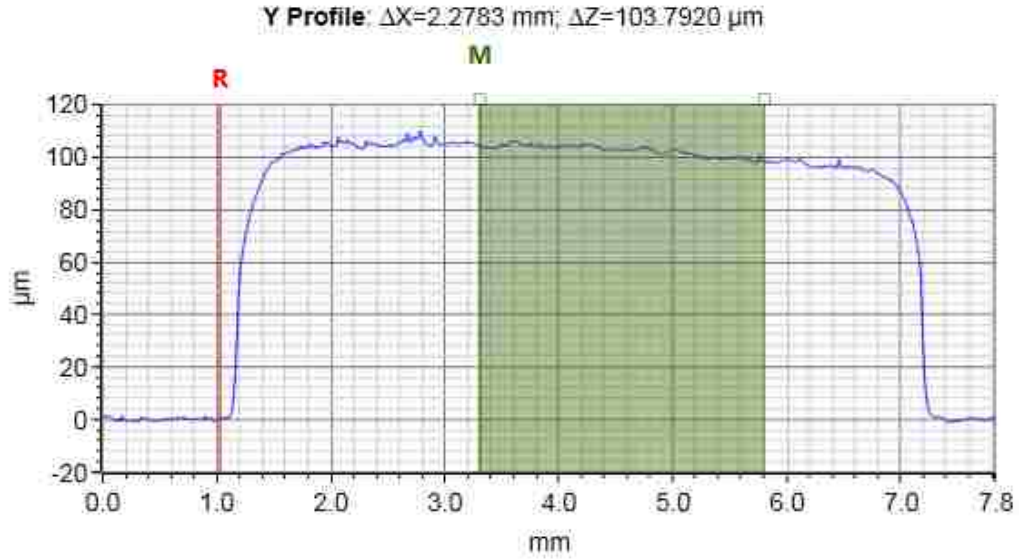

r

Scan (Left to Right)	Thickness Measurement (µm)
1	103.792
2	103.5969
3	102.7989
4	100.066
5	100.6201
6	101.5
7	101.5573
8	101.7428
9	102.1482
10	100.2021
11	100.9146
12	100.1479
13	104.3451

Average Value: 101.803 ± 1.455 µm

Side B:

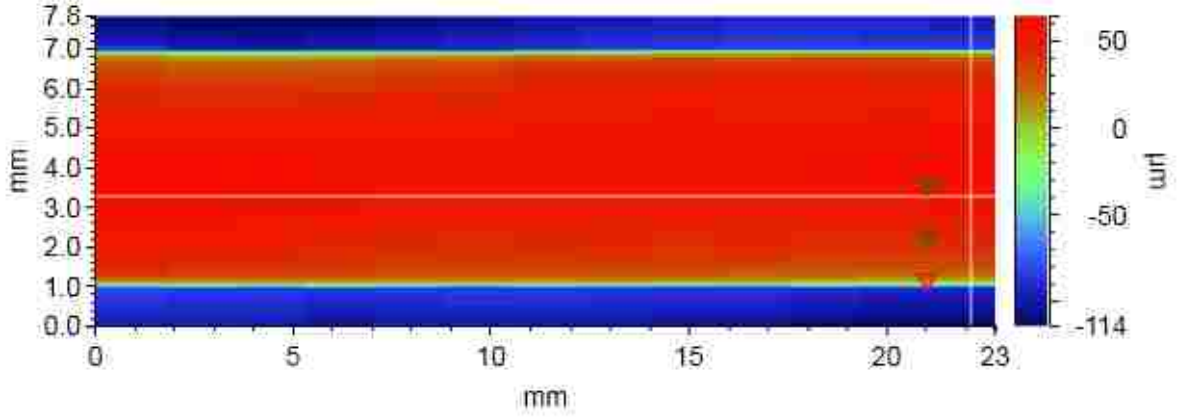
7.6
7.0
6.0
5.0
4.0
3.0
2.0
1.0
0.0
mm
0
5
10
15
20
23
mm
50
0
-50
-114
µm

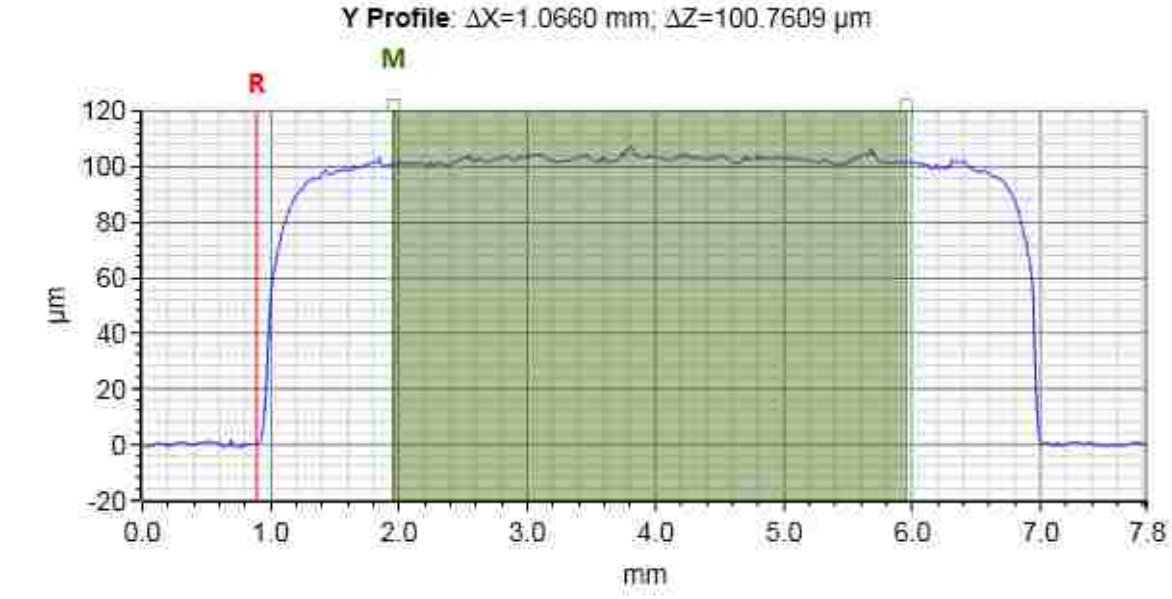
Y Profile: ΔX=1.0660 mm; ΔZ=100.7609 µm
R
M
120
100
80
60
40
20
0
-20
µm
0.0
1.0
2.0
3.0
4.0
5.0
6.0
7.0
7.8
mm

t

Scan (Left to Right)	Thickness Measurement (µm)
1	101.0574
2	101.4699
3	103.39
4	99.5763
5	103.3702
6	95.3735
7	99.526
8	99.9178
9	102.1345
10	98.6061
11	98.3839
12	102.6543
13	101.9513

Average Value: 100.570 ± 2.304 µm

F-3: 101.6 µm (4 mil)

Side A:

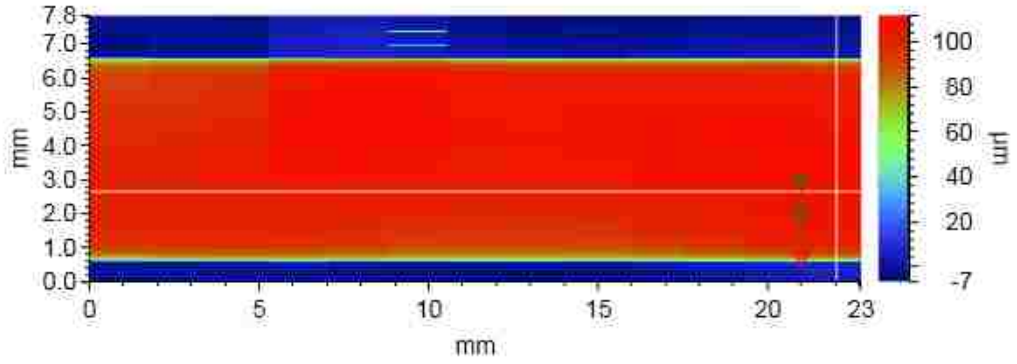

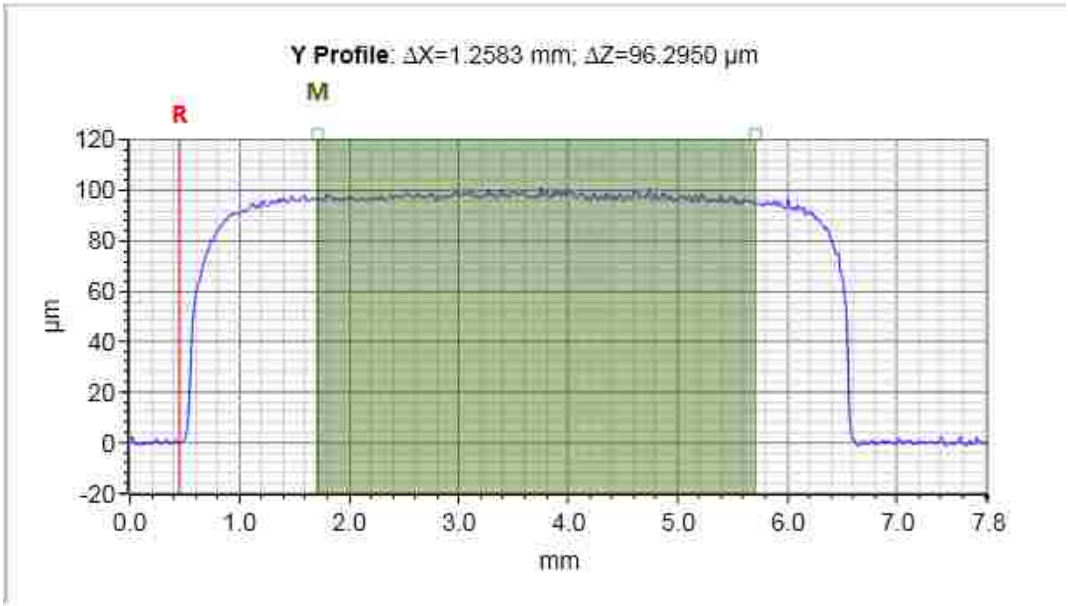

Scan (Left to Right)	Thickness Measurement (µm)
1	97.3202
2	97.002
3	93.0457
4	93.39
5	93.4591
6	93.425
7	93.2772
8	92.0009
9	92.8607
10	92.8754
11	93.1868
12	93.8464
13	96.6908

Average Value: 94.029 ± 1.754 µm

Side B:

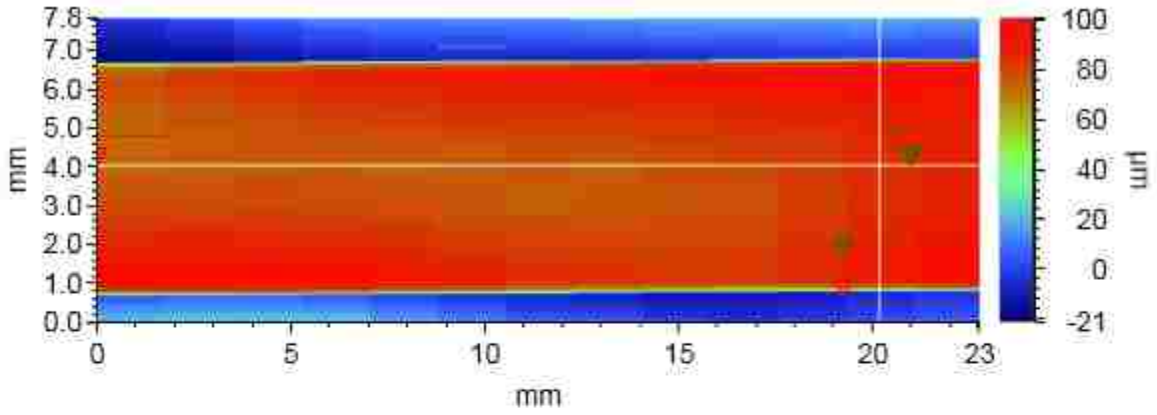
7.8
7.0
6.0
5.0
4.0
3.0
2.0
1.0
0.0
mm
0
5
10
15
20
23
mm
100
80
60
40
20
0
-21
µm

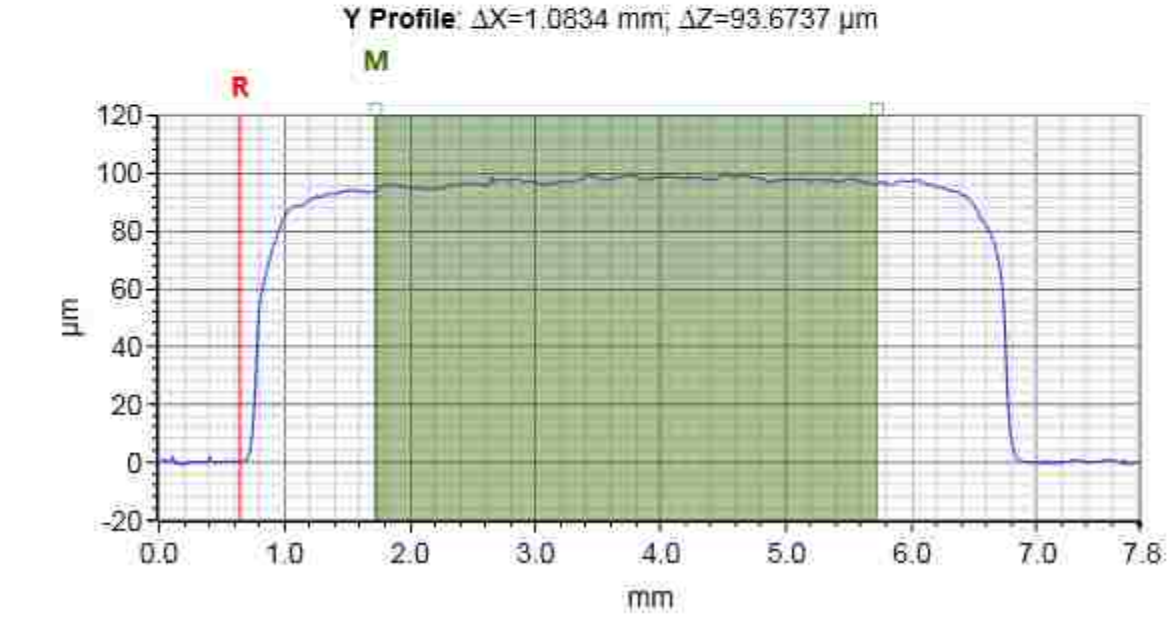
Y Profile: ΔX=1.0834 mm; ΔZ=93.6737 µm
M
R
120
100
80
60
40
20
0
-20
µm
0.0
1.0
2.0
3.0
4.0
5.0
6.0
7.0
7.8
mm

Scan (Left to Right)	Thickness Measurement (µm)
1	95.4966
2	94.7829
3	93.4918
4	95.535
5	94.46
6	93.2968
7	92.9489
8	92.1224
9	93.9602
10	90.5333
11	93.7275
12	93.4694
13	95.1758

Average Value: 93.769 ± 1.410 µm

y

Appendix G: Material Velocity Graphs with Error Bars

G-1: 50.8 µm (2 mil)

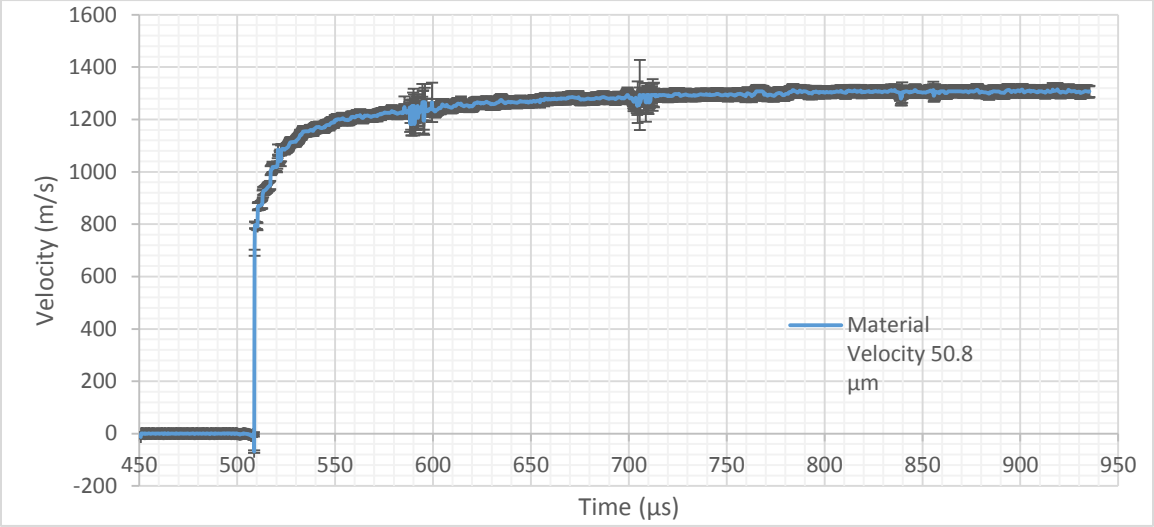

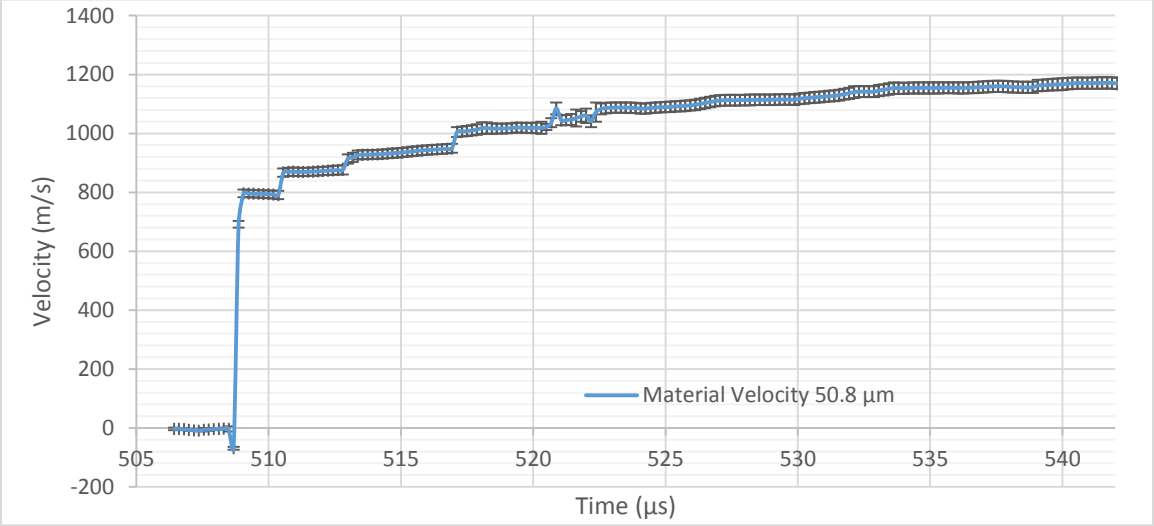

G-2: 76.2 µm (3 mil)

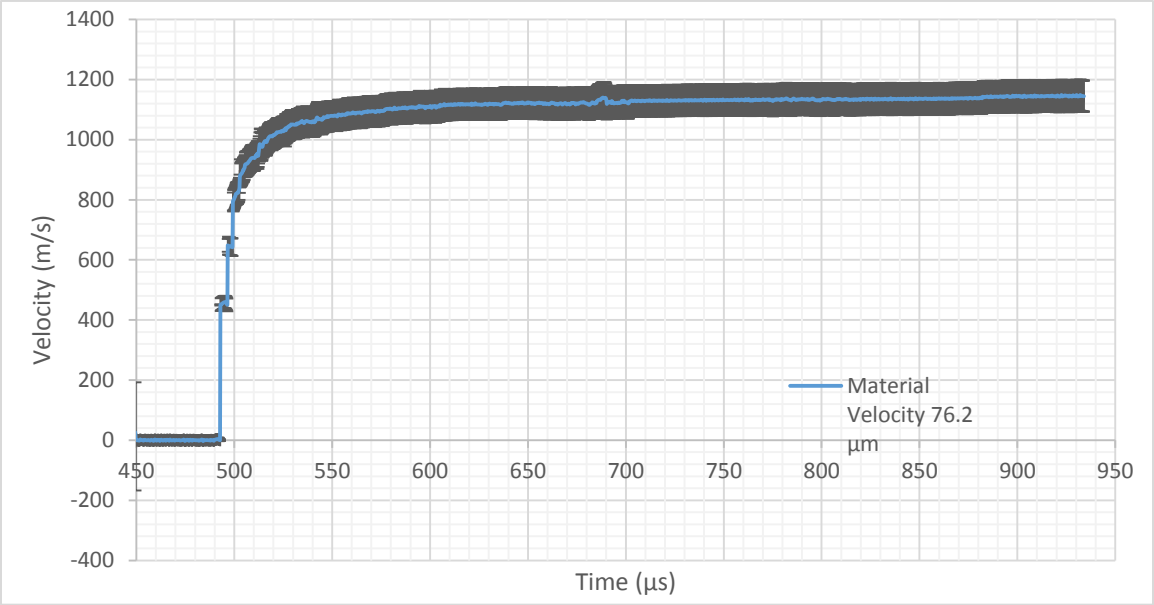

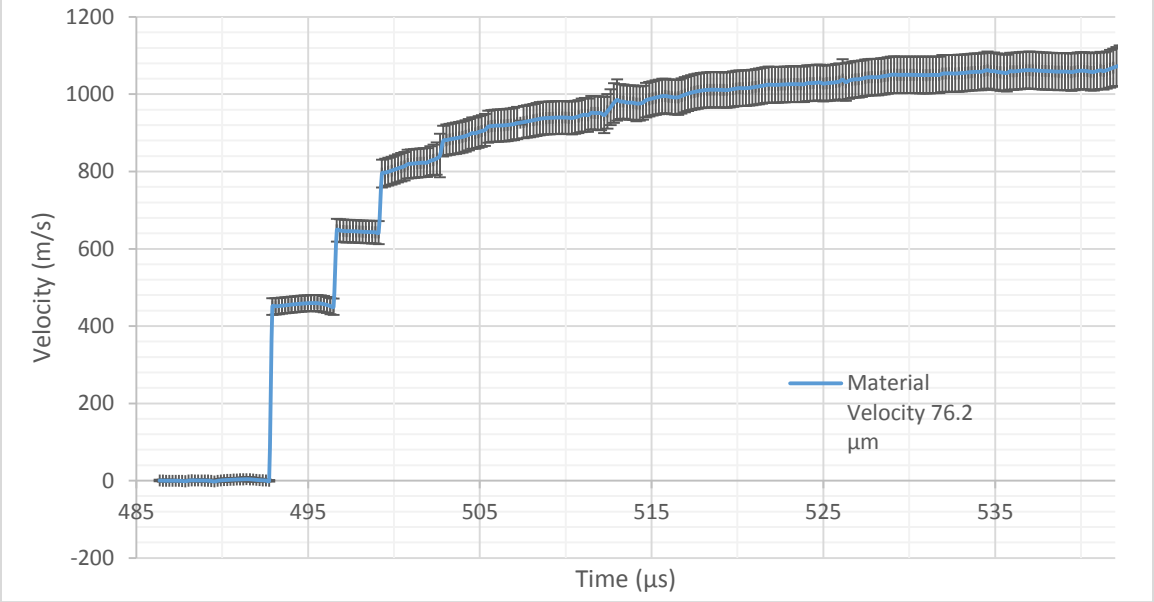

G-3: 101.6 µm (4 mil)